Numerical Investigation of Flow Dynamics Over a Multi-Element Airfoil in Ground Proximity

Bharathwaj Dharani

Thesis submitted to the University of Ottawa
in partial fulfillment of the requirements for the degree of

Master of Applied Science

in Mechanical Engineering

Department of Mechanical Engineering
Faculty of Engineering
University of Ottawa

Abstract

Low Reynolds number ($O(10^4)$) flows play a crucial role in aviation, particularly for unmanned aerial vehicles (UAVs), micro air vehicles (MAVs), and low-altitude flights, where aerodynamic efficiency and stability are critical. When operating near the ground, these flows become more complex due to changes in pressure distribution and wake interactions. Understanding these effects on multi-element airfoils is essential for optimizing performance during takeoff, landing, and low-altitude flight. In this study, we employ Direct Numerical Simulation (DNS) with a high-order spectral element method code, Nek5000, to investigate the flow dynamics around a 30P30N multi-element airfoil in ground proximity, at a low Reynolds number of 1.27×10^4 and an angle of attack (AoA) of 4°. Two-dimensional (2D) simulations are conducted for the varying ground clearance ratios, height from the ground (h) non-dimensionalized by stowed chord length (c), h/c =1, 0.8 and 0.6. The results are compared to previous work, which studied the same airfoil under free-stream conditions, to assess how ground proximity modifies the flow characteristics. The simulation reveals that the shear layer separates near the leading edge of the main element, forming a wave-like roll-up before periodically reattaching after mid-span. As the reattached flow moves further downstream toward the flap, we observe a periodic slot jet flow between the trailing edge of the main element and the flap. The separation bubble in the slat cove region is significantly smaller in ground proximity than in the free-stream case from earlier work, indicating that ground effect modifies the slat wake evolution, potentially altering transition mechanisms and downstream flow structures. Aerodynamic performance metrics, including lift, drag, and pressure and skin-friction coefficients, are analyzed to provide a comprehensive assessment of the airfoil's aerodynamic behaviour. The presence of ground effect results in increased lift and a substantial reduction in drag. Consequently, the lift-to-drag ratio (C_L/C_D) by 28% to 68% relative to previous free-stream studies, corresponding to more than a 1.7-fold enhancement in aerodynamic efficiency.

Acknowledgements

This thesis represents not only the culmination of my academic work, but also a journey shaped by the guidance, encouragement, and generosity of many remarkable individuals.

I would like to begin by expressing my deepest gratitude to my thesis supervisor, Dr. Catherine Mavriplis, whose guidance and unwavering support have been instrumental throughout my master's journey. I am sincerely thankful for the opportunity to work under her supervision at this prestigious institution, where I was encouraged to grow both technically and professionally. Her constant encouragement, positive outlook, and belief in my abilities motivated me through the inevitable challenges of graduate research. I am particularly grateful for the opportunities she provided to attend conferences, which not only enriched my research experience but also strengthened my leadership, communication, and public speaking skills, experiences that have had a lasting impact on my career development.

I am also deeply thankful to Dr. Ming Teng for his mentorship and guidance. From introducing me to Nek5000 and assisting with high-performance computing resources, to sharing his research perspective and experiences, his support played a vital role in shaping my development as a researcher and in broadening my understanding of computational fluid dynamics.

My sincere appreciation extends to my research group colleagues, Amit, Saleh, and Aktham, for their camaraderie, encouragement, and the many shared moments that brought balance and joy to this journey. Their support and friendship made the research environment both motivating and memorable, and helped me return to my work with renewed energy and focus.

I am profoundly grateful to my parents, Dr. Dharani and Dr. Dilshad Begum, and to my entire family for their unwavering support, guidance, and sacrifices. Their belief in me made it possible to pursue my goals, move across continents, and build a meaningful academic and personal life. I am equally thankful to my friends for their unconditional love, encouragement, and motivation throughout my studies.

I would also like to express my heartfelt gratitude to my counsellor, Dr. Adriana Oatu, whose guidance and support provided clarity and strength during my master's program.

Finally, I extend my sincere thanks to the Department of Mechanical Engineering at the University of Ottawa for providing a supportive academic environment and the opportunity to

pursue this degree. I gratefully acknowledge the support of the Natural Sciences and Engineering Research Council of Canada (NSERC) through a Discovery Grant (RGPIN-2023-04564), as well as the computational resources and technical assistance provided by the Digital Research Alliance of Canada, both of which made this research possible. I also thank the Canadian Aeronautics and Space Institute (CASI) for the opportunity to volunteer and assist in coordinating scientific conferences, an experience that significantly enhanced my technical knowledge, professional network, and overall development.

Table of Contents

List of Figures

List of Tables

List of Abbreviations

AoA	Angle of Attack
BC	Boundary Condition
BDF	Backward Differentiation Formula
CFD	Computational Fluid Dynamics
CFL	Courant Friedrichs Lewy
DNS	Direct Numerical Simulation
EXT	Explicit Extrapolation
FDM	Finite Deference Method
FEM	Finite Element Method
FVM	Finite Volume Method
GEV	Ground Effect Vehicle
HPC	High Performance Computing
LES	Large Eddy Simulation
LSB	Laminar Separation Bubble
MDA	McDonnell Douglas Aerospace
NACA	National Advisory Committee for Aeronautics
NASA	National Aeronautics and Space Administration
RANS	Reynolds Average Navier-Stokes
SA	Spalart - Allmaras
SEM	Spectral Element Method
SM	Spectral Method
SST	Shear Stress Transport
WIG	Wing-In-Ground-Effect

List of Symbols

c	Stowed chord length
C_D	Drag coefficient
C_{D_p}	Pressure Drag coefficient
C_f	Skin friction coefficient
C_L	Lift coefficient
C_p	Pressure coefficient
$\mathbf{f}$	Forcing function
F	Forcing function
g_f	Flap gap
g_s	Slat gap
h_{ijk}	Lagrangian interpolant polynomials
$\mathbf{I}$	Identity Tensor
n	Unit vector
N	Order of Polynomial
o_f	Flap Overhang
o_s	Slat Overhang
O	Open or Outflow boundary condition
p	Static pressure
P	Pressure
Re_c	Reynolds number based on stowed chord length
$\mathbf{u}$	Velocity vector
U_f	Forcing velocity
U_∞	Freestream velocity
v	Velocity boundary condition
W	Wall boundary condition

α	Angle of Attack
δ_s	Slat Angle
δ_f	Flap Angle
λ_f	Step Function
μ	Dynamic Viscosity
ρ	Density
ϕ_{ijk}	Basis coefficient

Chapter 1

Introduction

1.1 Motivation

The inspiration for this research arises from the increasing demand in both industry and academia to unravel the complex flow physics over multi-element airfoils operating in ground effect. While extensive research has been conducted on the performance of airfoils at higher Reynolds numbers and free-stream conditions, the complex flow dynamics that arise when an aircraft operates at a low Reynolds number in proximity to the ground, a phenomenon known as ground effect, remain a key area of investigation. This research gap is particularly relevant for the design of modern airliners and short takeoff and landing (STOL) aircraft, where accurate prediction of aerodynamic forces during the landing approach and flare is paramount.

The rapid progress of high-performance computing (HPC) and advanced numerical methods has created new possibilities for exploring complex aerodynamic flows with unprecedented accuracy. Among these approaches, Direct Numerical Simulation (DNS) enables high-fidelity analysis by directly resolving the incompressible Navier-Stokes equations, eliminating the need for turbulence modelling. While DNS remains computationally prohibitive at very high Reynolds numbers and for highly complex geometries, the present study serves as an important step toward pushing the applicability of DNS to more challenging flow regimes.

The availability of Nek5000 [1], a spectral element DNS code, enables the present work to capture the intricate flow features around a canonical three-element 30P30N airfoil in ground effect. While previous investigations, both experimental and computational, carried out by Wang et al. [5-8], Vadsola et al. [2][3], Kokash et al. [9], Teng and Mavriplis [4], have extensively examined this airfoil at low Reynolds numbers, $Re_c = 10^3$ to 10^4 under free-stream conditions, studies focusing on low-Reynolds-number flows in proximity to the ground remain limited. The present study aims to address this gap by providing high-fidelity DNS data and detailed insights into key flow mechanisms, including shear-layer interactions, vortex dynamics, and laminar-turbulent separation behaviour.

Beyond contributing to fundamental understanding, this work also carries practical relevance. Insights gained here are valuable not only for large aircraft during landing but also for the design of micro aerial vehicles (MAVs), unmanned aerial vehicles (UAVs),

ground-effect vehicles, and other platforms operating at low altitudes and low Reynolds numbers. By addressing this gap, the study advances both the theoretical knowledge of ground-effect aerodynamics and its application to future flight technologies.

1.2 Airfoils

The concept of lifting surfaces dates back to the late 1800s and early 1900s, when pioneers such as Otto Lilienthal demonstrated that cambered wing surfaces could significantly improve the lift-to-drag ratio. In 1902, the Wright brothers incorporated simple cambered airfoils into their designs, enabling the first successful powered flights. Systematic airfoil research emerged in the 1910s and 1920s, initially relying on empirical methods and trial-and-error testing. With the establishment of the National Advisory Committee for Aeronautics (NACA) in 1915, wind tunnel investigations were conducted more rigorously, leading to the development of standardized NACA airfoil series that optimized lift, drag, and stall characteristics and became benchmarks for aircraft design. As aviation progressed into the jet age, new challenges such as compressibility effects, swept wings, and transonic flows drove the development of supercritical airfoils. In the modern era, advances in computational fluid dynamics (CFD) have enabled the design and optimization of specialized airfoils that extend far beyond the capabilities of traditional wind tunnel testing.

An airfoil is a streamlined surface specifically shaped to generate more lift than drag when moving through a fluid. While they serve as the fundamental building blocks of wings and propellers in aviation, airfoils also play a crucial role in other industries, including wind energy (wind turbine blades), power generation (turbomachinery blades), marine propulsion (propellers and hydrofoils), and even automotive engineering (spoilers and downforce devices). Airfoils can be classified into distinct types based on parameters such as camber, aerodynamic characteristics, flight regime, as well as by special-purpose application. While airfoils are used in various industries, the classifications discussed here are primarily relevant to aircraft applications. These categories are outlined in the following sections.

1.2.1 Based on Camber

Airfoils can be classified based on their camber into symmetrical and cambered types. Symmetrical airfoils have identical upper and lower surface geometries and generate no lift at zero angle of attack. They are commonly used in aerobatic aircraft, where consistent aerodynamic performance is required for both upright and inverted flight. Cambered airfoils, in contrast, have a curved profile with the upper surface more convex than the lower, producing positive lift even at zero angle of attack and achieving higher lift

coefficients at low angles of attack. These are widely used in general aviation, gliders, and aircraft optimized for subsonic flight.

1.2.2 Based on Flow Characteristics

Airfoils can also be classified according to their flow characteristics as Laminar flow airfoils and High-lift airfoils. Laminar flow airfoils are designed to maintain laminar flow over a large portion of the chord, which reduces skin-friction drag and improves aerodynamic efficiency, but they are sensitive to surface roughness and contamination. High-lift airfoils, often incorporating multiple elements such as slats and flaps, are designed to maximize lift at low speeds, making them suitable for takeoff and landing phases of flight. These airfoils play a critical role in enhancing performance and safety in aircraft that require high lift coefficients or operate at low Reynolds numbers.

1.2.3 Based on Flight Regime

Airfoils designed for specific flight regimes optimize performance for different speed ranges. Subsonic airfoils are shaped to provide high lift and low drag at speeds below Mach 0.8, making them ideal for general aviation and low-speed aircraft. Transonic or supercritical airfoils feature a flattened upper surface and a thicker trailing edge to delay shock formation and reduce drag near Mach 0.8-1.2, enhancing efficiency in high-speed subsonic flight. Supersonic airfoils, with thin profiles and sharp leading edges, are tailored to minimize wave drag at speeds above Mach 1 and are commonly used in fighter jets and high-speed aircraft.

1.2.4 Based on Special Purpose or Stability

Certain airfoils are designed for specific functional or stability requirements. Reflexed airfoils, with an upward-curved trailing edge, provide positive pitching moment stability and are commonly used in tailless or flying-wing aircraft. Ground-effect airfoils are optimized for operation close to the ground, enhancing lift and reducing induced drag, which is particularly beneficial for low-altitude aircraft and ground-effect vehicles. Delta airfoils, characterized by a triangular planform, are widely employed in supersonic and high-speed aircraft due to their favourable aerodynamic characteristics at high angles of attack and Mach numbers. These specialized designs enable tailored performance for unique operational needs and stability requirements.

1.3 High-Lift Airfoils

Among the various airfoil types, high-lift airfoils are specifically designed to maximize lift at low speeds, making them essential during takeoff, landing, and other low-speed flight operations. They can be broadly categorized as single-element or multi-element airfoils. Single-element airfoils achieve moderate lift improvements through optimized camber and thickness. In contrast, multi-element airfoils employ multiple surfaces such as leading-edge slats and trailing-edge flaps to significantly enhance lift by energizing the boundary layer, delaying flow separation, and increasing the effective wing area [2][4][6].

In modern aviation, almost all commercial aircraft rely on multi-element wing systems to generate the required lift at relatively low speeds, thereby ensuring safe operations. At the same time, they allow designers to keep the wing area smaller, which directly benefits cruise efficiency and reduces fuel consumption. Since fuel economy is strongly influenced by wing size, efficient high-lift systems play a central role in balancing low-speed performance with optimal cruise characteristics [10].

Among the widely studied multi-element airfoils, the McDonnell Douglas Aerospace (MDA) 30P30N three-element airfoil is one of the most extensively investigated both experimentally and computationally. The MDA 30P30N consists of a main element, a leading-edge slat, and a trailing-edge flap (shown in Figure 1.1). This configuration is renowned for its ability to achieve high lift coefficients while maintaining controlled flow separation, making it an excellent choice for low-Reynolds-number studies and high-lift applications. Its modular design also facilitates the investigation of complex flow phenomena, including shear-layer interactions, laminar separation bubbles, and wake dynamics, which are critical for understanding aerodynamic performance in both free-stream and ground-effect conditions.

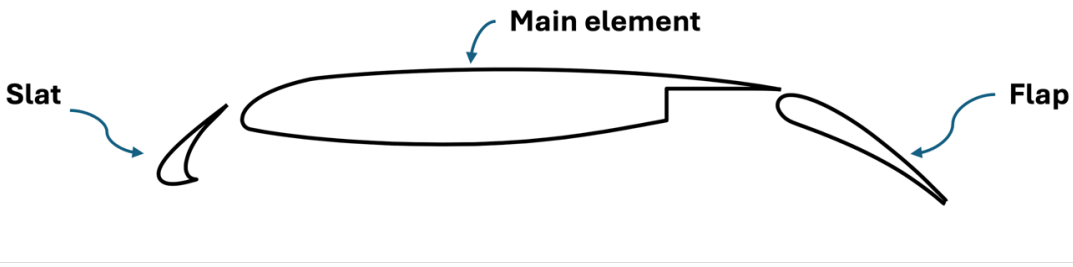

Figure 1:1: MDA 30P30N Three-Element Airfoil

Figure 1.2 illustrates the influence of high-lift devices on the aerodynamic performance of an airfoil. Case A represents the lift coefficient (C_L) of the airfoil without any high-lift devices. In Case B, the leading-edge slat is deployed, which locally delays flow separation by re-energizing the boundary layer and effectively increases the airfoil's angle of attack ($\Delta\alpha$). Case C shows the effect of the trailing-edge flap, which increases the airfoil's camber, resulting in a rise in lift coefficient (ΔC_L). When deployed simultaneously, the flap and slat synergistically enhance the airfoil's lift characteristics, as indicated by the Case A-B-C in Figure 1.2, showing a substantial increase in maximum lift.

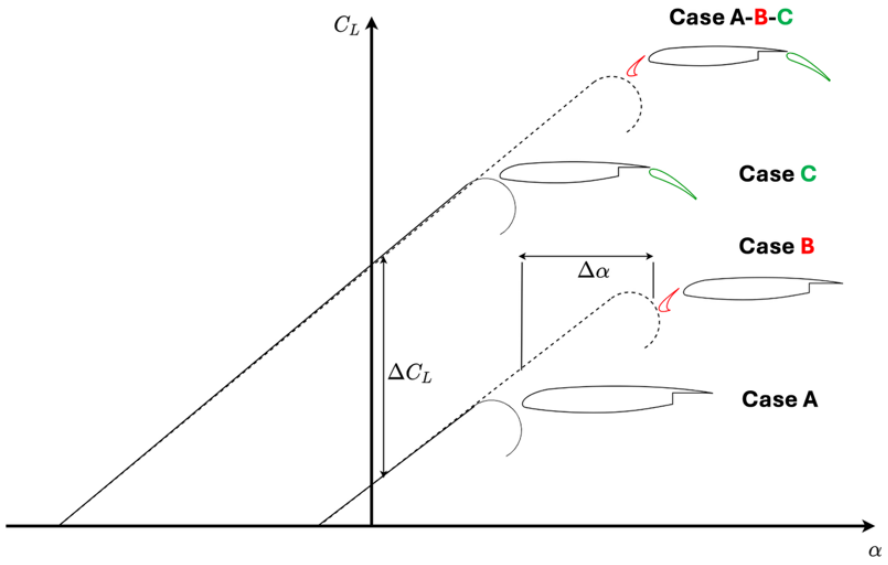

Figure 1:2: The Effect of Leading-Edge Slat and Trailing-Edge Flap on Airfoil Lift Characteristics [2]

While leading-edge slats and trailing-edge flaps significantly enhance lift, the high-lift system itself represents a complex and critical component of aircraft design. Its deployment must be precisely timed for takeoff and landing, yet it must retract cleanly during cruise to minimize drag and maintain aerodynamic efficiency [2][3]. The mechanical complexity of the system also affects manufacturing and maintenance costs, making careful design and optimization essential. With the continued growth of global air traffic and increasing emphasis on fuel efficiency, emissions reduction, and noise mitigation in modern aviation, improving high-lift system performance is vital for developing economically efficient and environmentally sustainable aircraft. Optimizing the lift-to-drag ratio and analyzing overall flow characteristics have become a major focus of research, as these efforts enhance aircraft efficiency, reduce thrust requirements, and consequently lower noise emissions [10].

1.4 Ground Effect Vehicle

Ground effect vehicles (GEVs) operate in close proximity to an impervious surface, such as the ground or water, typically at heights lower than the wingspan. In this regime, aerodynamic interactions with the surface enhance performance. As the aircraft flies near the surface, the altered pressure distribution creates a cushioning effect, increasing pressure on the lower surface and generating additional lift [11], as shown schematically in Figure 1.4. This also reduces wingtip vortices, lowering induced drag and improving overall aerodynamic efficiency (see Figures 1.3 and 1.4).

GEVs are specifically designed to take advantage of this ground effect phenomenon and are often referred to as surface skimmers [12]. Consequently, they benefit from higher lift-to-drag ratios, reduced fuel consumption, increased payload capacity, and shorter takeoff distances compared to conventional aircraft. Additionally, Wing-In-Ground-Effect (WIG) vehicles, a type of GEV, which operate efficiently just above flat surfaces rather than fully flying or floating, represent a hybrid category between traditional aircraft and marine vehicles, combining features of both domains [12].

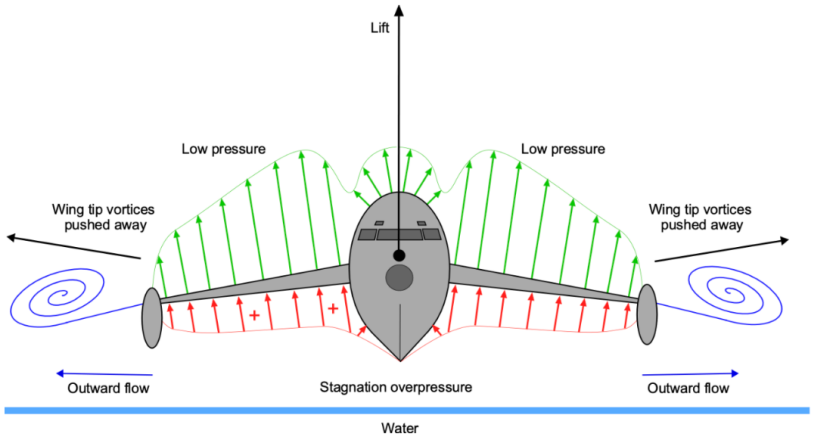

Figure 1:3: Schematic of Pressure Distribution and Reduced Wingtip Vortices Around an Aircraft in Ground Effect [12]

WIG vehicles have evolved from experimental Soviet-era ekranoplans**,** such as the Lun-class and A-90 Orlyonok, designed for high-speed, heavy-payload operations just above water, to modern commercial crafts like the AirFish-8, which efficiently exploit ground effect for increased lift and reduced drag. This demonstrates the enduring potential and versatility of WIG technology.

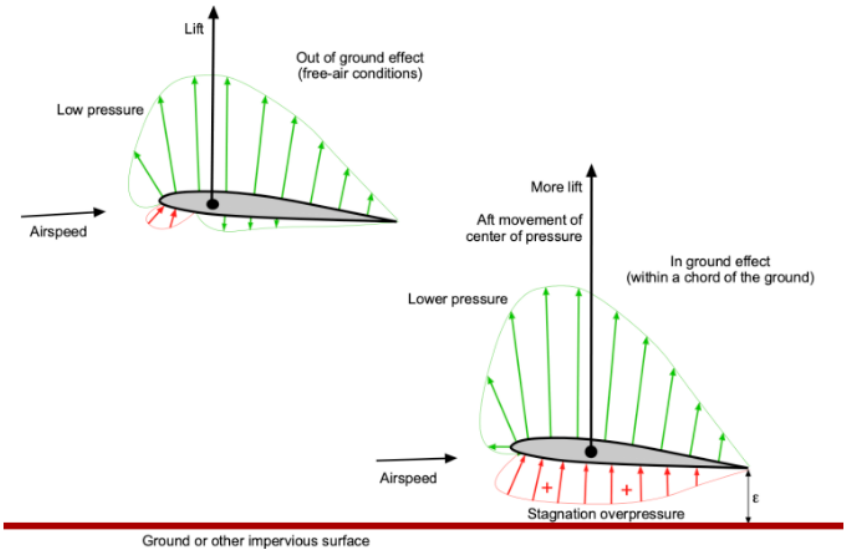

Figure 1:4: Comparative Pressure Distribution Over a 2D Airfoil Section in Free-Stream (Left) and Ground Effect (Right) [12]

Designing ground effect vehicles requires careful consideration of wing geometry, high-lift devices, and stability systems, as the aerodynamics and flow physics near the ground differ significantly from free-stream conditions [11]. However, several challenges must be addressed, including stability, control, and safety during maneuvers, particularly in turns [13]. Additionally, variations in terrain or operating over water introduce further complexities, as wave conditions and surface irregularities can affect handling, lift, and overall aerodynamic performance.

As discussed above, the ground effect phenomena increase lift by modifying the pressure distribution around the airfoil while reducing drag due to weaker wingtip vortices and improved aerodynamic efficiency. This is further illustrated in Figure 1.5, where the left plot shows thrust variation directly related to drag, as higher drag requires higher thrust to maintain motion and the right plot shows lift variation, highlighting the enhanced lift generated when operating in ground effect [14].

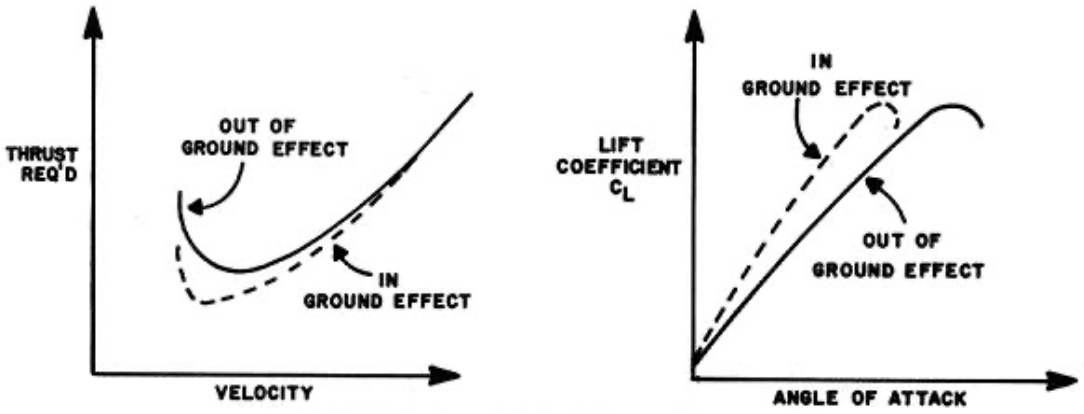

Figure 1:5: Thrust (a) and Lift (b) Variations In and Out of Ground Effect [14]

These discussions indicate that similar aerodynamic performance trends can be expected in the present study, analyzing the 30P30N configuration in ground effect conditions. Furthermore, analyzing proximity effects offers critical insight into the modifications of flow structures and aerodynamic behaviour, providing both additional research scope and practical relevance for the future development of WIG and other ground-effect vehicles.

1.5 Methods for Investigation

Experimental and computational methods are the two primary approaches employed to investigate and understand the complex flow physics around airfoils.

Experimental methods rely on physical testing in controlled environments or real-world conditions to obtain direct measurements of aerodynamic performance. Common techniques include wind tunnel testing, where scaled or full-sized airfoils are exposed to controlled airflow to measure the various aerodynamic parameters [10][15], and water tunnel experiments [5-8], which are particularly effective at low Reynolds numbers and often incorporate dye-based visualization. Flight testing is another essential method, involving full-scale aircraft equipped with sensors to capture aerodynamic forces and flow characteristics under actual operating conditions, which are very expensive among the others. In addition, flow visualization methods such as smoke lines, PIV imaging, etc., are used to show features like flow separation, vortices, and shock waves.

Computational Fluid Dynamics (CFD) has emerged as a powerful tool for airfoil analysis and optimization, offering detailed flow predictions without the constraints of physical testing. CFD employs numerical methods such as Reynolds-Averaged Navier-Stokes (RANS), Large Eddy Simulation **(**LES**)**, and Direct Numerical Simulation (DNS) to solve

the Navier-Stokes equations, each offering different levels of fidelity to capture flow features and support aerodynamic optimization [10].

The RANS approach is the most widely adopted, as it solves the time-averaged Navier-Stokes equations at relatively low computational cost, making it suitable for engineering applications and design studies. For higher accuracy, LES resolves large turbulent structures while modelling the smaller scales, enabling more precise predictions of unsteady flows [16]. At the highest fidelity, Direct Numerical Simulation (DNS) resolves all turbulence scales directly, though at an immense computational expense.

Most aerodynamic studies commonly rely on RANS and LES models due to their computational efficiency and suitability for general flow analysis. However, in the presence of ground effect, the flow over the 30P30N airfoil is significantly altered, which can delay or promote flow separation and generate complex recirculation between elements, as well as wake interactions between the forward and aft elements, particularly in the slat cove and gap regions. These phenomena are difficult to capture accurately with conventional turbulence models [17][18]. To resolve these flow features precisely and enable detailed comparisons with previously published literature, the present study employs direct numerical simulation (DNS). A more detailed discussion of the numerical methods and the rationale for using DNS are provided in the following Chapter.

1.6 Thesis Outline

This research aims to investigate the flow dynamics around a 30P30N multi-element airfoil at different ground clearance ratios using high-order spectral element Direct Numerical Simulation (DNS). To systematically present the study, the thesis is organized into the following chapters:

Chapter 2, Literature Review and Background, reviews previous work on multi-element and single-element airfoils in both free-stream and ground effect conditions. Chapter 3, Methodologies, describes the methodologies employed in this simulation study, including solver setup, grid and mesh generation, simulation domain configuration, and visualization techniques. Chapter 4, Results and Discussion, presents the results obtained from the Nek5000 simulations, covering velocity and vorticity fields, aerodynamic characteristics, and comparisons with previously published studies. Finally, Chapter 5, Conclusion, summarizes the conclusions of the present work and Chapter 6, Future Work, discusses potential avenues for future research and development.

Chapter 2

Literature Review and Background

Understanding the aerodynamic performance of multi-element airfoils has been the focus of extensive research in both experimental and computational studies. This section reviews prior work on multi-element airfoils, highlighting investigations of lift, drag, and flow separation. Emphasis is placed on studies examining turbulence modelling, Reynolds number effects, and the influence of ground proximity on flow physics. Insights from these studies form the basis for the present analysis of the 30P30N multi-element airfoil in ground proximity and guide the selection of simulation approaches and modelling strategies, as introduced in Chapter 1 and further detailed in the following Chapter 3.

2.1 Experiments and Computation

A wind tunnel experiment was conducted by Chin et al. [15] in the NASA Langley Low Turbulence Pressure Tunnel (LTPT) at flight Reynolds numbers of 5 x 10^6 and 9 x 10^6, investigating the 30P30N baseline and a modified 30P30AD configuration, which incorporated a 0.23% increase in flap gap. Their results demonstrated that lift generally increased with Reynolds number, with the overall lift coefficient (C_L) rising up to a stall angle of approximately 21°, beyond which it declined. The slat contribution to lift continued to increase with AoA, while the flap contribution decreased, highlighting the complex redistribution of lift among the elements at higher incidences. The 30P30AD showed reduced lift and higher drag compared to the baseline within the AoA range of 12°-16°. Beyond this range, it demonstrated a higher lift, increasing the maximum C_L by about 0.05 and delaying stall by approximately 1, owing to the enhanced flap suction peak from the increased gap. These results highlight the strong sensitivity of the multi-element airfoil to geometric modifications, and their significant impact on overall aerodynamic performance.

Klausmeyer and Lin [10] also investigated the MDA 30P30N airfoil at Reynolds numbers of Re of 5 x 10^6, 9 x 10^6, and 16 x 10^6over a wide range of angles of attack. Their results showed a stall angle comparable to that reported by Chin et al. [15]. The stall mechanism was attributed to flow reversal on the main element, which initiated separation. Interestingly, they observed that while the flow remained attached to the flap at $C_{Lmax,}$ separation occurred at lower angles of attack.

Computational Fluid Dynamics (CFD) approaches such as RANS, LES, and DNS have been widely employed to extend understanding and support the optimization of flow studies at a lower cost than experiments. These methods resolve the flow structures with varying levels of fidelity, depending on the chosen modelling approach and the specific requirements of the analysis. Comparing computational results with experimental data remains essential for assessing the accuracy of turbulence models and their capability to reproduce detailed flow features. The following literature review pertains to studies conducted under freestream conditions.

CFD analysis investigating several turbulence models to simulate the flow over a 30P30N three-element airfoil configuration was carried out by Rogers et al. [19]. The models examined included the one-equation Baldwin-Barth (BB) model, the one-equation Spalart-Allmaras (SA) model, the Shear Stress Transport (SST) model, and the one-equation Durbin-Mansour (DM) model, for different Reynolds numbers and angles of attack. The surface pressure predictions showed good agreement with experimental data, while the velocity profiles demonstrated only moderate agreement. Notably, the variations among the turbulence models were less pronounced than the discrepancies observed between the computational and experimental results. Overall, the models demonstrated consistent trends, with the SA model showing the strongest wake mixing. However, the SA model did not represent transition effects accurately, leading to premature stall prediction in the simulations due to its limited transition modelling capability. The reattachment point was under-predicted by all the models. Similarly, Lynch et al. [20] noted that the RANS SA model provides a reasonable approximation of the overall flow mechanisms but fails to capture the detailed dynamics of shear-layer merging, transition, and wake development.

The flow over two-dimensional three-element airfoils was examined by Klausmeyer and Lin [21] using various CFD methods. They found that RANS-based approaches showed less variability across different codes. However, while RANS models capture the overall flow features, many struggle to represent curvature effects accurately and tend to predict stronger wakes than observed experimentally. In particular, the slat wake is often overpredicted, leading to discrepancies in the near-field flow. Rogers et al. [19] also reported similar discrepancies between computational results and experiments for the slat wake at lower angles of attack, which were not significantly improved even with increased grid resolution.

Anderson et al. [22] applied a two-dimensional unstructured Navier-Stokes solver to multi-element airfoils with advanced flap configurations, highlighting the importance of systematic grid convergence studies. The Spalart Allmaras (SA) and Baldwin-Barth (BB) turbulence models were employed in this study. Results showed that while surface pressure distributions were reasonably captured with moderate grid sizes, accurate resolution of

velocity profiles-particularly at high angles of attack-required significant mesh refinement and careful treatment of wall boundary layers. Thomas and Lin [23] further highlighted that drag predictions in RANS are significantly influenced by the treatment of far-field boundaries, emphasizing the sensitivity of turbulence modelling results to computational domain settings.

Aeroacoustics is another major area of study for high-lift systems due to its impact on environmental noise and aircraft performance. Several studies have investigated the aerodynamic noise sources and mitigation strategies. Zang et al. [24] used wall-modeled LES with the Ffowcs-Williams-Hawkings approach and identified the slat cove as the primary source of tonal noise, while the main element produced low-frequency noise and the flap contributed negligible noise. Jawahar et al. [25] conducted experiments on the 30P30N with different slat cove fillers, showing that while lift and drag were largely unaffected, the fillers improved lift-to-drag ratio slightly and reduced the suction peak over the main element by up to 15%, as observed from the pressure coefficient results, while also significantly reducing both broadband and tonal noise. These works further highlight that noise generation and control are important considerations alongside aerodynamic performance in high-lift airfoil design.

Deck and Laraufie [18] carried out a numerical investigation of the flow dynamics over a generic unswept three-element airfoil using the Zonal Detached Eddy Simulation (ZDES) technique, for flow conditions corresponding to aircraft approach for landing. They observed the formation of discrete vortices and roll-ups in the slat cove, caused by Kelvin–Helmholtz (KH) instabilities in the separating shear layers. The study also showed that these vortices underwent distortion as they reattached, with most of the smaller vortices being ejected through the slat-main gap, while larger vortices remained entrapped within the slat cove. The slat wake inherited some of the vorticity structures from the cove, which were subsequently stretched due to flow acceleration. Similarly, the separated shear layer in the flap cove, the space where the flap fits when stowed, exhibited roller and rib-like vortices before impinging on the cove walls. The flow in the flap cove shares characteristics with a backward-facing step, with vortices ejected from the main flap gap being deformed and realigned along the streamwise direction. These observations highlight the complex vortex dynamics in multi-element airfoils, which are strongly influenced by local shear-layer instabilities and geometric confinement. Bodart et al. [16] carried out a large-eddy simulation (LES) of the flow around a 30P30N airfoil, which showed good agreement with experimental data for the aerodynamic coefficients. Anderson et al. [22] noted in their study that the multiple elements and intricate geometry of the 30P30N airfoil significantly complicate the flow analysis, as the interactions between the individual components are highly complex. Consequently, turbulence models require further development and careful tuning to accurately capture these flow features [18].

Overall, the literature indicates that conventional turbulence models often fail to accurately predict separation layers and their interactions, and generally cannot capture laminar-to-turbulent transition, as they were not specifically developed for these phenomena [2-3]. Since transition strongly affects the aerodynamic performance of the 30P30N airfoil, high-fidelity approaches such as LES and DNS are required to resolve these details accurately. Although LES can capture the large-scale eddies, it still relies on modelling the small-scale structures, which are critical for understanding transition [26]. The location of transition is particularly sensitive in the presence of ground effect, as in this study, and has a significant impact on drag predictions. Therefore, DNS is employed in the present study, as it can fully resolve the relevant scales and accurately capture laminar-to-turbulent transition [27].

2.2 Low Reynolds Number Flow

At low Reynolds numbers, the aerodynamic behaviour of airfoils exhibits unique characteristics that are critical for design considerations. One important phenomenon in such flows is the development of a laminar separation bubble (LSB). An LSB forms when the laminar boundary layer separates under an adverse pressure gradient and then reattaches downstream after transition to turbulence. While a small and stable bubble may have a limited impact, a large or unstable LSB can significantly deteriorate performance by reducing lift, increasing drag, and promoting earlier stall [28]. Moreover, Mueller and DeLaurier [29] emphasized that particular attention to the airfoil boundary layer is necessary to mitigate the effects of laminar separation bubbles. In particular, the bursting of the LSB, where the separated shear layer fails to reattach and the bubble collapses into fully separated flow, can cause an abrupt loss of lift and severely compromise aerodynamic efficiency [28][30][31]. The present study will also contribute to a better understanding of the presence and evolution of LSBs on multi-element airfoils, complementing observations from previous studies on simpler geometries and single-element airfoils [33-35].

The low-Reynolds number wake shear layer interaction and the complex dynamics in the slat cove were analyzed by Wang et al. [5]. They experimentally investigated the flow over a 30P30N airfoil at $Re_c = 8.32 \times 10^3$ for angles of attack ranging from 2° to 12°, using time-resolved particle image velocimetry (PIV) and flow visualization. Their observations revealed the formation of a slat-cove separation bubble due to the reattachment of the shear layer separating from the lower surface of the slat. A time-averaged large laminar separation bubble was specifically observed over the main element at an angle of attack of 4°. Counter-rotating vortices, known as Görtler vortices, were observed in the slat wake. These vortices were seen as originating from the virtual curved boundary created by the separation bubble in the slat cove and were proposed to induce secondary counter-rotating vortices with the main element shear layer, resulting in streaky structures.

Further, Wang et al. [6] conducted an extended study over a wider range of low-Reynolds-number flows on the 30P30N airfoil at an angle of attack (AoA) of 4° and identified a critical Reynolds number interval between Re_c =1.27 x 10^4 and 1.38 x 10^4, which they considered novel for multielement airfoils at low Reynolds numbers. Within this interval, significant variations in the dominant flow structures were observed. For Re_c below this range, the slat wake was dominated by Görtler vortices, with no evidence of shear-layer roll-up at the slat cusp. In contrast, for Re_c above the critical interval, shear-layer roll-up, similar to that typically seen at higher Reynolds numbers (O(10^6)) was observed at the slat cusp. The subsequent evolution of these vortices resulted in the coexistence of streamwise and spanwise vortices over the main element. Consistent with the earlier study [5], it was reaffirmed that when the slat wake was dominated by Görtler vortices, streaky structures were induced in the main-element shear layer, whereas at higher Reynolds numbers within this interval, spanwise double-secondary vortices were observed above the main element.

The experimental findings of Wang et al. [5-6] were further examined numerically by Vadosola et al. [2-3] using a high-order spectral element method on the 30P30N airfoil for Re_c = 8.32 x 10^3, 1.27x 10^4 and 1.83 x 10^4, AoA of 4°, in both two- and three-dimensional simulations. Good agreement between 2D and 3D results was observed at lower Reynolds numbers, but discrepancies increased as Re_c increased. The computed vortical structures closely matched those reported experimentally: Görtler vortices dominated the slat wake below the critical interval, while above it, streaks and spanwise vortices prevailed, eventually forming three-dimensional hairpin vortices that contributed to turbulence. Before the onset of these Görtler vortices, tongue- or rib-like structures appeared in the slat cove, initiating the three-dimensional transition. Aerodynamic analysis further showed that lift increased with Reynolds number, whereas drag decreased.

Extending the work of Wang et al. [6], Wang et al. [7] investigated the flow over 30P30N for Re_c = 1.38 x 10^4 - 3.05 x 10^4, at the same angle of attack, and demonstrated that slat-wake disturbances govern the transition process by generating double-secondary vortices, which eventually lead to the formation of an attached turbulent boundary layer over the main element. A Proper Orthogonal Decomposition (POD) analysis was used by Kokash et al. [9] to study the slat-cove flow structures and the origin of Görtler vortices for Re_c = 1.27 x 10^4, at AoA of 4°. Their analysis showed that Görtler vortices originate from curvature-induced centrifugal instabilities at the slat cusp. Specifically, bell-shaped flow structures develop near the leading edge of the slat cusp and are advected over the main element through the slat-main gap region, ultimately forming the observed Görtler vortices.

The transition scenarios were studied by Teng and Mavriplis [4] with a focus on analyzing the mean flow behavior and underlying instability mechanisms. In their simulations, the

boundary conditions were modified from Vadsola's case, with flow inlets specified at the left and bottom boundaries and outlets at the top and right boundaries. Their study showed that the overall transition characteristics were qualitatively similar across different Reynolds numbers. In the separated flow regions, the Kelvin-Helmholtz instability was the primary driver of flow instability, while the Görtler vortices were associated with centrifugal instability. The analysis also confirmed that lift increased from $Re_c = 8.32 \times 10^3$ to $Re_c = 1.27 \times 10^4$ but showed a drop at $Re_c = 1.83 \times 10^4$, which was attributed to the disappearance of the laminar separation bubble, leading to a reduction in the effective camber at higher Reynolds numbers. A similar trend was observed in the lift-to-drag ratios. A similar boundary condition and flow configuration with a specific $Re_c = 1.27 \times 10^4$ and AoA of 4°, in ground proximity, will be examined in the present study.

2.3 Ground Effect

As introduced in the previous chapter, ground effect modifies the overall flow field around an airfoil, generally increasing lift and reducing induced drag [35]. To understand these effects in greater detail, several relevant studies were analyzed. Among them, Ahmed et al. [36] conducted experiments on a NACA 4412 airfoil in a low-turbulence wind tunnel using a moving-ground setup at a Reynolds number of 3×10^5. The study examined angles of attack from 0° to 10° with trailing-edge ground clearances ranging from 5% to 100% of the chord. At the lowest clearance, h/c = 0.05 and 0° angle of attack, laminar separation occurred much earlier along the chord. The convergent-divergent passage formed between the airfoil and the ground enhanced suction on the lower surface, further reducing lift. For all angles of attack, drag increased as the airfoil approached the ground due to modifications in the lower-surface pressure distribution. Interestingly, upper-surface suction decreased with reduced clearance for all AoA. Lift decreased at low angles of attack (up to 4°) but increased at higher angles as a result of elevated lower-surface pressure extending to the trailing edge. Pressure coefficients on the lower surface rose with decreasing clearance, and this effect, combined with increasing angle of attack, contributed to improved lift. Drag was reported to be higher for all AoA cases closer to the ground.

Jamei et al. [37] numerically investigated the aerodynamic characteristics of a three-part compound wing and a rectangular wing in ground effect. The compound wing used a NACA 6409 airfoil as its sectional profile. The turbulent flow computations over the wing surfaces were simulated for different ground clearance ratios using the κ-ε turbulence model. The results compared the compound wing with a rectangular wing fixed at 2° angle of attack, using experimental data from other studies for reference, and showed that the compound wing produced higher lift and lower drag than the rectangular wing, resulting in a significantly improved lift-to-drag ratio at small ground clearances. The reduction in

drag was attributed to weaker wingtip vortices due to the closer proximity of the wing to the ground. Additionally, the lower-surface pressure distribution of the compound wing was modified to generate higher lift while reducing downwash velocity. The study further highlighted that the compound wing configuration represents a promising design for Wing-in-Ground (WIG) craft applications. The κ-ω SST and κ-ε turbulence models were shown to provide good overall results in the pressure and wake analysis of an inverted cambered airfoil in ground effect, as reported by Mahon and Zhang [38]. They noted that the κ-ω SST model was more accurate for predicting surface pressures, while the κ-ε model better captured the wake characteristics.

A two-dimensional numerical investigation of clean and four-element airfoil configurations in ground effect at different angles of attack was conducted by Qin et al. [39] at a freestream Reynolds number of Re = 3.52×10^6. The computations were performed by solving the Navier-Stokes equations using the finite element method, with the κ-ω SST turbulence model. The study reported that lift increased for the multi-element airfoil as ground clearance decreased, whereas lift decreased for the clean airfoil under the same conditions. The increase in lift was attributed to higher pressure on the lower surface, which shows good agreement with other literature. Drag and nose-down moment decreased in both cases. Additionally, increasing the angle of attack modified flow separation in the slat cove, with flap separation becoming more pronounced at small ground clearance and low angles of attack. At higher angles of attack, attached flow with two vortices appeared in the wake behind the airfoil, and the vortices intensified as ground clearance decreased.

The dynamic stall analysis using OpenFOAM and Fluent software over a 30P30N airfoil in free-stream and ground-proximity conditions was studied by Sereez et al. [40]. RANS coupled with the Spalart-Allmaras turbulence model was utilized for flow analysis at a Reynolds number of 5×10^6 and a Mach number of 0.2. Contrary to other studies, the lift coefficient was observed to decrease primarily with decreasing ground clearance, an effect attributed to the pressure distribution influenced by the slotted flap. Fully separated flow during dynamic stall further caused a reduction in lift during the downstroke, both in free air and near the ground.

Sereez et al. [41] investigated the impact of ground effect on lateral-directional stability during take-off and landing using a Common Research Model (CRM), representative of a transport airliner. The simulations were performed in Fluent employing the κ-ω SST turbulence model, with a moving wall boundary condition to replicate the runway boundary layer. Their results indicated that, as the aircraft approaches the ground, the roll subsidence and spiral modes merge into an oscillatory roll-spiral mode with a significant frequency. Although this phenomenon pertains to flight dynamics, it is primarily driven by aerodynamic changes, specifically, the altered lift distribution and reduced induced drag

associated with ground effect. The authors also highlighted the need for future investigations on high-lift configurations using hybrid geometries, such as the DLR F11 and NASA GTM models, incorporating fully deployed flaps and slats under ground-effect conditions.

From the above discussion, it is evident that significant performance improvements can be achieved due to ground effect. It should also be noted that most of the discussion in the above literature pertains to higher Reynolds numbers. The behaviour of high-lift devices in the lower Reynolds number regime is less explored, particularly near the ground, where the flow characteristics differ significantly from free-stream flight conditions. This represents a key area of research for understanding and optimizing high-lift systems for low-Reynolds number and ground proximity conditions, and also for the future development of low-Reynolds-number ($<O(10^4)$) UAVs and other small vehicles [29][32].

Therefore, the present DNS study on the 30P30N multi-element airfoil aims to provide detailed insights into ground-effect flow features at low Reynolds numbers, which are critical as they directly influence lift, drag, and stability, and to enhance understanding for future research on aircraft performance in ground-effect flight. In addition, studies by Wang et al. [5-8], Vadsola et al. [2-3], and Teng and Mavriplis [4] provide a solid foundation for this investigation due to the similarities in flow configurations, serving as the starting point for the present work.

Chapter 3

Methodology

This chapter presents the methodology adopted for the 2D numerical simulation of flow over the 30P30N airfoil in ground proximity. It covers all the steps from solver selection and computational domain setup to mesh generation, boundary condition specification, and post-processing of results. The simulations are carried out using the open-source CFD code Nek5000 [1], which is a DNS solver for the incompressible Navier-Stokes equations based on the Spectral Element Method (SEM). The high-order SEM formulation allows accurate resolution of fine-scale flow structures, which are critical for studying the effects of ground proximity.

The chapter is organized as follows: Section 3.1 provides a description of the solver and its capabilities. Section 3.2 details the spatial and temporal discretization schemes employed, including the time-splitting method used for numerical integration. Section 3.3 describes the flow configuration, including the geometry of the 30P30N airfoil and the computational domain. Section 3.4 outlines the three different cases studied, while Section 3.5 discusses the grid and mesh generation strategy. Sections 3.6 present the flow parameters, and Section 3.7 presents the initial conditions and boundary conditions applied in the simulations. Section 3.8 explains the use of the sponge layer at the outlet to prevent reflections, and Section 3.9 provides details on computational time requirements and visualization of results.

3.1 Solver

3.1.1 Numerical Method

The flow over multi-element airfoils in ground effect is governed by the incompressible Navier-Stokes equations, which describe the conservation of mass and momentum in a fluid. Due to the nonlinearity and complexity of these equations, particularly in the presence of boundary layers, flow separation, and the effects of proximity to the ground, analytical solutions are not feasible for realistic airfoil geometries. Therefore, numerical methods are essential to obtain accurate approximations of the flow field.

Several numerical approaches exist for solving the incompressible Navier-Stokes equations, including the finite difference method (FDM), finite volume method (FVM), finite element method (FEM), and high-order spectral methods (SM). While each of these approaches offers distinct strengths, the choice of method depends on the nature of the problem and the level of accuracy required to resolve key physical phenomena.

FVM and FEM are widely used for simulating flows over airfoils and other geometries. FVM is popular in industrial and commercial CFD software due to its robustness and conservative formulation, whereas FEM offers flexibility in handling unstructured meshes and complex boundaries. However, both methods can introduce numerical dissipation and often require very fine meshes to capture thin boundary layers, transition, and separated flow regions accurately.

The Spectral Element Method (SEM) [43] combines the geometric flexibility of the finite element method with the high-order accuracy of spectral methods. In SEM, the computational domain is divided into non-overlapping macro-elements, similar to FEM, and within each element, the solution is approximated using high-order Lagrange polynomials defined at Gauss-Lobatto-Legendre (GLL) points. By increasing the polynomial order (p-refinement), solution accuracy can be significantly enhanced without additional mesh refinement (h-refinement). This high-order representation results in low numerical dissipation and dispersion, allowing SEM to accurately capture fine-scale flow structures. Moreover, SEM exhibits exponential convergence for smooth solutions, ensuring rapid reduction of numerical errors, while its element-based formulation provides excellent parallel efficiency, making it suitable for large-scale, high-fidelity simulations.

These attributes make SEM particularly well-suited for simulating flow over a multi-element airfoil in ground effect, as it can accurately capture laminar-to-turbulent transition, separated flows, wake dynamics, and subtle phenomena such as boundary layer interactions and near-wall vortices that may be overlooked by lower-order methods. The only potential drawback is the computational cost, which increases with polynomial order; however, this is outweighed by the method's ability to deliver highly accurate and physically reliable results, especially for flows where capturing transition and fine-scale structures is critical.

3.1.2 Nek5000

In the present study, Nek5000 [1] is employed as the computational solver. It is an open-source, Spectral Element Method (SEM)-based CFD code developed at Argonne National Laboratory, designed for high-accuracy simulations of incompressible and low-Mach number flows. Its combination of spectral accuracy, geometric flexibility, and element-

based parallel efficiency makes it well-suited for complex geometries such as multi-element airfoils.

In the present study, Nek5000 [1] is employed as the computational solver. It is an open-source, Spectral Element Method (SEM)-based CFD code developed at Argonne National Laboratory, designed for high-accuracy simulations of incompressible and low-Mach number flows. Its combination of spectral accuracy, geometric flexibility, and element-based parallel efficiency makes it well-suited for complex geometries such as multi-element airfoils. These features allow the solver to accurately capture the flow physics around the 30P30N airfoil in ground effect.

Nek5000 solves the incompressible Navier-Stokes equations, given by:

$\nabla \cdot \mathbf{u} = 0,$	(3.1) Continuity

$\rho\left(\frac{\partial \mathbf{u}}{\partial t} + \mathrm{u} \cdot \nabla \mathbf{u}\right) = -\nabla P + \mu(\nabla^2 \mathrm{u}) + \rho \mathrm{f},$	(3.2) Momentum

where vectors are represented by bold letters, $\mathbf{u}$ is the velocity vector, P is the pressure, ρ is the density, μ is the dynamic viscosity, and f is an external force or forcing term.

The Equations (3.2) can also be expressed in nondimensional form as:

$\frac{\partial \mathbf{u}^*}{\partial \boldsymbol{t}^*} + \mathbf{u}^* \cdot \nabla \mathbf{u}^* = -\nabla \boldsymbol{P}^* + \frac{1}{Re}(\nabla^2 \mathbf{u}^*) + \mathbf{f}^*,$	(3.3)

where $\mathbf{u}^* = \frac{\mathbf{u}}{U_\infty}$, $\boldsymbol{t}^* = \frac{tU_\infty}{c}$, $\mathbf{f}^* = \frac{\mathrm{f}c}{U_\infty^2}$, $\boldsymbol{P}^* = \frac{P}{\rho U_\infty^2}$, $Re = \frac{\rho U_\infty c}{\mu}$, and U_∞ is the freestream velocity.

3.2 Discretization

The present study employs high-order spatial and temporal discretization as provided by the SEM in Nek5000. The details of the spatial and temporal discretization, as well as the specific implementation of the time-splitting scheme, are described in the following sections.

3.2.1 Spatial Discretization

In the spectral element method, the physical domain Ω_f (shown in Equation (3.4)) is partitioned into a set of non-overlapping subdomains, or elements, denoted by Ω^n . This decomposition forms the basis for approximating the solution of the governing equations within each element, while ensuring continuity across the entire computational domain.

$$\Omega_f = \bigcup_{n=1}^{N_f} \Omega^n \; ; n = 1, \dots, N_f. \tag{3.4}$$

Within each element Ω^n , any variable $\phi(\mathrm{x})$ is expressed as a tensor product of orthogonal high-order basis functions:

$$\phi(\mathrm{x})|_{\Omega^n} = \phi(x,y,z)|_{\Omega^n} = \sum_{k=0}^{N}\sum_{j=0}^{N}\sum_{i=0}^{N} \phi_{ijk}^{n}\; h_i(r)\, h_j(s)\, h_k(t), \tag{3.5}$$

where $h_i(r), h_j(r), h_k(r)$ are the N^{th} order one-dimensional Lagrangian interpolant Legendre polynomials evaluated at Gauss Lobatto Legrendre (GLL) quadrature points. The coefficient ϕ_{ijk}^{n} are the basis coefficients, representing the values of ϕ at the quadrature points, and $\mathrm{r} = (r,s,t)$ are the coordinates in the canonical reference element $\widehat{\Omega} = [1,1]^3$. For $\mathrm{x} = (x,y,z) \in \Omega^n$, an isoparametric mapping is given by:

$$\mathrm{x}|_{\Omega^n} = \sum_{k=0}^{N}\sum_{j=0}^{N}\sum_{i=0}^{N} \mathrm{x}_{ijk}^{n}\; h_i(r)\, h_j(s)\, h_k(t). \tag{3.6}$$

A similar approach can be used for the discretization of the pressure field, employing Lagrangian interpolants of order N – 2. This is commonly referred to as $\mathbb{P}_N$ - $\mathbb{P}_{N-2}$ staggering. For example, if the polynomial order for the velocity field is the N = 8

corresponding pressure field is represented using N = 6. This formulation is particularly effective in eliminating spurious pressure modes that may arise in the numerical solution of the incompressible Navier-Stokes equations, while also reducing the strictness of pressure boundary condition requirements [44].

These spectral basis expansions for the velocity and the pressure are used in the traditional Galerkin finite element methodology: the strong form of the Poisson equations, for example, are recast in an integral weighted residual form. Through integration by parts, the system becomes a symmetric positive definite matrix equation:

$\boldsymbol{A}\mathrm{u} = \boldsymbol{B}\mathrm{f}$	(3.7)

where $\boldsymbol{A}$ is the stiffness matrix and $\boldsymbol{B}$ is the mass matrix, u is the velocity or the pressure and f is the known right hand side of the Poisson equation. The global matrix equation is solved iteratively by the preconditioned conjugate gradient method. The tensor product formulation allows us to avoid forming the entire matrix. Typically, in the cases investigated, the conjugate gradient pressure solution is the most computationally expensive, while the subsequent velocity solutions are quick, eg., 10 versus 5 overall iterations.

3.2.2 Temporal discretization

Nek5000 employs a semi-implicit time-stepping scheme for the temporal integration of the incompressible Navier–Stokes equations. In this approach, the nonlinear convective terms are treated explicitly using a k-th order extrapolation scheme (EXTk), with, while the viscous terms are treated implicitly using a k-step backward difference scheme (BDFk), also with $k \leq 3$ [45]. For the simulations conducted in this study, a second-order accurate time-stepping scheme, BDF2/EXT2, was employed [46].

The time step Δt is limited by the explicit treatment of the convective terms to ensure numerical stability during the time-marching process. This stability constraint is quantified using the Courant-Friedrichs-Lewy (CFL) condition, which is given by:

$\Delta t < \mathrm{C} \times min_{\Omega_f}\left(\frac{\Delta x}{\lvert u\rvert}, \frac{\Delta y}{\lvert v\rvert}, \frac{\Delta z}{\lvert w\rvert}\right),$	(3.8)

where C denotes the CFL number, and min_{Ω_f} represents the minimum value evaluated over the entire flow field. The quantities Δx, Δy and Δz are the distances between

collocation points in the x, y, z directions, respectively, while u, v, and w are the corresponding velocity components along these directions. In the present study, a CFL number of 0.4 was used in the solver setup to maintain numerical stability throughout the simulation.

3.2.3 Time Splitting Scheme and General Solution Procedure

The semi-discrete formulation of the governing equations, as described by Karniadakis et al. [47], is briefly outlined in this section. The Equation (3.2) is rewritten as follows:

$$\frac{\partial \mathbf{u}}{\partial t} = -\nabla p + \nu \mathbf{L}(\mathbf{u}) + \mathbf{N}(\mathbf{u}) + \mathrm{f} \quad \text{in } \Omega, \tag{3.9}$$

where vectors are denoted by bold letters, p represents the static pressure (P/ρ), ν is the kinematic viscosity.

Here **L** and **N** correspond to the linear and nonlinear operators, respectively, and are defined as follows:

$$\mathbf{N}(\mathbf{u}) = -\mathbf{u} \cdot \nabla \mathbf{u}, \tag{3.10}$$

$$\mathbf{L}(\mathbf{u}) = \nabla^2 \mathbf{u}. \tag{3.11}$$

Furthermore, Equation (3.9) can be split into three sub-steps using a k-th order scheme from the Adams-Bashforth family, as follows:

$$\hat{\mathbf{u}} = \sum_{j=1}^{k} a_j \mathbf{u}^{n+1-j} + \Delta t \left(\sum_{j=1}^{k} b_j \mathbf{N}\left(\mathbf{u}^{n+1-j}\right) + \mathrm{f}^{n+1} \right) \quad \text{in } \Omega, \tag{3.12}$$

$$\hat{\hat{\mathbf{u}}} = \hat{\mathbf{u}} - \Delta t \nabla p^{n+1} \quad \text{in } \Omega, \tag{3.13}$$

$\mathbf{u}^{n+1} = \hat{\hat{\mathbf{u}}} + \Delta t \nu \mathbf{L}(\mathbf{u}^{n+1}) \quad \text{in } \Omega.$	(3.14)

Here, $\hat{\mathbf{u}}$ and $\hat{\hat{\mathbf{u}}}$ denote intermediate velocity fields. The coefficient a_j corresponds to the k coefficients of the k-step backward difference formula (BDFk), while the coefficient b_j are associated with the k coefficients of the explicit extrapolation scheme of order k (EXTk), respectively. Finally, an elliptic equation (Poisson equation) for pressure can be written as,

$\nabla^2 p^{n+1} = \frac{1}{\Delta t} \nabla \cdot \hat{\mathbf{u}}.$	(3.15)

The final velocity $\mathbf{u}^{n+1}$, is obtained by solving the Helmholtz equation, Equation (3.14), in which the intermediate velocity field $\hat{\hat{\mathbf{u}}}$ serves as the forcing term.

3.3 Flow Configuration

3.3.1 Geometry

The three-element 30P30N airfoil configuration used in this study is shown in Figure 3.1, along with the reference coordinates. The nose-tip of the slat leading edge is designated as the global origin (0,0) of the Cartesian coordinate system when the flow approaches at an angle of attack (AoA), α = 0°. The same defined reference coordinates are consistently employed in the results section presented later in this thesis. The stowed chord length, c, defined as the chord length when both the slat and flap are retracted and aligned with the main element, is taken as 1 m in the present study. The slat chord length corresponds to 15% of the stowed chord, while the flap chord length corresponds to 30%. Additional geometric parameters such as the deflection angles with respect to x axis, gap sizes, and overhang distances of the slat and flap are summarized in Table 3.1. The Reynolds number, Re_c, employed in this study is consistently based on the stowed chord length, c. These parameters define the canonical 30P30N configuration, which has been widely adopted in both experimental and numerical studies as a benchmark high-lift system [2-9].

Table 3.1: Geometric Parameters of the 30P30N Multi-Element Airfoil [48]

Slat Angle, δ_s	30°
Flap angle, δ_f	30°
Slat Gap, $g_{s.}$	2.95%
Flap Gap, g_f	1.27%
Slat Overhang, o_s	-2.5%
Flap Overhang, o_f	0.25%

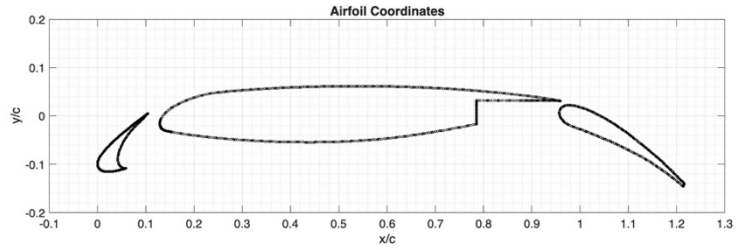

Figure 3:1: The Three-Element 30P30N Airfoil Configuration with Reference Coordinates

3.3.2 Computational Domain

The numerical setup of the computational domain is illustrated in Figure 3.2. Here, x and y denote the streamwise and wall-normal directions, respectively, where u and v are their corresponding instantaneous velocity components. The ground clearance is expressed using the clearance ratio h/c, where h is the vertical distance from the lower tip of the flap to the ground plane.

The computational domain is two-dimensional (2D) and rectangular in shape, with the bottom boundary inclined at 4° relative to the streamwise x-axis to account for the Angle of Attack (AoA), $\alpha = 4°$, when the airfoil operates in ground proximity (discussed in detail in Section 3.7). The total domain length extends 9c in the streamwise direction, while the domain height varies with the ground clearance ratio**,** taking values of 3.5c, 3.3c, and 3.1c for h/c = 1.0, 0.8 and 0.6, respectively. Here, c denotes the stowed chord length, and h

represents the ground clearance height measured vertically from the flap trailing edge to the ground. It is important to note that, in this study, h/c is based on this vertical distance rather than the perpendicular distance to the inclined ground plane (bottom boundary). Therefore, when comparing the present results with conventional literature, a small geometric correction, approximately cos 4° (≈ 0.9976), needs to be applied to account for the 4° inclination of the ground boundary. The inflow boundary is located 3c upstream of the slat nose (taken as the origin), while the outflow boundary is positioned 4.75c downstream of the flap upper trailing-edge tip. These domain extents were selected to ensure that the far-field boundaries exert negligible influence on the flow field around the airfoil, with the exception of the ground boundary, whose influence is intentionally included in order to capture ground-effect phenomena in this study.

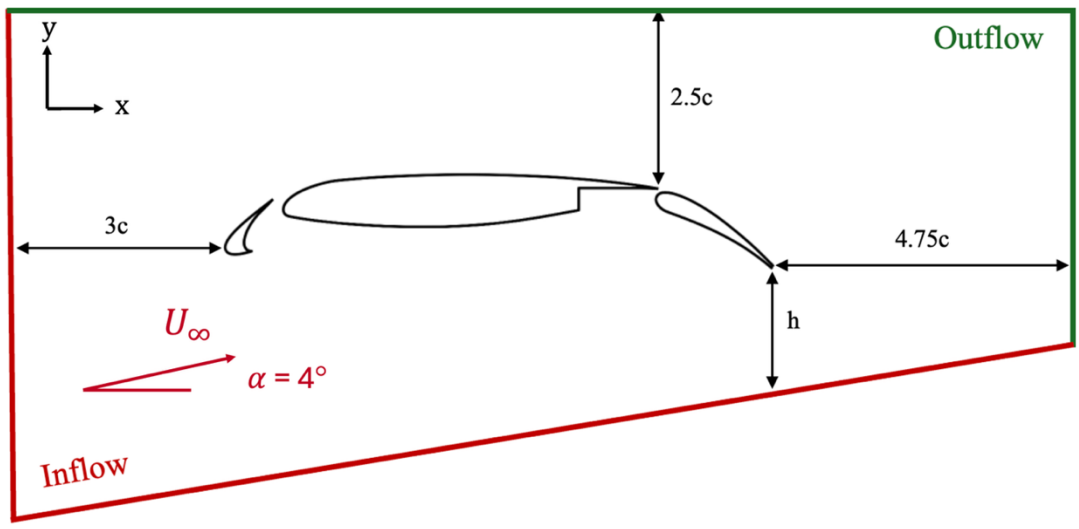

Figure 3:2: Computational Domain with Boundary Conditions and Flow Direction, (c = Stowed Chord Length, and h = Ground Clearance Height Measured from Flap Trailing Edge)

Alternative domain sizes were tested, but the chosen configuration was found to be sufficient for the present computational analysis without compromising solution accuracy. This choice is consistent with earlier numerical investigations [2-4] and maintains compatibility with the rectangular test section geometry employed in related experimental studies [5-8]. The boundary conditions applied to the computational domain are also indicated in Figure 3.2 and are discussed in detail in Section 3.7.

3.4 Cases Simulated

The present study investigates the flow dynamics over the 30P30N airfoil in ground proximity in 2D. Simulations were performed for three different ground-clearance ratios h/c = 1.0, 0.8, and 0.6 at a fixed chord-based Reynolds number Re_c = 12,700 and an angle of attack AoA, α = 4°. These flow configurations and corresponding parameters are summarized in Table 3.2.

Table 3.2: Cases Simulated with Flow Parameters

Case	Ground-Clearance Ratio, h/c	Re_c	AoA
Case 1	1.0	1.27×10^4	4°
Case 2	0.8	1.27×10^4	4°
Case 3	0.6	1.27×10^4	4°

For each configuration, the flow around the airfoil is analyzed, with particular emphasis on major regions of interest where complex flow behaviour is expected. Accordingly, the computational mesh (presented in Section 3.5) is designed to provide fine resolution in the near vicinity of the airfoil to accurately capture critical flow features. Specific locations such as the slat cove, slat-main element gap, main–flap gap, and highly curved regions of the geometry are given special attention during mesh generation, as these areas play a central role in the flow physics. Furthermore, several distinct aerodynamic phenomena such as separation, reattachment, and vortex formation are investigated in these regions. All such regions of interest are labelled in Figure 3.3 for clarity, and critical flow features will be discussed in detail in the results section.

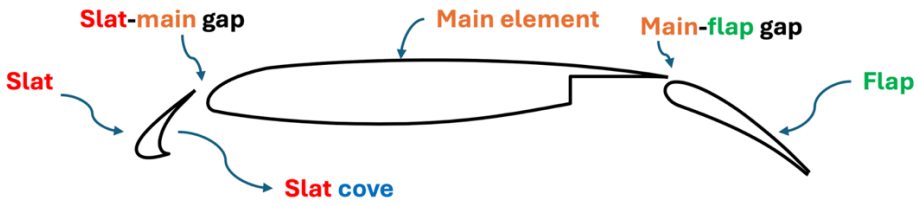

Figure 3:3: The 30P30N Airfoil Labelled with Critical locations

3.5 Multiblock Grid and Mesh Generation

3.5.1 Gmsh

The geometry of the 30P30N airfoil, as described in Section 3.3.1 (shown in Figure 3.1), was imported into Gmsh [49] an open-source software widely recognized for its robustness and flexibility in grid and mesh generation. Gmsh provides advanced meshing capabilities, including structured and unstructured grid generation, refinement control, and boundary layer resolution, making it particularly suitable for high-fidelity simulations of complex geometries. In this study, Gmsh was used to generate the computational grid for the flow domain corresponding to three different ground-clearance cases, with h/c ratios of 1.0, 0.8, and 0.6. The overall multiblock grid, along with the mesh for the flow domain, is shown in Figures 3.4 and 3.5.

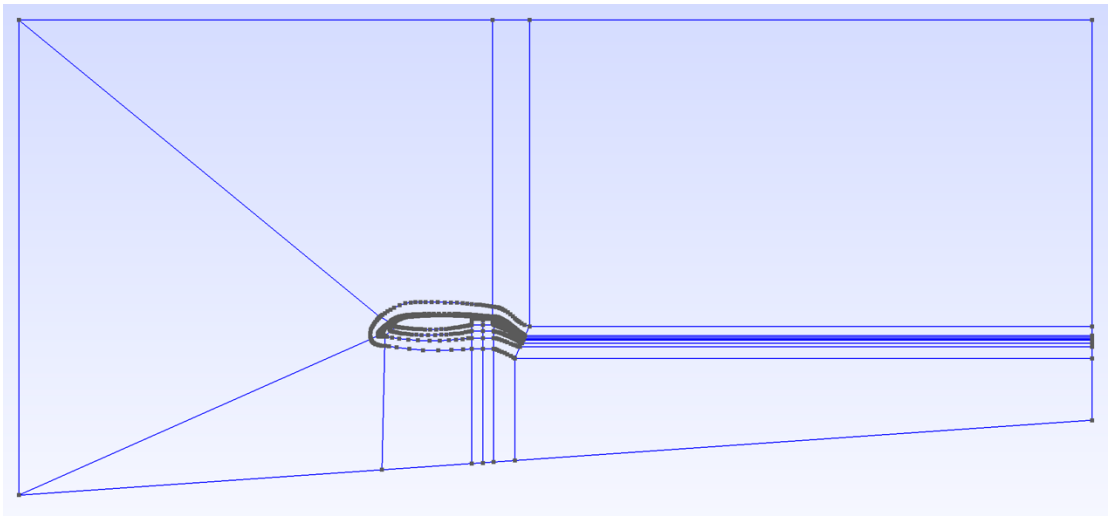

Figure 3:4: Computational Domain with Multiblock Grid Generated using Gmsh

A multiblock structured grid approach was employed for the 30P30N airfoil to ensure accurate resolution of the flow field while reducing the overall number of elements without compromising precision [50] [51]. The computational domain was divided into 45 blocks to facilitate structured grid generation for the entire flow region. In the vicinity of the airfoil surface, a series of three progressively refined inflation layers was implemented to accurately capture the boundary layer and near-wall flow features. These layers gradually decreased in thickness towards the airfoil surface, providing enhanced mesh resolution in regions of high velocity and pressure gradients while maintaining computational efficiency in the far field. The present multiblock structured grid for the 30P30N airfoil represents an

improvement over the previous grid used [2-4]* (See page 32). The specific changes and upgrade in grid resolution will be discussed later in this section.

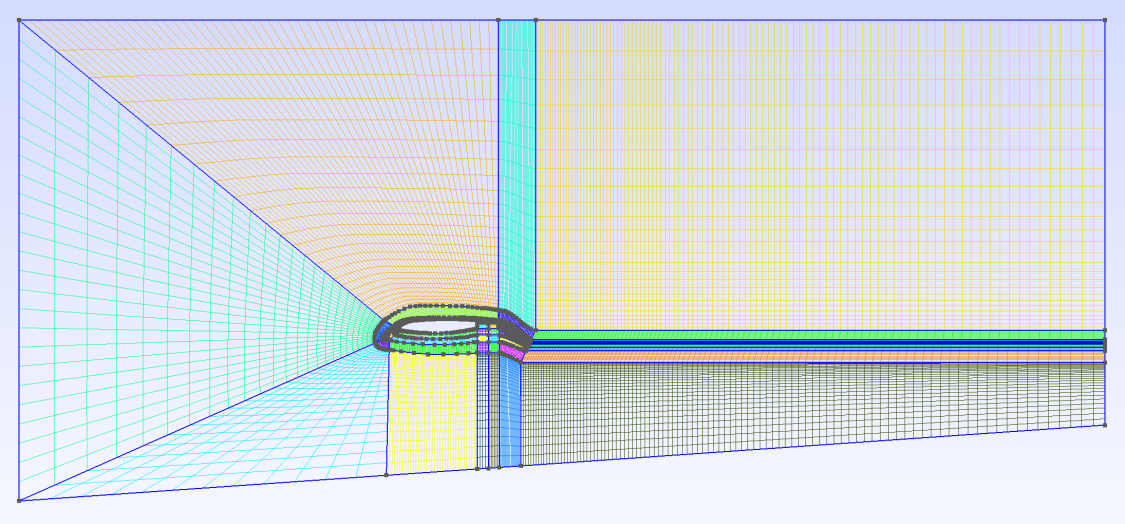

Figure 3:5: Computational Domain with Multiblock Grid with Mesh Generated using Gmsh

The mesh in regions over the slat, slat cove, the slat-main gap, and the flap-main gap was further refined with a higher density of elements, as these areas contain strongly curved geometries and regions with steep geometric gradients, requiring finer resolution to accurately capture the rapid changes in curvature* (See page 32). Mesh quality parameters, such as element orthogonality and skewness, were carefully considered. Sub-blocks were split orthogonally to preserve element quality throughout the domain, with minor skewness allowed in intricate regions to accommodate complex geometries. Since the Nek5000 solver supports only structured grids with quadrilateral elements in 2D simulations, all blocks consisted exclusively of structured quadrilateral elements. The overall grid for the flow domain comprised 16,887 quadrilateral elements, shown in Figure 3.5.

This grid configuration with the same number of elements in each inflation layer was consistently used for all three ground-clearance cases (h/c = 1.0, 0.8, and 0.6). As the ground clearance decreased from h/c = 1 to 0.6, the lower sub-block layer near the ground effectively became more refined. This finer resolution accurately captures the more complex large vortex structures that develop when h/c decreases and also improves the resolving of the downstream wake, which developed further downstream, as discussed in Results Chapter (see Chapter 4). Although grids with a higher number of elements in each sublayer were also considered iteratively during a grid convergence study, the chosen mesh

was found to be sufficient to capture all relevant flow phenomena without compromising computational cost. The resulting multiblock grid mesh near-airfoil, including the inflation layers, is illustrated in Figure 3.6.

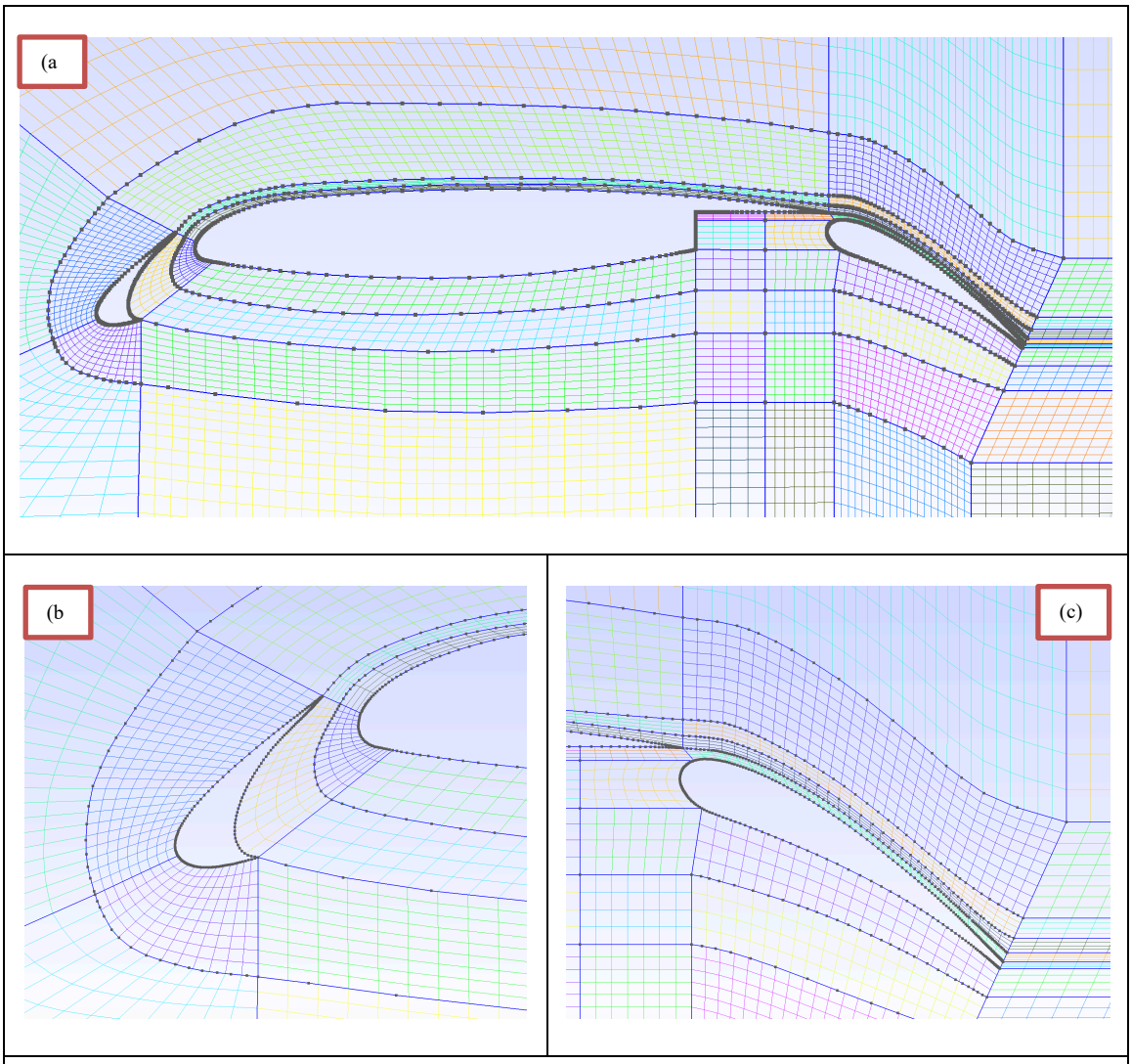

Figure 3:6: Close Up View of Multiblock Grid with Mesh in the Inflation Layer closer to Airfoil Generated using Gmsh, (a) The 30P30N Airfoil, (b) The Salt, and (c) The Flap

In Gmsh, the respective domain boundaries were explicitly defined, consistent with the computational domain shown in Figure 3.2. The inflow, left and bottom boundaries were designated as the inlet, while the outflow, top and right boundaries were defined as the outlet. The airfoil components were separately identified as the slat, main element, and flap. When the mesh is later exported to Nek5000, these identifiers are explicitly called to assign the corresponding boundary and initial conditions, as detailed in the subsequent sections

3.5.2 Nek5000

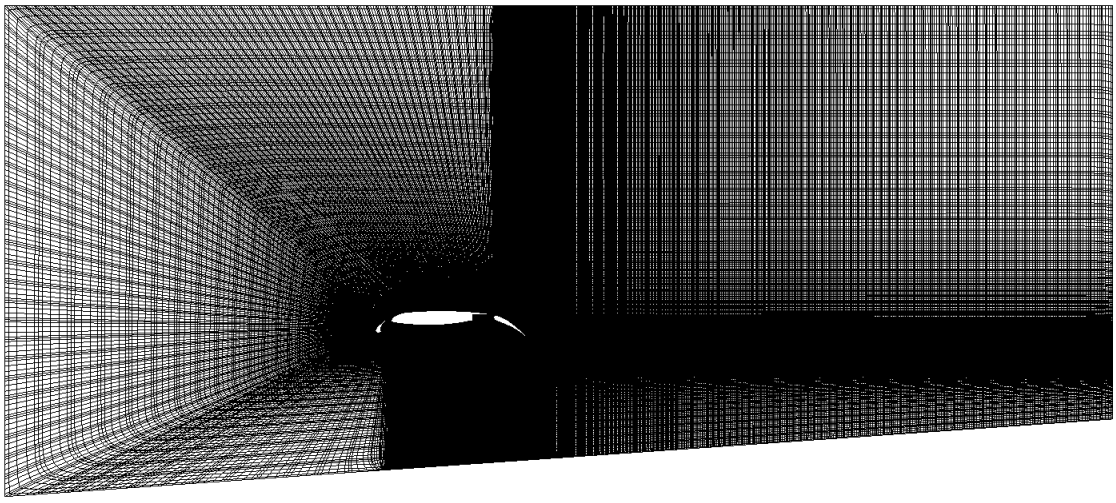

Figure 3:7: Spectral-Element Grid with Mesh of the Computational Domain for Polynomial Order $N = 5$ in Each Direction, Generated by Nek5000

Once the grids for the different h/c cases of the 30P30N airfoil were generated in Gmsh, the mesh files (e.g., *30P30N_groundclearance#.msh*) were exported to Nek5000, where they were converted into the corresponding *30P30N_groundclearance#.re2* files using the *gmsh2nek* [52] converter. Each of the 16,887 quadrilateral elements was assigned a polynomial order of N = 5 for velocity in each direction, as determined from the grid-independence study discussed in Section 4.1. This corresponds to a total of 422,175 spectral collocation points used to resolve the flow field. Additionally, a mesh smoother [53] specifically developed for Nek5000 was employed at runtime to smooth block-element boundary interfaces, thereby improving element quality for stable and accurate flow simulations. The refined two-dimensional spectral-element grid mesh with polynomial order N = 5 is illustrated in Figure 3.7 - 3.9.

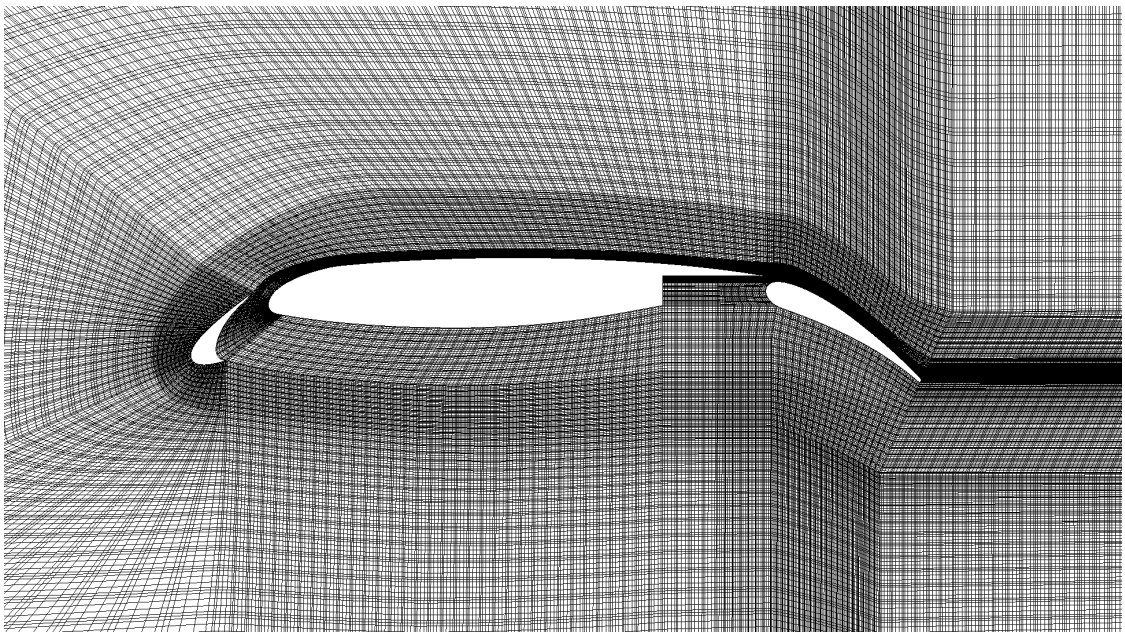

Figure 3:8: The Spectral-Element Grid with Mesh with Polynomial Order $N = 5$ in Each Direction, in the Airfoil Inflation Layers, Generated by Nek5000

*As discussed above, the present grid was improved in several regions with a higher density of elements compared to the previous studies [2-3] and subsequent works [9][4]. Figure 3.10 depicts the mesh and element distribution in the near-airfoil inflation layers from the previous study. Due to the complex recirculation expected in the slat cove in ground effect, the element density in this region was increased. Additionally, to accurately capture the slat geometry, the number of elements over the slat was also increased, as seen by comparing Figure 3.10(b) from the previous study with Figure 3.9(b) of the present grid.

To resolve the flap geometry and capture the jet flow behaviour in the main-flap gap (discussed later in the Results chapter), element density in this region was also increased. This improvement is clearly visible when comparing Figures 3.10(c) and 3.9(c). The number of elements in other regions remained largely unchanged between the two studies. A comparison of the near-airfoil mesh overall between the previous study (Figure 3.10) and the present study (Figure 3.8) further illustrates these enhancements.

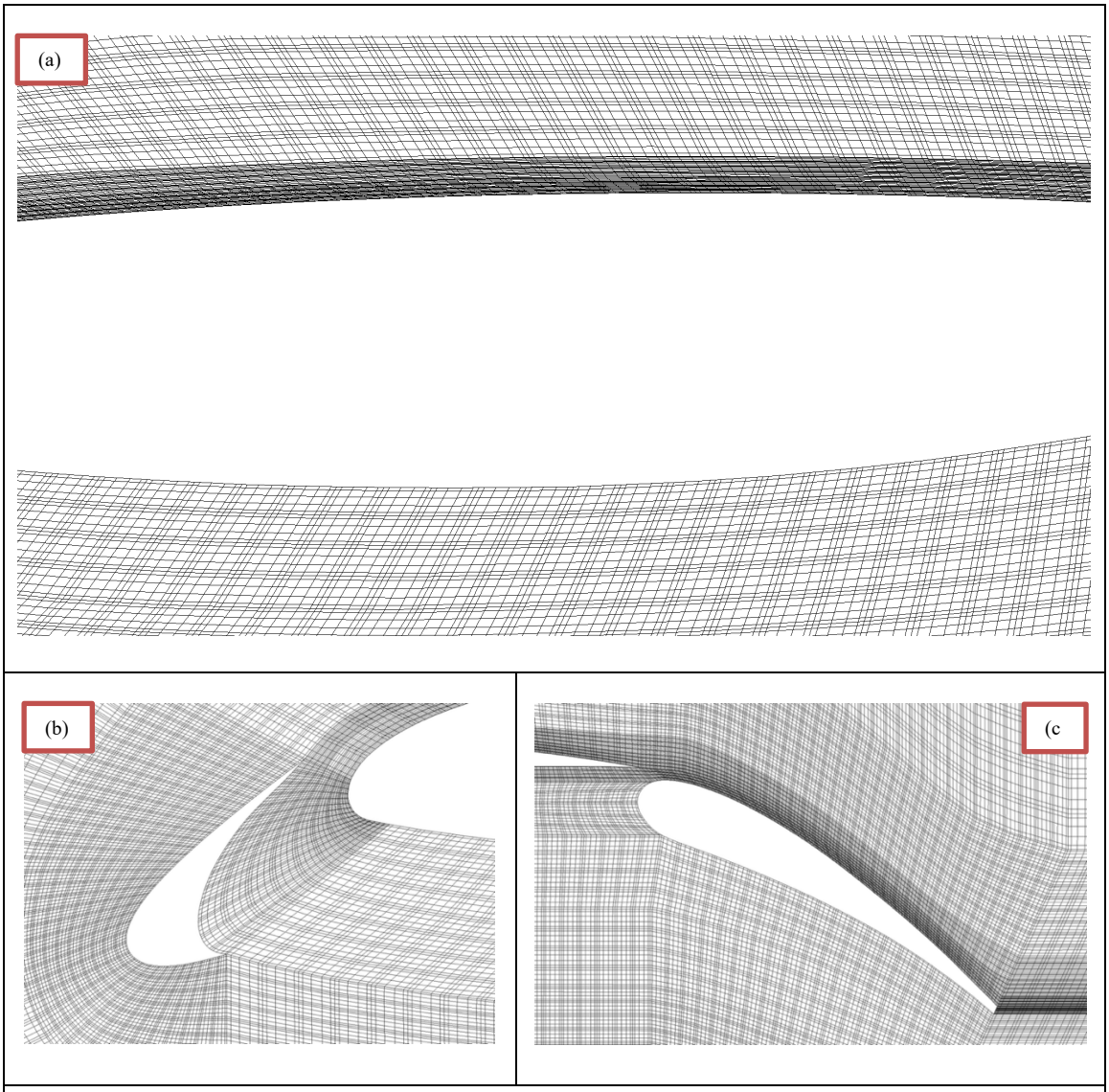

Figure 3:9: The Spectral-Element Grid with Mesh for Polynomial Order $N = 5$ in the Inflation Layers of Each Element of the 30P30N Three-Element Airfoil, Generated by Nek5000. (a) Main Element, (b) Slat, and (c) Flap

Overall, these modifications increased the total number of elements from 13,282 in 2D study in freestream [2-4] to 16,887 in the present study. Although the mesh size increased, the polynomial order was reduced from $N = 7$ in the previous study to $N = 5$ in the present study, maintaining a similar overall computational time without compromising the accuracy of the results. Additionally, there are slight changes in the boundary conditions compared to the previous study, which will be explained in detail in the Boundary Conditions section (Section 3.7).

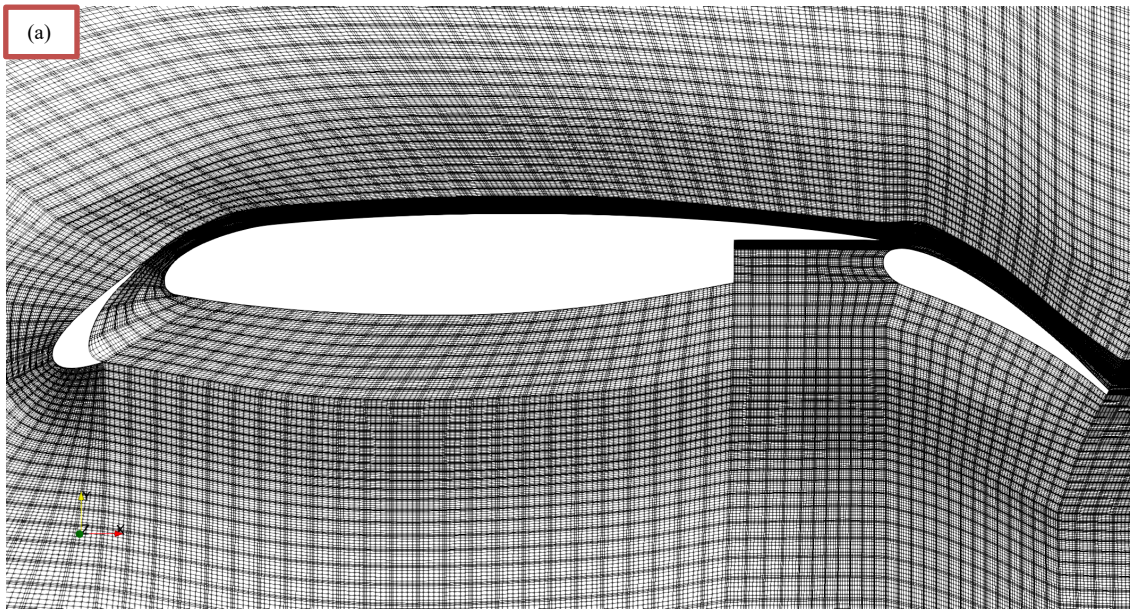

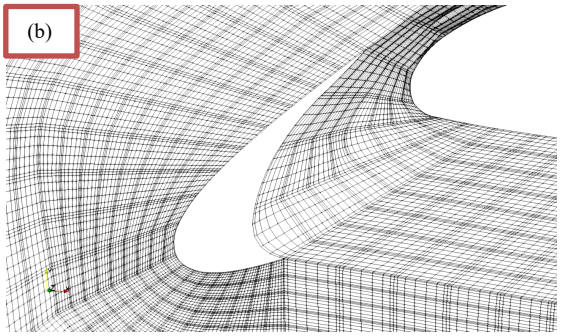

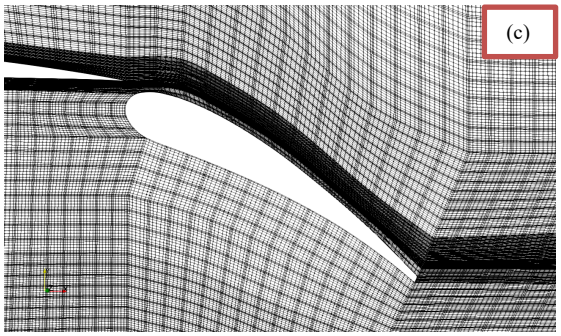

Figure 3:10: The Spectral-Element Grid with Mesh for Polynomial Order $N = 7$, of the 30P30N Three-Element Airfoil Used in Freestream Case Simulation [2-4], Generated by Nek5000. (a) Inflation Layers of the 30P30N Airfoil, (b) Slat, and (c) Flap

3.6 Flow Parameters

The present simulations are governed by the incompressible Navier-Stokes equations (see Section 3.1). Accordingly, the key flow parameter considered is the chord-based Reynolds number, Re_c, defined as:

$$Re_c = \frac{\rho U_\infty c}{\mu}, \quad (3.15)$$

where ρ is the density set to 1, U_∞ is the freestream velocity set to 1, c is the unit stowed-chord length, and μ is the dynamic viscosity. In the present simulation, dynamic viscosity is defined based on the chord-based Reynolds number Re_c ,

$\mu = \frac{1}{Re_c}.$	(3.16)

With the free-stream velocity fixed at $U_\infty = 1$, this formulation enables the Re_c to be varied directly by adjusting μ, which is specified in the Nek5000 parameter file (*.par*).

3.7 Initial and Boundary Conditions

The initial and boundary conditions for the present simulations are specified in the .usr and .par files in Nek5000. The computational domain is initialized with a uniform free-stream velocity $U_\infty = 1$ as the initial condition, implemented in the *.usr* file. Specifically, the streamwise (u) and wall-normal (v) velocity components are prescribed as:

$u = U_\infty \cos \alpha$ and $v = U_\infty \sin \alpha$,	(3.17)

where $\alpha = 4°$ is the AoA considered in this study, as described in Section 3.3.2

Boundary conditions are applied using identifiers assigned in Gmsh, which is consistent with Figure 3.2, and these identifiers corresponding to specific edge boundaries are specified in the .par file to assign the appropriate boundary conditions.

The inlet is defined with a user-specified, constant velocity (v) boundary condition, which is a Dirichlet boundary condition. The surfaces of the airfoil, including the slat, main element, and flap are defined with a wall (W) boundary condition, representing a no-slip Dirichlet boundary condition. The outlet is defined as an outflow or open (O) boundary condition, representing a Neumann boundary condition. This outflow boundary condition represents a natural boundary condition arising from the variational formulation of the incompressible Navier-Stokes equations. The no-stress formulation of the outflow boundary condition used in the present study is given by:

$[-p\mathbf{I} + \mu(\nabla \mathbf{u})] \cdot \mathbf{n} = 0$	(3.18)

where **I** is the identity tensor, μ is the dynamic viscosity, and **n** is the unit normal vector. Furthermore, the outflow is stabilized by implementing a sponge forcing function, as discussed in the following section.

In the previous study by Vadsola et al., [2-4], Neumann boundary conditions were imposed on the top and bottom boundary of the computational domain. The velocity components are specified as follows:

$\frac{\partial \mathrm{u}}{\partial y} = 0.$	(3.19)

In the present study, a different set of boundary conditions is employed, as described below. The inlet velocity is prescribed on both the left and bottom boundaries (as shown in Section 3.2.2). The velocity components (u, v) (see Equation 17) are defined such that their resultant corresponds to a free-stream velocity of unit magnitude U_∞. The left boundary is thus assigned a uniform velocity of magnitude U_∞, oriented at an AoA, α = 4° relative to the airfoil. Similarly, the bottom boundary is prescribed with the same velocity components (u, v), corresponding to U_∞ at α = 4°. Since the bottom boundary is already inclined at the angle of 4° as α, this treatment effectively mimics a moving ground boundary condition, consistent with the physical condition of an airfoil operating at AoA, α = 4°, in ground proximity. In this way, the relative motion between the airfoil and the ground is accurately represented, with the ground modelled as moving at an angled U_∞ in the opposite direction to the airfoil motion.

In all simulations, no external disturbances are applied; thus, the flow transitions to turbulence naturally, driven only by numerical perturbations arising from round-off and truncation errors.

3.8 Sponge forcing

During preliminary simulations, it was observed that, due to the intensity of vortex shedding, backflow occurred at the outlet boundary, which destabilized the solution and, in some cases, caused numerical blow-up. To address this, a sponge layer was implemented near the outlet on the right boundary of the computational domain to gradually damp

vortical structures before they exited the domain. This damping is achieved using a sponge forcing function applied to the outflow region (right boundary), which helps maintain numerical stability by preventing non-physical reflections and backflow. The need for the sponge layer is particularly pronounced in the present study due to the relatively short downstream distance between the trailing edge of the flap and the outlet boundary, given the Reynolds number considered [2][51]. By absorbing energy from the vortical structures, the sponge layer ensures a smooth transition of the flow out of the domain while preserving the physical accuracy of the simulation.

The sponge forcing function utilized in this study was originally developed by Schrader et al. [54][55]. In the present implementation, it is based on the "Spongebox" module within the KTH framework for Nek5000 toolboxes, as described in the GitHub repository maintained by Massaro et al. (2024) [56]. This function drives the flow toward a specified reference velocity using a volumetric forcing term. For the current simulations, the sponge layer was applied to a small region in the streamwise direction, corresponding to 10% of the stowed chord length at the end of the computational domain, immediately upstream of the outflow boundary condition. The sponge forcing function is defined as follows:

$$F(x,t) = \lambda_f(x)\left[U_f(x) - U(x,t)\right], \quad (3.20)$$

where U_f denotes the target forcing velocity, which is set to a unit value in the present simulations, and U represents the instantaneous velocity.

The λ_f is the sponge function, defined as:

$$\lambda_f(x) = \lambda_{max}\left[S\left(\frac{x_{min} + \Delta_{wl} - x}{\Delta_{dl}}\right) - S\left(\frac{x - x_{max} + \Delta_{wr}}{\Delta_{dr}}\right)\right], \quad (3.21)$$

where λ_{max} represents the sponge strength, and S(x) is a step function defined by Equation (3.22). The parameters Δ_{wl} and Δ_{wr} correspond to the widths of the left and right sponge sections, respectively, while Δ_{dl} and Δ_{dr} denote the drop widths of the left and right sponge sections.

$S(x) = \begin{cases} 0 & x \leq x_{min} \\ 1/(1+e^{((x-1)+x^{-1})}) & x_{min} < x \leq x_{max} \\ 1 & x > x_{max} \end{cases}$	(3.22)

Table 3.3: Sponge Forcing Parameter Used in the Present Study

Term	Spongebox variables	Value
λ_{max}	strength	100.0
Δ_{wl}	widthlx	0.2
Δ_{wr}	widthrx	0.2
Δ_{dl}	droplx	0.1
Δ_{dr}	droprx	0.2

For the present study, the sponge zone extends between x_{min} = 0.02 and x_{max} = 0.98, where these values are defined relative to 98% of the selected sponge region. For the cases considered in this study, the parameters specified in the "Spongebox" code to configure the sponge layer are listed in the Table 3.3 and were used to enforce the desired reference velocity corresponding to the Reynolds number employed in this study.

3.9 Computation Time and Visualization

The computations were carried out on the HPC systems of the Digital Research Alliance of Canada [57], specifically on the Niagara and Cedar (currently known as Fir) clusters. Both clusters were used for the simulations of the cases considered in this study. The Nek5000 spectral element solver employed in this study is highly scalable and has been successfully tested on Peta-scale systems, as reported by N. Offermans et al [58]. The number of cores and nodes utilized on each cluster is provided in Table 3.4, along with the wall-clock time required to generate one flow-through dump, averaged over the simulation cases. The average computational time per flow-through for the different cases is summarized in Table 3.5. The total data generated for the three cases simulated in this study was approximately 300 GB. This data was subsequently visualized for analysis, as discussed later in this section.

Table 3.4: Computational Time for Each Cluster Along with Corresponding Node and Core Usage

Cluster	**Number of Nodes**	**Total Number of CPU cores**	**Wall Clock Computational Time Per Flow Through (Hr)**
Niagara	1	80	1.5
Cedar (Fir)	6	90	1.25

Table 3.5: Average Computational Time for Different Simulated Cases

Case	**Ground-Clearance Ratio, h/c**	**Re_c**	**AoA**	**Wall Clock Computational Time Per Flow Through (Hr)**
Case 1	1.0	1.27×10^4	4°	1.5
Case 2	0.8	1.27×10^4	4°	1.3
Case 3	0.6	1.27×10^4	4°	1.2

The computational outputs were transferred from the HPC clusters to a personal workstation (MacBook Pro) for post-processing and visualization. Nek5000 generates a metafile along with the associated data files, which were employed for flow visualization. ParaView [59][60], an open-source, high-performance software widely used for CFD post-processing, was the primary tool utilized to visualize and analyze the flow features presented in the Results section. In addition, MATLAB [61] was employed for further quantitative analysis of the processed data extracted from ParaView.

The visualization and analysis were performed on a personal workstation with 32 GB unified memory, an 18-core GPU, and a 12-core CPU, which enabled efficient handling of the large datasets (approximately 300 GB). The visualizations and insights obtained from these tools form the basis of the discussions presented in the following section.

Chapter 4

Results and Discussion

This chapter presents and discusses the results obtained from two-dimensional numerical simulations of flow over the 30P30N multi-element airfoil in ground proximity, performed using Nek5000. The study considers different ground clearance ratios, h/c = 1, 0.8, and 0.6 at a chord-based Reynolds number of Re_c = 1.27 x 10^4 and an angle of attack AoA, α = 4°.

The chapter is organized as follows: Section 4.1 presents the grid convergence study conducted for the present work. Section 4.2 examines the instantaneous velocity magnitude fields to highlight the unsteady flow features over the airfoil. Section 4.3 discusses the time-averaged velocity magnitude fields obtained by averaging the instantaneous results, providing insights into the persistent flow structures. Section 4.4 analyzes the streamwise u-velocity fields superimposed with velocity streamlines to illustrate recirculation regions and wake development over the airfoil geometry. Section 4.5 presents the instantaneous vorticity fields, detailing shear layer separation and vortex roll-ups, while Section 4.6 discusses the time-averaged vorticity fields to capture the persistent vortical structures. Section 4.7 evaluates the streamwise mean velocity, u_s profiles at different chordwise locations. Finally, Section 4.8 focuses on the aerodynamic metrics, including lift, drag, and pressure coefficients, to examine their variation under the influence of ground effect.

All the results discussed in the following sections are based on simulations run and time-averaged over approximately 10.5 flow-throughs. A single flow-through is defined as the time required for a free-stream fluid particle to travel from the left inlet boundary to the right outlet boundary. The results are compared across the three ground clearance ratios considered in this study and further benchmarked against the freestream condition investigated by [2-8] with a similar flow configuration

4.1 Grid Independence Study

A critical component of any numerical simulation is the grid independence study, which ensures that the computed results are not influenced by grid resolution . In other words, the grid independence study demonstrates that further mesh refinement does not lead to significant changes in the predicted flow features or aerodynamic coefficients, thereby confirming that the chosen grid resolution is sufficient to capture the essential flow physics

with accuracy and efficiency. This step is particularly important in high-fidelity simulations, where resolving fine-scale structures such as separation bubbles, shear layers, and wake vortices directly impacts the reliability of the results.

As discussed in Chapter 3, Section 3.5, after finalizing the grid and element mesh in Gmsh with a precise number of elements to capture the dominant flow dynamics around the 30P30N airfoil configuration, the mesh was imported into Nek5000. In Nek5000, additional refinement is achieved through the spectral element method. The grid is composed of quadrilateral elements, within which the solution is represented as a tensor product of N^{th} order Legendre polynomials in each spatial direction. Increasing the polynomial order N enhances the effective resolution of the solution without modifying the number of elements, thereby improving the accuracy of the flow field representation. Each element contains $N+1$ collocation points per direction, so higher values of N provides a denser distribution of points and enable the resolution of finer-scale flow features.

The grid independence study was carried out by increasing the polynomial order from N = 5 ($N+1$ = 6 collocation points) used in the present simulations to N = 7 ($N+1$ = 8 collocation points) to evaluate the variation in results. Specifically, the time-averaged lift and drag coefficients were compared between the two polynomial orders for the ground clearance case of h/c = 1 at an Re_c = 1.27 x 10^4 at an AoA of 4°. In addition, instantaneous velocity magnitude fields were examined at approximately the same physical time to assess variations in local flow features. The comparison of the time-averaged lift and drag coefficients is presented in Table 4.1, and the instantaneous velocity field comparisons are shown in Figures 4.1 and 4.2.

Convergence was established when further increases in N yielded negligible differences, thereby validating the adequacy of the selected resolution for the present DNS analysis

Table 4.1: Time-Averaged Lift and Drag Variation between Polynomial order N = 5 and N = 7, for Ground Clearance h/c = 1 at Re_c = 1.27 x 10^4 at AoA = 4°

Order N	**C_L**	**C_L Variation (%)**	**C_D**	**C_D Variation (%)**
5	1.6572	-	0.0479	-
7	1.6451	**0.73**	0.0477	**0.41**

From Table 4.1, it is observed that the variation in the drag coefficient (C_D) between polynomial orders N = 5 and N = 7 is only 0.41%, while the corresponding change in the lift coefficient (C_L) is 0.73%. These small differences indicate that increasing the

polynomial order does not lead to any substantial change in the aerodynamic parameters.

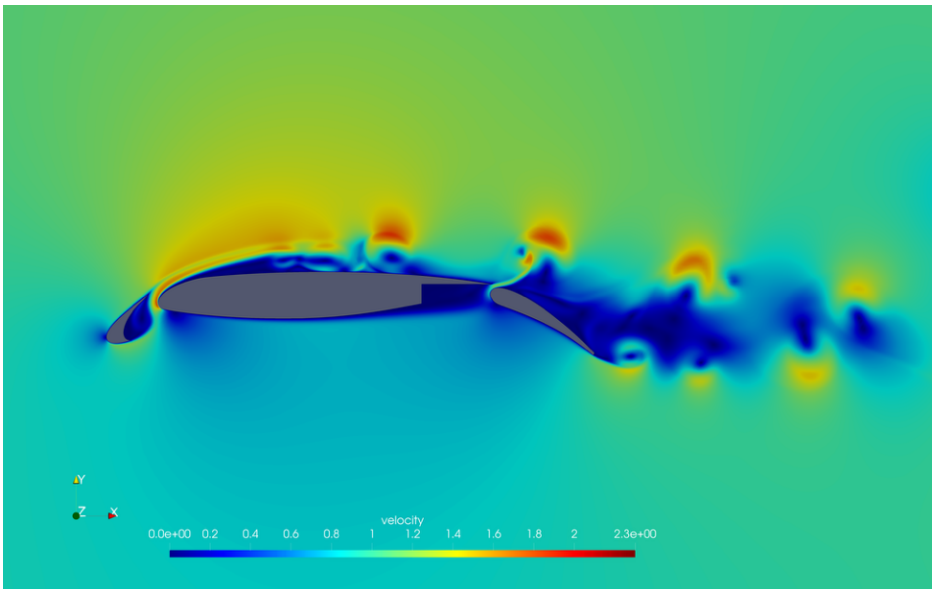

Figure 4:1: Instantaneous Velocity Magnitude Field for Ground Clearance Ratio h/c =1 (Simulation Run with Polynomial Order N = 5, in Each Direction)

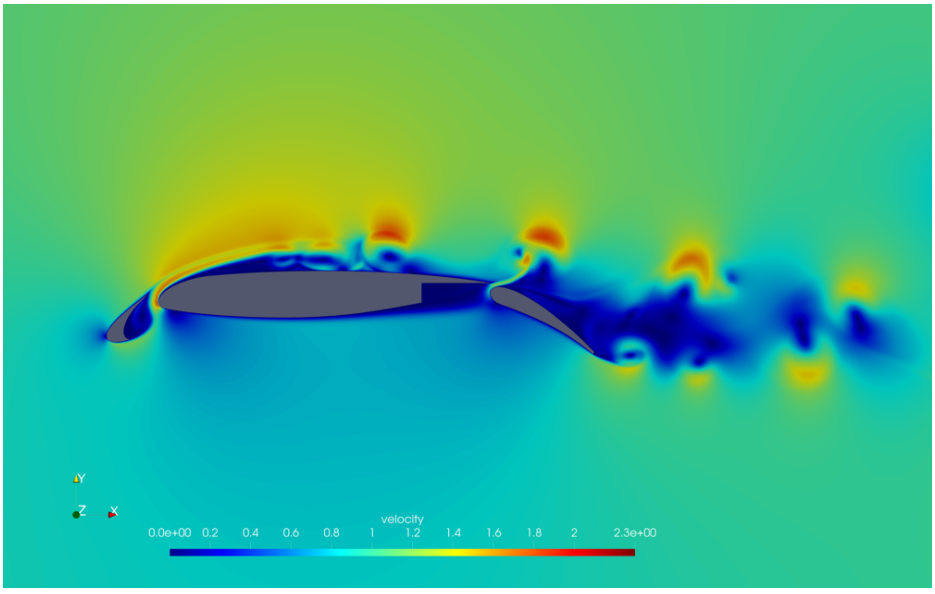

Figure 4:2: Instantaneous Velocity Magnitude Field for Ground Clearance Ratio h/c =1 (Simulation Run with Polynomial Order N = 7, in Each Direction)

This observation is further supported by comparing Figures 4.1 and 4.2, which show that the velocity magnitude fields are nearly identical for both polynomial orders. Therefore, no significant differences in flow features or aerodynamic metrics are found between N = 5 and N = 7, confirming grid independence. Consequently, the resolution with N = 5 ($N + 1$ = 6 collocation points) is considered adequate (at < 1% change) to capture the flow structures with sufficient accuracy, while also reducing computational cost and improving overall efficiency.

4.2 Instantaneous Velocity Magnitude Field

In this section, the instantaneous velocity profiles over the 30P30N airfoil are analyzed to capture the detailed flow features and transient phenomena. These reveal the location of stagnation points, regions of flow separation, and the development of recirculation and separation bubbles over the slat, main element, and flap. The instantaneous fields also highlight shear layer roll-ups, vortex shedding, and the breakdown of vortical structures, as well as the formation of slot jets in the gaps between airfoil elements. Additionally, the evolution of the wake and its interaction with upstream separated layers are examined. Together, these observations provide a comprehensive view of the unsteady flow physics and underlying mechanisms governing the aerodynamic performance of the airfoil under different ground proximities. Figures 4.3-4.5 illustrate the instantaneous velocity magnitude fields for the three ground-clearance ratios, h/c = 1.0, 0.8 and 0.6

4.2.1 Slat

As the flow encounters the airfoil at an angle of attack of 4°, a stagnation point forms at the nose of the slat. From this point, the flow accelerates along both the upper and lower surfaces of the slat. The flow on the lower surface undergoes separation and meanders within the slat cove region and undergoes complex recirculation [5]. It subsequently reattaches near the slat trailing edge, generating a separation bubble within the slat cove region. Downstream of the trailing edge, this reattached flow separates again and merges with the boundary layer separating from the slat's upper surface, before convecting further downstream over the main element. A detailed analysis of this interaction is provided in the u-velocity and vorticity sections. Notably, the separation bubble observed in the slat cove region in the present study is comparatively smaller than that reported under free-stream condition [2][4]. In the current study, it is also revealed that the slat cove bubble 'breathes,' periodically expanding and contracting as the flow passes.

4.2.2 Main

The incoming main flow encounters the leading edge of the main element, forming a stagnation point on the lower surface relative to the 4° angle of attack. The flow then accelerates rapidly around the leading edge, attaining its maximum velocity before being progressively decelerated under the influence of the adverse pressure gradient (APG). This APG causes the boundary layer to separate at approximately $x/c \approx 0.16$ (as identified in the skin-friction coefficient distribution, see C_f section), giving rise to a free shear layer, referred to as SL_{M1} (see vorticity section).

As the shear layer develops along the chord, its interaction with the shear layer shed from the slat trailing edge induces disturbances that become evident slightly upstream of mid-chord ($x/c \approx 0.4$). These disturbances manifest as oscillatory, wave-like velocity structures within the separated shear layer. These are caused by Kelvin-Helmholtz (K-H) instability in the separating shear layers. Further downstream, the shear layer undergoes roll-up and vortex shedding, forming a sequence of coherent vortical structures. Beyond the mid-chord region, these vortices progressively break down and reattach onto the main-element surface, leaving behind a cloud of low-velocity fluid that is convected downstream.

4.2.3 Main-Flap

As the low-velocity clouds move through the main-flap gap between the trailing edge of the main element and the flap, they displace the high-momentum flow from beneath the airfoil, generating a periodic jet into the main-flap gap. This jet formation arises due to the interaction between the high-velocity underflow and the passing low-velocity cloud. The periodic jet is observed approximately 15-19 times per flow-through, depending on the h/c ratio. In the absence of these low-velocity clouds, the high-momentum flow from beneath the airfoil enters the main-flap gap smoothly, forming a continuous streak along the flap rather than a plunging jet.

4.2.4 Flap

Downstream, the flow separates over the flap due to its geometric angle, failing to reattach and continuously shedding vortices, which establish a coherent wake behind the flap. The angle and intensity of this wake vary with the h/c ratio, showing noticeable changes as the airfoil approaches the ground (h/c decreasing from 1.0 to 0.6), discussed further in the average velocity magnitude field section.

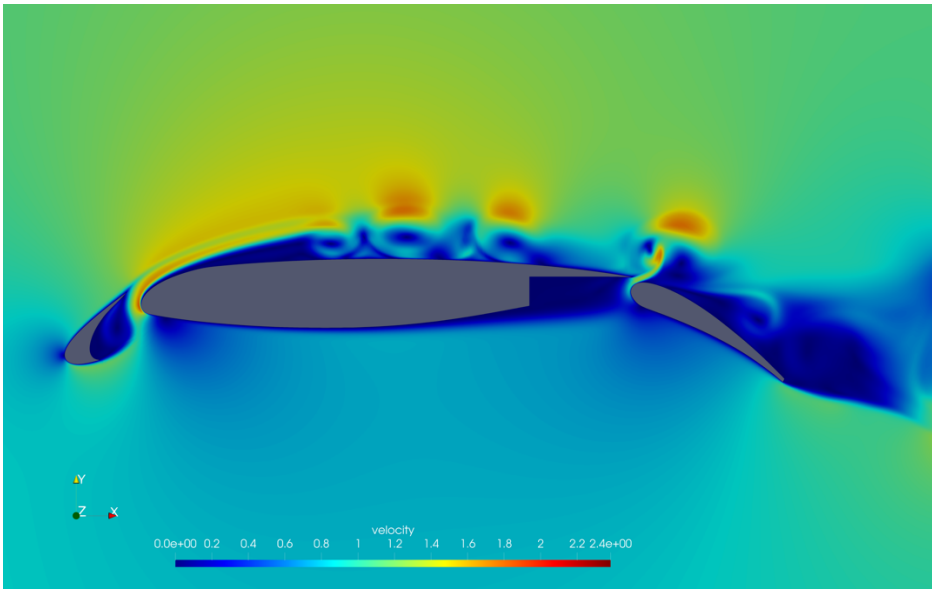

Figure 4:3: Instantaneous Velocity Magnitude Field for Ground Clearance Ratio h/c = 1

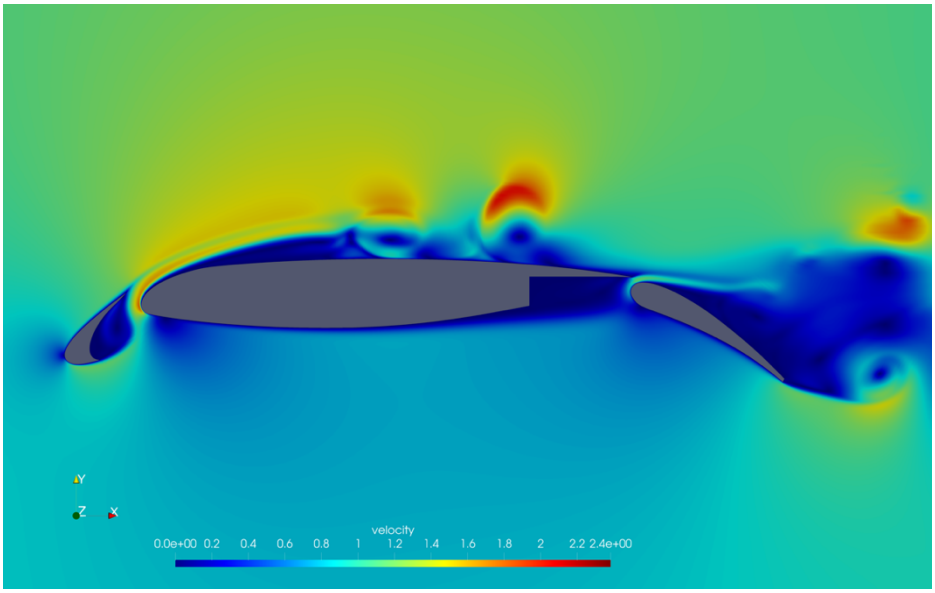

Figure 4:4: Instantaneous Velocity Magnitude Field for Ground Clearance Ratio h/c= 0.8

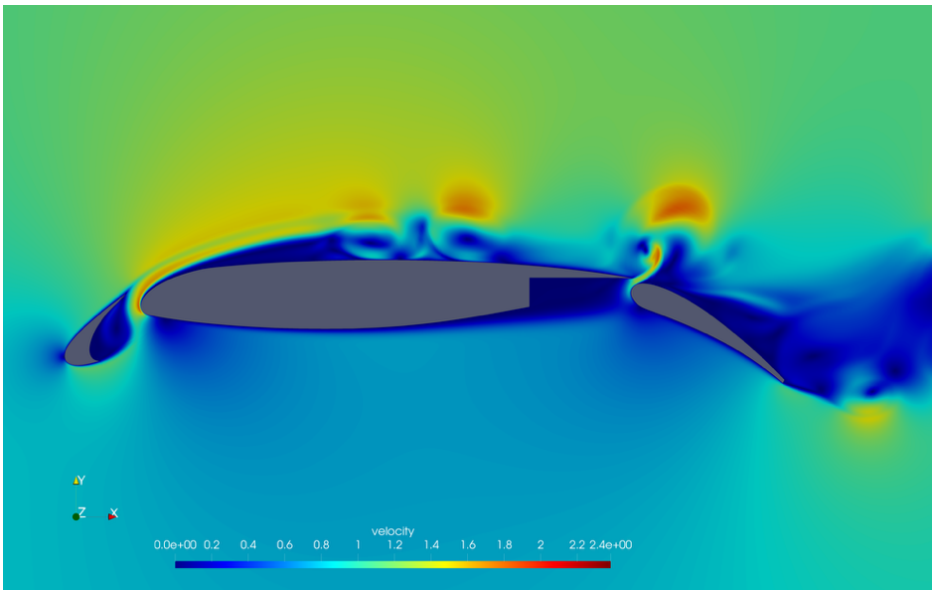

Figure 4:5: Instantaneous Velocity Magnitude Field for Ground Clearance Ratio h/c = 0.6

4.3 Time-Averaged Velocity Magnitude Field

To complement the observations from the instantaneous velocity magnitude fields, the time-averaged velocity magnitude provides a clearer representation of the persistent flow structures and overall trends across the 30P30N airfoil. Figures 4.6 - 4.8 presents the time-averaged velocity magnitude fields for the three h/c ratios 1, 0.8, and 0.6, respectively. While the instantaneous fields capture transient phenomena such as shear layer interactions, roll-ups, periodic jets, and vortex shedding, the averaged fields highlight the mean distribution of high- and low-momentum regions, the steady wake behind the flap, and the influence of ground proximity (h/c ratio) on the flow topology.

The peak velocity remains consistently located near the leading edge of the main element-driven by the slat cove separation bubble and the accelerated mainstream flow through the slat-main gap while the overall maximum and minimum velocity magnitudes remain nearly unchanged across the three configurations. These averaged fields allow quantification of flow acceleration, deceleration, and the extent of separation zones, providing a consistent basis for comparing the effects of different h/c ratios on aerodynamic performance.

4.3.1 Slat

The time-averaged velocity magnitude over the slat reveals sustained flow acceleration above and below the stagnation point, while also clearly delineating the boundary-layer separation on both surfaces of the slat. The separation bubble in the slat cove appears more distinct and persistent, consistent with but more defined than in the instantaneous velocity fields, manifesting as a low-velocity ring structure. The size of this separation bubble decreases with the ground clearance ratio.

4.3.2 Main

Over the main element, the time-averaged velocity magnitude field closely resembles the instantaneous field near the leading edge, reaffirming the boundary-layer separation at approximately $x/c \approx 0.16$. In the averaged plots, this separation is more clearly defined, followed by reattachment slightly downstream of the mid-chord. Above the separated boundary layer from the main element, a second shear layer originating from the slat develops. This shear layer is convected downstream in parallel to the main-element shear layer upto approximately mid-chord, before the two begin to interact.

The wave-like disturbances observed in the instantaneous velocity field, arising from the downstream interaction between the main-element shear layer and the slat trailing-edge shear layer due to the Kelvin-Helmholtz (K-H) instability, vanish in the time-averaged field. Instead, the averaged field reveals a large recirculation bubble with subsequent reattachment over the main element (discussed further in the u-velocity section). Although less pronounced than the instantaneous fluctuations, these averaged structures delineate persistent low-velocity regions associated with the mean recirculation and roll-up zones.

For decreasing h/c from 1.0 to 0.6, the separated shear layer shifts away from the wall, delaying reattachment and resulting in a thicker, longer recirculation bubble over the main element, indicating the influence of ground proximity on boundary-layer recovery. This behaviour is clearly visible in the time-averaged velocity magnitude fields, although the overall flow field over the main element among the different h/c remains largely unchanged apart from these minor differences. Together, these observations highlight the ground effect on boundary-layer behavior and the modulation of shear layer interactions.

4.3.3 Main-Flap

The periodic jet observed in the instantaneous velocity field within the main-flap gap manifests in the time-averaged field as a continuous flow connecting the gap to the region above the airfoil. Similarly, the streak that forms in the absence of low-velocity clouds in the instantaneous field appears as a faint, elongated streak extending slightly over the flap

within the wake region. This averaged structure reflects the residual influence of the periodic jets and streaks, highlighting the persistent flow pathways in the main-flap gap.

4.3.4 Flap

The chaotic vortex shedding from the flap, evident in the instantaneous velocity fields, forms a well-defined wake when averaged in time. Across the three h/c ratios, the time-averaged wake exhibits a similar overall trend and structure, with only minor variations. As h/c decreases, the wake appears slightly narrower; however, this effect is subtle in the averaged velocity magnitude fields (see Figures 4.6 - 4.8). The narrowing becomes more discernible through the reduction in pressure drag, as reflected by the decreasing C_{D_p} values discussed in the Lift and Drag Coefficients section.

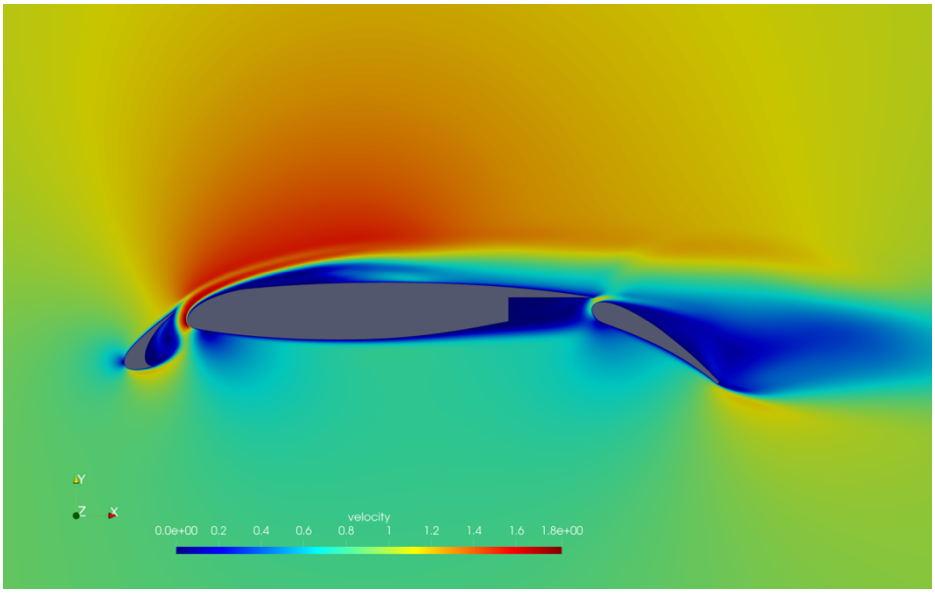

Figure 4:6: Time-Averaged Velocity Magnitude Field for Ground Clearance Ratio h/c=1

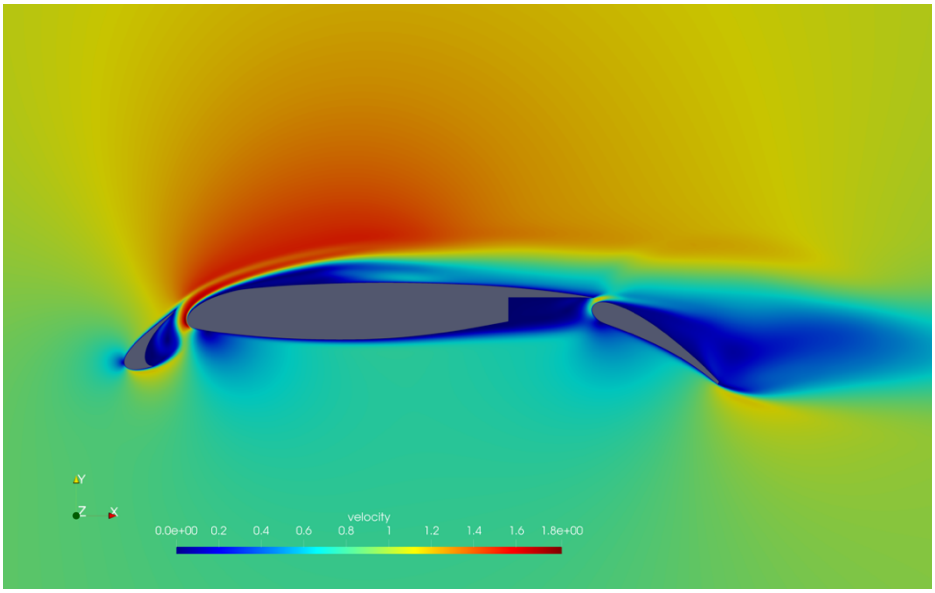

Figure 4:7: Time-Averaged Velocity Magnitude Field for Ground Clearance Ratio h/c = 0.8

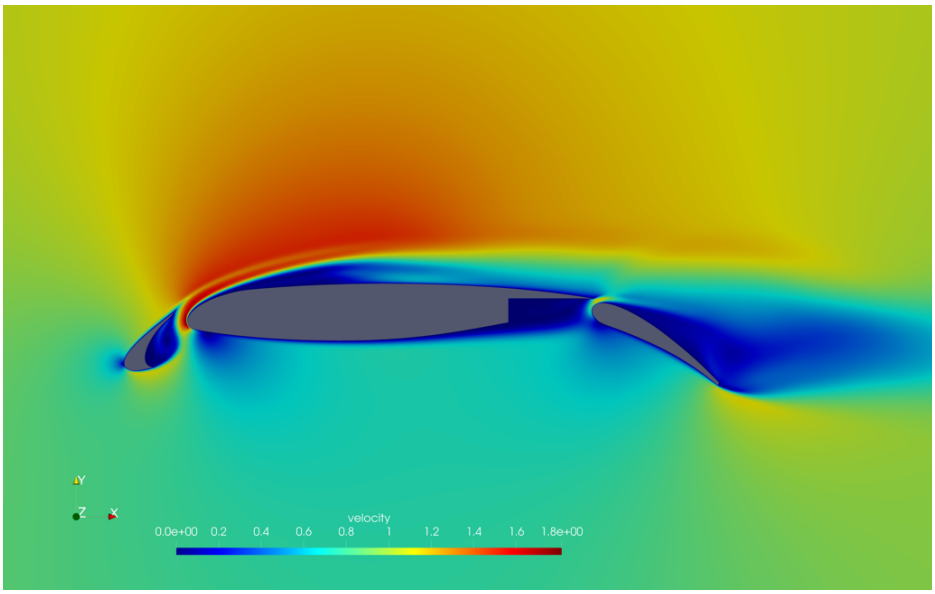

Figure 4:8: Time-Averaged Velocity Magnitude Field for Ground Clearance Ratio h/c = 0.6

4.4 Time-Averaged u-Velocity Field

Building on the instantaneous and time-averaged velocity magnitude fields, this section examines the mean u-velocity field (time-averaged x-velocity component) to further elucidate the underlying flow physics over the 30P30N airfoil. For each h/c ratio, the mean u-velocity field is superimposed with velocity streamlines, providing a clear representation of the flow organization. This combined visualization highlights the behaviour of the flow within the slat cove, over the main element, and in the wake region downstream of the airfoil. By correlating the mean u-velocity distribution with the streamline patterns, the formation and extent of recirculation bubbles, together with the mechanisms of separation, reattachment, and wake development, can be systematically compared across the different h/c cases.

Figures 4.9 - 4.11 present the mean u-velocity field superimposed with velocity streamlines for the three ground-clearance ratios, h/c = 1.0, 0.8, and 0.6, respectively. To provide further detail, Figures 4.12 -14 show close-up views of the slat, main element, and flap regions, respectively for the same cases, illustrating the local flow features more clearly. The labels used in the discussion are commonly presented in Figure 4.12, for reference. Further, the mean streamwise velocity field with superimposed streamlines for the free-stream condition is presented in Figure 4.15, providing a basis for comparison with the ground-effect cases.

4.4.1 Slat

The streamlines clearly illustrate the flow acceleration along the slat surfaces, both above and below, starting from the front stagnation point, shown in Figures 4.9 and 4.12(b), 4.10 and 4.13(b), and 4.11 and 4.14 (b) for h/c = 1.0, 0.8, and 0.6, respectively. They also highlight flow separations: one originating from the top surface of the slat, which moves over the main element, and another from the bottom surface, which enters the slat cove.

Separated flow from the slat's lower surface meanders within the slat cove and the slat-main gap, eventually reattaching near the slat trailing edge, forming separation bubbles (SB_{S1} and SB_{S2}) within the slat cove, as indicated by regions of low velocity. Two distinct separation bubbles are observed in the slat cove region: a smaller separation bubble (SB_{S1}), whose size remains relatively constant across different h/c ratios, and a larger separation bubble (SB_{S2}), which decreases in size as h/c decreases. This reduction in the size of the larger separation bubble (SB_{S1}) results in less meandering flow and earlier reattachment near the slat trailing edge. A similar trend has been observed in the literature, where increasing Reynolds numbers caused a comparable reduction in the size of the separation bubble 0[4][8]. These observations suggest that the ground effect may have effectively increased the local Reynolds number around the airfoil, particularly in the slat cove region.

Furthermore, the meandering flow in the slat cove then combines with the flow from above the slat, ultimately interacting with the flow over the main element further downstream.

4.4.2 Main

The stagnation point on the main element is clearly identified, where the streamlines diverge around the leading edge. Following the leading edge, the streamlines confirm the presence of flow separation, consistent with observations from the instantaneous and time-averaged velocity magnitude fields. Downstream, the separated streamlines reattach, giving rise to a large laminar separation bubble (SB_{M1}) over the main element. This feature is evident from the recirculating streamline pattern and the low-velocity region observed in Figures 4.9 - 4.11 and Figure 4.12 (a), 4.13 (a) and 4.14 (a).

In addition, a secondary separation bubble (SB_{M2}) develops beneath SB_{M1}. As h/c decreases, SB_{M2} shifts slightly downstream, a trend that becomes more apparent in the pressure-coefficient (C_p) and skin-friction (C_f) distributions sections. This secondary bubble typically forms around $x/c \approx 0.4$, coinciding with the onset of wave-like roll-ups observed in the instantaneous velocity magnitude fields. This correspondence suggests that SB_{M2} may be driven, at least in part, by these unsteady roll-up and wave structures at the same chordwise location. Supporting this, additional evidence of flow separation near $x/c \approx 0.4$ is also observed in both the vorticity field and further discussed in detail in the skin-friction (C_f) distribution sections.

The large separation bubble SB_{M1}, over the main element, is an averaged feature, consistently observed in both the time-averaged velocity magnitude and mean u-velocity fields. The reattachment points of this bubble shift downstream as h/c decreases, as evidenced by the streamline reattachment locations, which causes the recirculation region to lengthen and thicken. This trend suggests that, at smaller h/c ratios, the flow requires a longer distance to regain sufficient momentum to overcome the adverse pressure gradient and reattach. This behaviour may also be partially attributed to the ground effect, which increases the velocity angle through the slat-main, thereby thickening the separation bubble (as discussed in the following section) and consequently requiring a longer distance for reattachment compared to the free-stream case.

4.4.3 Main-Flap

Overall, the streamline patterns in the main-flap gap region are generally similar across all three h/c ratios (see Figures 4.9 - 4.11 and close-ups 4.12(c) - 4.14(c)). The streamlines originating from the lower surface of the main element are deflected upward through the gap, smoothly aligning with the flap surface and continuing downstream into the wake. This behaviour corresponds to the jet-like feature observed in the time-averaged velocity

magnitude fields, although here it manifests more as a redirected streak-like flow that attaches along the flap rather than a distinct plunging jet.

Simultaneously, the streamlines from the upper surface of the main element traverse the gap with only slight deflection, influenced by the upward momentum of the underflow, before continuing over the flap. This interaction between the upward-deflected underflow and the relatively undisturbed upper-surface flow establishes a coherent connection across the gap, consistent with the jet and streak structures identified in the time-averaged velocity magnitude analysis. Notably, flow separation at the top of the flap occurs at approximately the same chordwise location for each case.

4.4.4 Flap

The wake downstream of the flap is dominated by a large recirculating (RB_F) bubble that originates on the flap surface and extends slightly into the wake, along with a smaller secondary separation bubble (SB_F) closer to the trailing edge of the flap. These flow features are evident from the time-averaged u-velocity streamlines, as shown in Figures 4.9- 4.11 and Figures 4.12 (c), 4.13 (c), and 4.14 (c). The overall shape and structure of the wake are similar across all three h/c cases; however, the primary recirculating bubble on the flap is slightly inclined downward on the top compared to the wake recirculation bubble observed under free-stream conditions [4]. This downward inclination is likely influenced by the slot jet and the streak flow originating from the flap gap region, which redirects and modifies the trajectory of the wake.

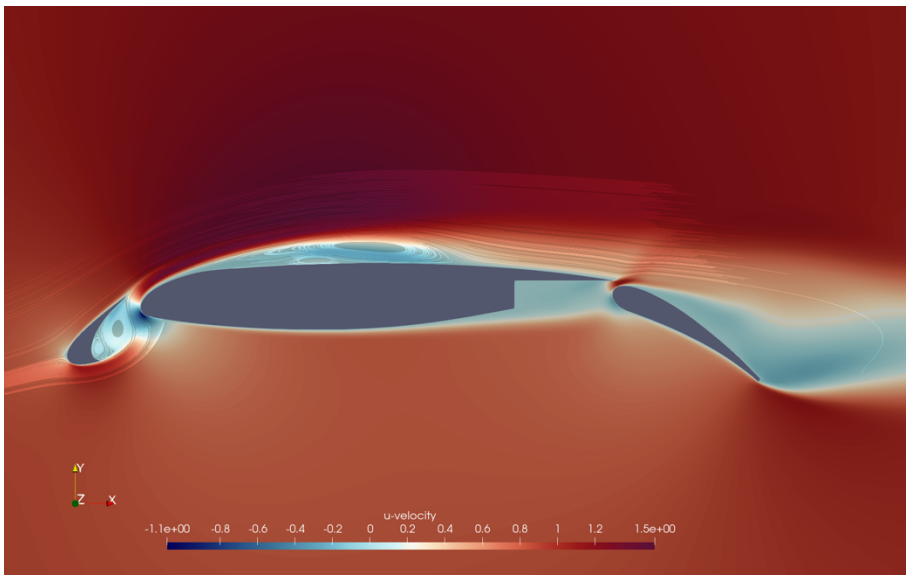

Figure 4:9: Time-Averaged u-Velocity Field with Streamlines for Ground Clearance Ratio h/c = 1

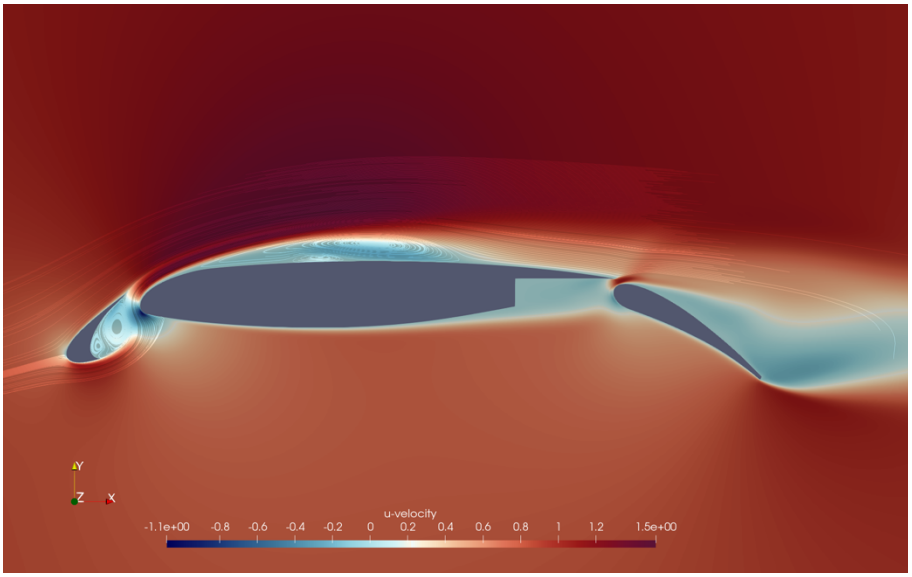

Figure 4:10: Time-Averaged u-Velocity Field with Streamlines for Ground Clearance Ratio h/c = 0.8

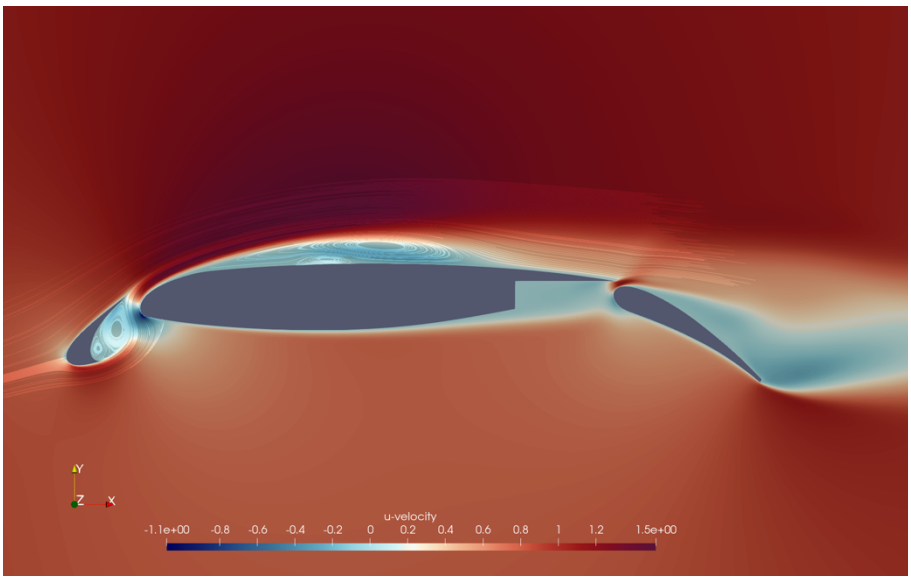

Figure 4:11: Time-Averaged u-Velocity Field with Streamlines for Ground Clearance Ratio h/c = 0.6

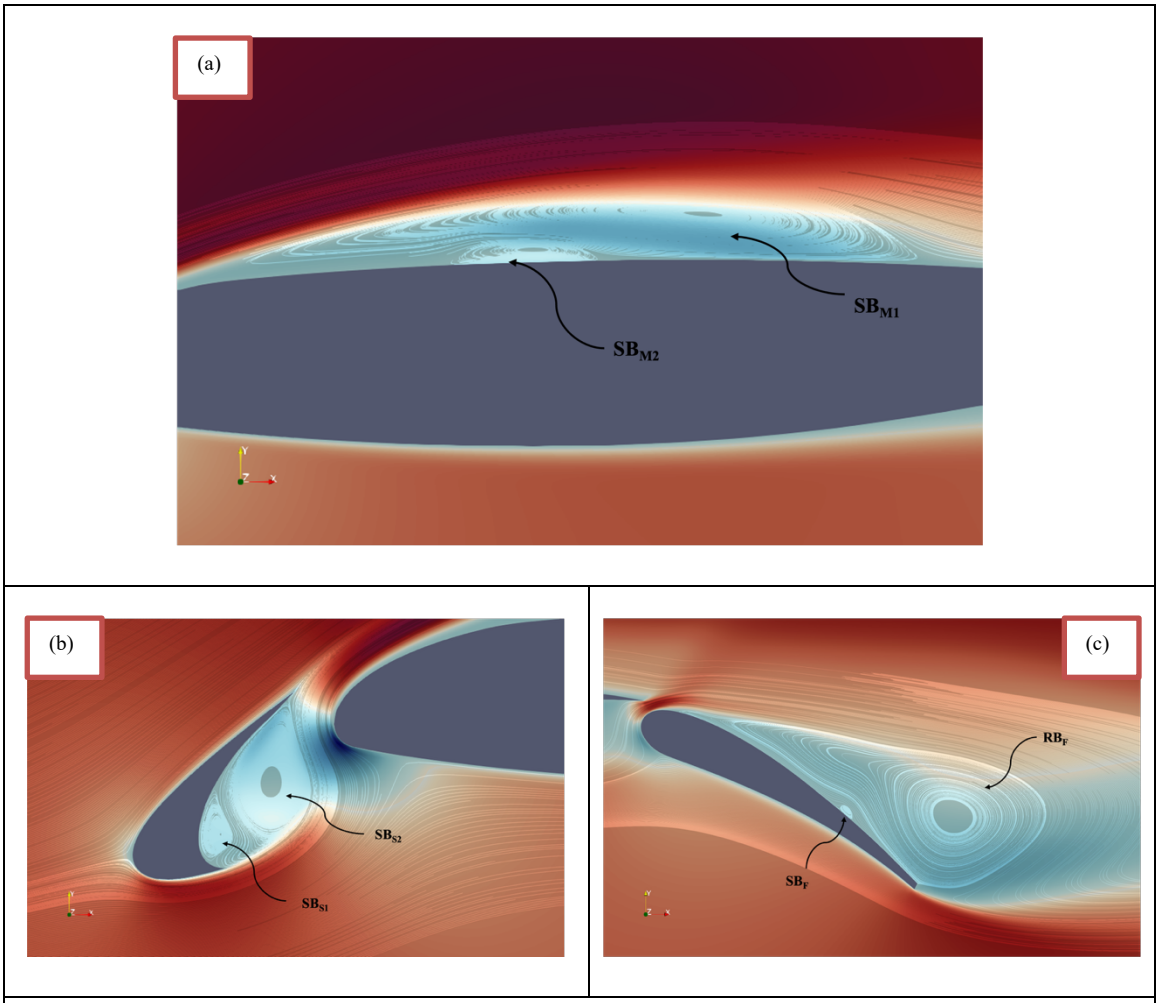

Figure 4:12: Time-Averaged u-Velocity Field with Streamlines for Ground Clearance Ratio h/c = 1, a) Main Element, b) Slat and c) Flap

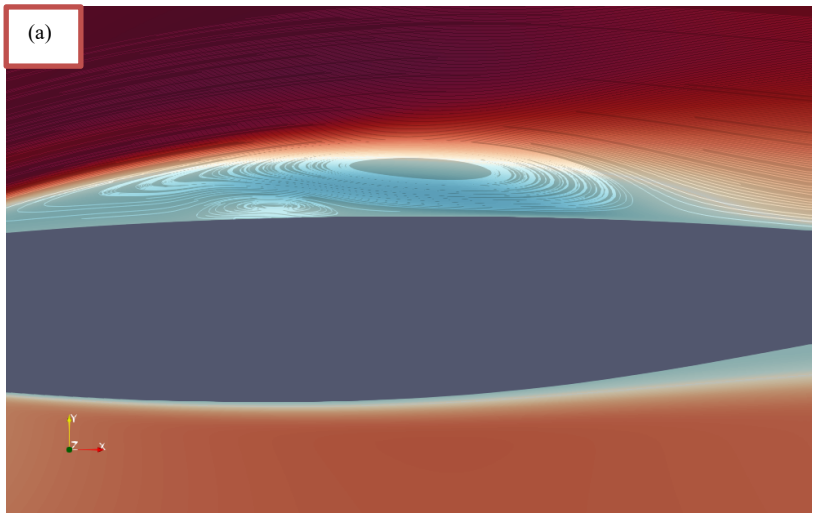

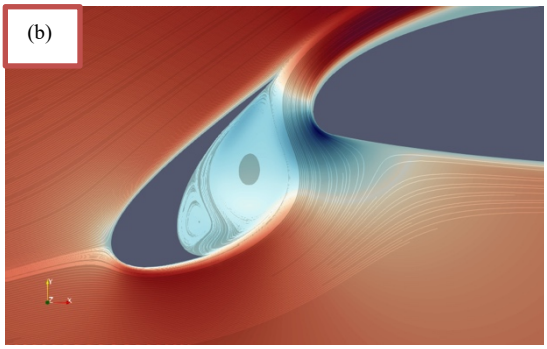

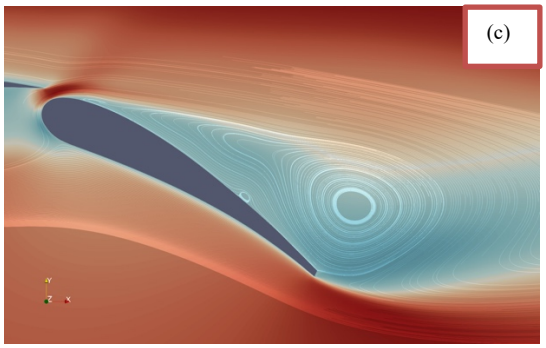

Figure 4:13: Time-Averaged u-Velocity Field with Streamlines for Ground Clearance Ratio h/c = 0.8, a) Main Element, b) Slat and c) Flap

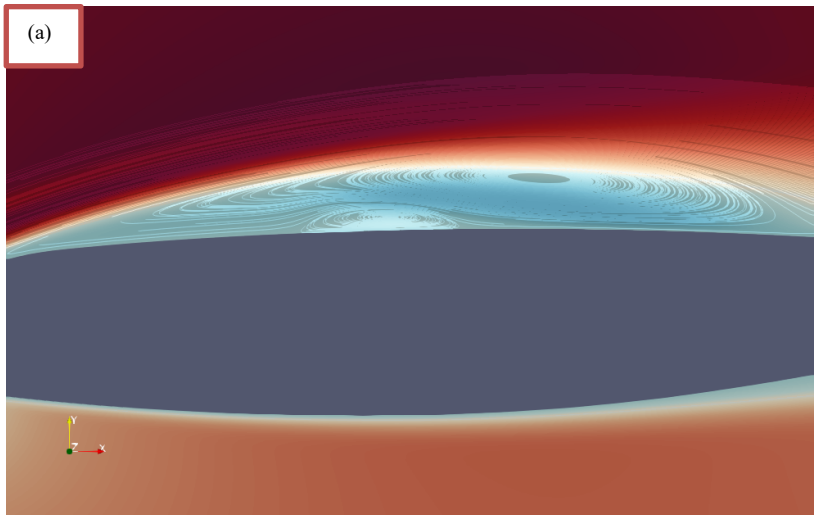

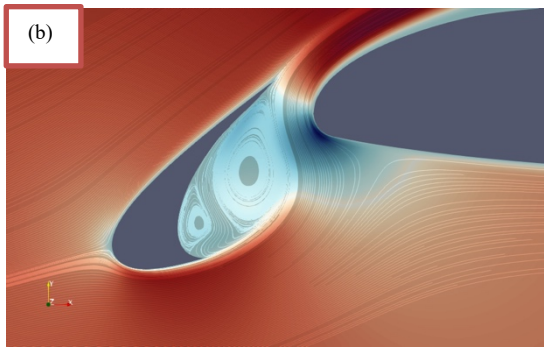

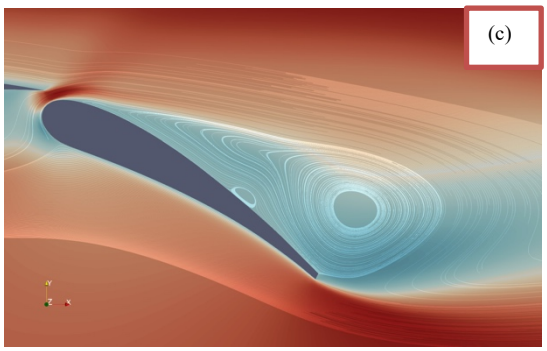

Figure 4:14: Time-Averaged u-Velocity Field with Streamlines for Ground Clearance Ratio h/c = 0.6, a) Main Element, b) Slat and c) Flap

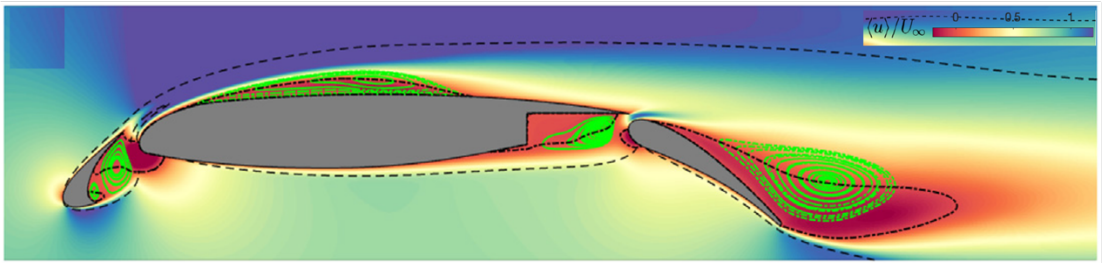

Figure 4:15: Time-Averaged u-Velocity Field with Streamlines for Freestream Condition [4]

4.5 Instantaneous Vorticity Field

In this section, the instantaneous vorticity fields are analyzed to investigate the unsteady flow structures over the 30P30N airfoil for different h/c ratios. These vorticity fields primarily highlight the behaviour of the separating shear layers and the formation of roll-up structures, and the location of separation bubbles, which were previously observed in the instantaneous velocity magnitude fields. Figures 4.16 - 4.18 present the instantaneous vorticity fields for h/c = 1, 0.8, and 0.6, respectively, enabling a comparative assessment of the shear layer evolution, roll-up strength, and separation phenomena across the different ground-clearance conditions. The labels used in the discussion are commonly presented in Figure 4.16, for reference.

4.5.1 Slat

The vorticity fields reveal the behaviour of the boundary layers separating from both the top and bottom surfaces of the slat, which were initially identified in the instantaneous and time-averaged velocity magnitude fields. These separated layers form free shear layers, denoted as SL_{S1} and SL_{S2}, originating from the top and bottom slat surfaces, respectively. The vorticity plots indicate that the shear layer SL_{S2}, separating from the bottom of the slat, is deflected by the main flow and meanders through the slat cove before reattaching near the trailing edge, as discussed in previous sections. This behaviour is influenced by the geometry of the slat, the curvature of the slat cove, and the leading edge of the main element.

The shear layer SL_{S2} does not exhibit vortex shedding; hence, the reattachment is laminar, leading to the formation of separation bubbles SB_{S1} and SB_{S2} within the slat cove, in agreement with observations reported in literature [2][4][5]. Among these, only the larger separation bubble, SB_{S2}, is prominently observable in both the instantaneous and time-averaged vorticity fields, as it represents the dominant recirculating structure within the slat cove. After reattaching near the slat trailing edge, the stronger SL_{S2} separates again and progresses downstream through the slat-main gap, extending over the main element up to approximately one-third of the chord. Meanwhile, the shear layer SL_{S1}, originating from the top of the slat, partially merges and travels above SL_{S2} as it extends over the main element along a similar chordwise distance.

4.5.2 Main

The shear layer SL_{M1}, separating from the leading edge of the main element as it encounters the adverse pressure gradient (APG), is clearly observed in the instantaneous vorticity fields. This shear layer is convected downstream beneath SL_{S1} and SL_{S2}, where it undergoes a Kelvin-Helmholtz (K-H) instability triggered by disturbances across the layer

and interactions with the surrounding shear flows. These instabilities give rise to wave-like roll-ups (RP), which were previously identified in the instantaneous velocity magnitude fields and are visible as swirling patterns in the instantaneous vorticity field. As h/c decreases, the onset of these wave roll-ups is delayed, indicating a slower transition.

These chaotic K-H induced roll-up structures (RP) mark the transition of the flow from laminar to turbulent. The roll-ups eventually trigger vortex shedding (VS) further downstream, which facilitates turbulent reattachment of the flow and leads to the formation of laminar separation bubbles (SB_{M1} and SB_{M2}) over the main element. Additionally, the origin of roll-ups contributes to the development of a secondary separation bubble SB_{M2} associated with the separating shear layer, SL_{M2}, as seen in the later time-averaged vorticity fields section. These phenomena are present across all h/c cases, although the intensity, frequency, and timing of the roll-ups and vortex shedding vary with h/c. The intensity of the roll up was is higher in the present study compared to the freestream case [2-8]. A smaller shear layer, SL_{M3}, partially responsible for the slot jet and streak, separates from the lower trailing edge of the main element and extends into the main-flap gap region.

4.5.3 Main flap

A stagnation point is observed at the lower leading edge of the flap. Flow moving above this point generates a shear layer, SL_{F1}, which travels through the slat-main gap and eventually separates. The plunging jet and streak observed in the instantaneous velocity magnitude fields arise from the combined contributions of SL_{F1} and SL_{M3} as they pass through the main-flap gap, which are also evident as vorticity jets and streaks in the instantaneous vorticity fields. The frequency and intensity of this jet vary with decreasing h/c.

4.5.4 Flap

Meanwhile, flow beneath the flap stagnation point separates as shear layer SL_{F2}, entering the wake and generating periodic upward swirling vortices downstream. These vortices influence the flap recirculation bubble (RB_F), pushing it upward, as observed in the u-velocity field.

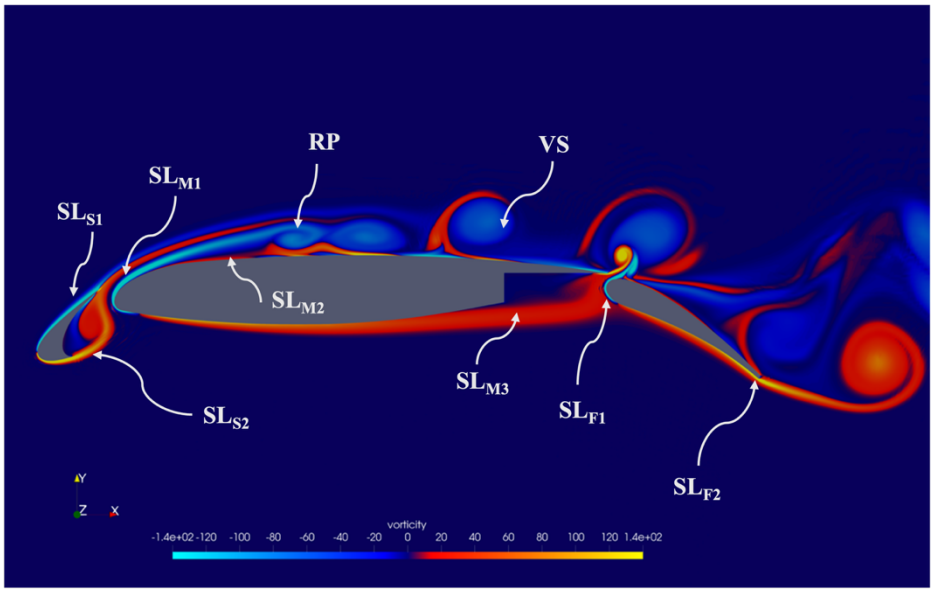

Figure 4:16: Instantaneous Vorticity Field for Ground Clearance Ratio h/c = 1

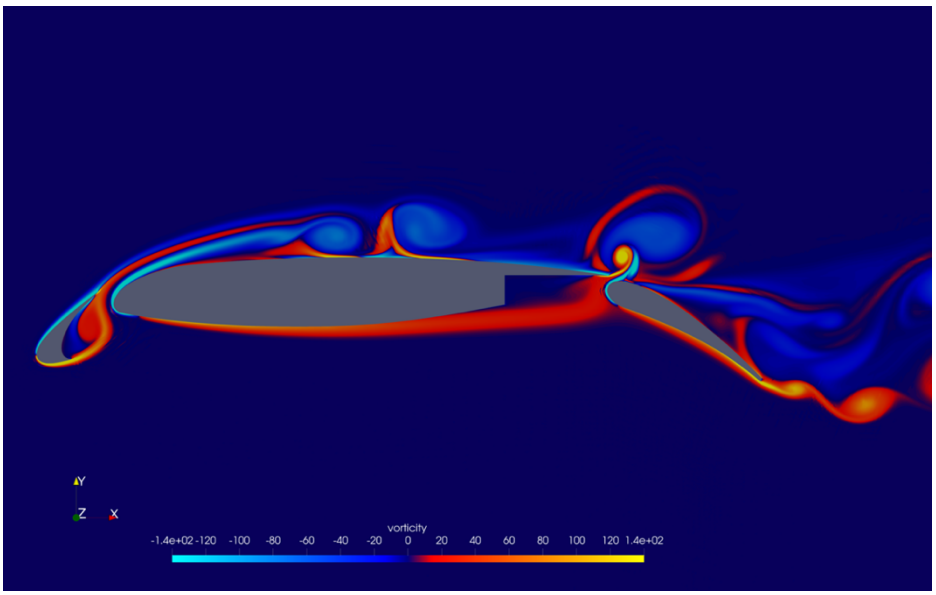

Figure 4:17: Instantaneous Vorticity Field for Ground Clearance Ratio h/c = 0.8

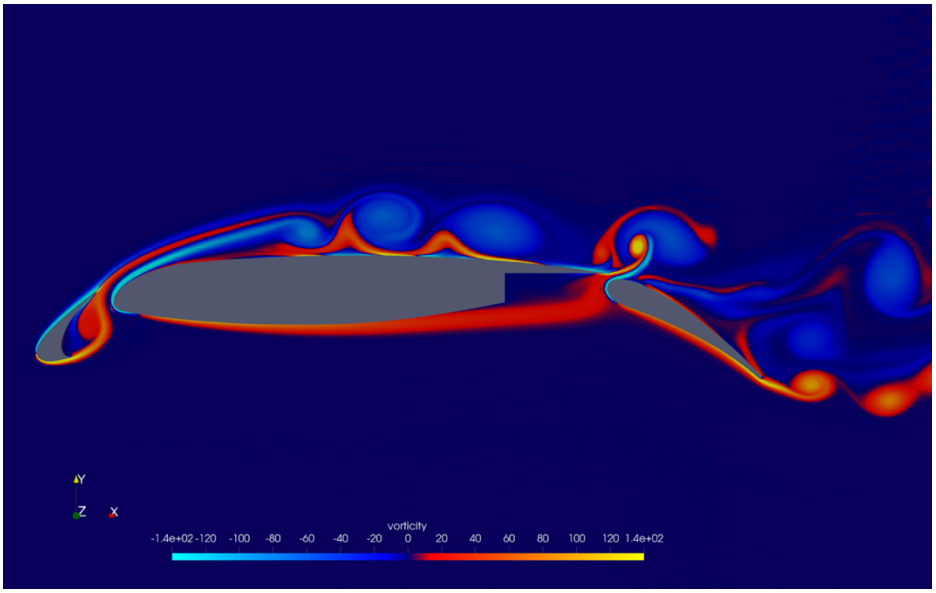

Figure 4:18: Instantaneous Vorticity Field for Ground Clearance Ratio h/c = 0.6

4.6 Time-Averaged Vorticity Field

In this section, the time-averaged vorticity fields are presented to complement and enhance the observations made in the instantaneous vorticity analysis. These averaged fields highlight the persistent shear layers, the regions of vortex shedding, and the reattachment zones. Additionally, the averaged fields reveal the formation and extent of the laminar and secondary separation bubbles over the slat, main element, and flap. Figures 4.19 - 4.21 illustrate these time-averaged vorticity distributions for the three h/c ratios 1, 0.8, and 0.6, respectively, facilitating a comparative assessment of how the ground clearance influences the mean flow topology. The labels used in the discussion are commonly presented in previous section Figure 4.16, for reference.

4.6.1 Slat

The time-averaged vorticity fields clearly reaffirm the presence of the shear layers SL_{S1} and SL_{S2} separating from the slat, indicating that these structures persist even under averaging. Both shear layers extend over the main element, with this extent increasing as h/c decreases. This longer propagation contributes to the delayed roll-up observed in the instantaneous vorticity fields, consequently postponing the vortex shedding and the transition from laminar to turbulent flow.

4.6.2 Main

In ground-effect conditions, the shear layer SL_{M1} separates earlier than in the free-stream case [4], with separation progressively delayed as h/c decreases (detailed discussion in C_f section). An additional shear layer, SL_{M2}, is observed closer to the airfoil surface around x/c ≈ 0.4, which attaches back to the surface, downstream near x/c ≈ 0.5, forming the secondary separation bubble, SB_{M2}. Following the vortex shedding (VS) identified in the instantaneous vorticity fields, the averaged vorticity field clearly illustrates the reattachment regions of these shear layers over the main element. As h/c decreases, the reattachment points shift further downstream, resulting in a larger and thicker separation region. This enlarged separation bubble increases the local camber, potentially enhancing lift, in agreement with observations reported in the literature [2][4].

4.6.3 Main-Flap

In the time-averaged vorticity fields, the periodic vorticity jets observed in the instantaneous fields are smoothed into weaker, fading jet-like structures. Similarly, the periodic streaks originating from the combination of SL_{F1} and SL_{M3} are averaged out, appearing as persistent shear-layer streaks extending over the flap. These shear layers influence the flap recirculation bubble (RB_F), causing its upper boundary to incline downward, a feature consistent with the trends observed in the time-averaged u-velocity fields.

4.6.4 Flap

The shear layer separating from the lower surface of the flap (SL_{F2}), which generates periodic upward swirling vortices in the instantaneous vorticity fields, appears in the time-averaged fields as an upward diffused vorticity smear. This averaged signature explains why the lower boundary of the flap recirculation bubble (RB_F), which extends into the wake, is displaced upward, as also seen in the time-averaged u-velocity fields. The upward inclination of these vortical structures, evident in the instantaneous fields and reinforced in the averaged vorticity distribution, becomes more pronounced as h/c decreases. This effect is likely linked to ground proximity, where the upward deflection of the wake leads to a narrowing compared to the free-stream condition. Such wake narrowing can be associated with the reduction in pressure drag C_{D_p}, consistent with the lower $C_D$values discussed in the drag coefficient section.

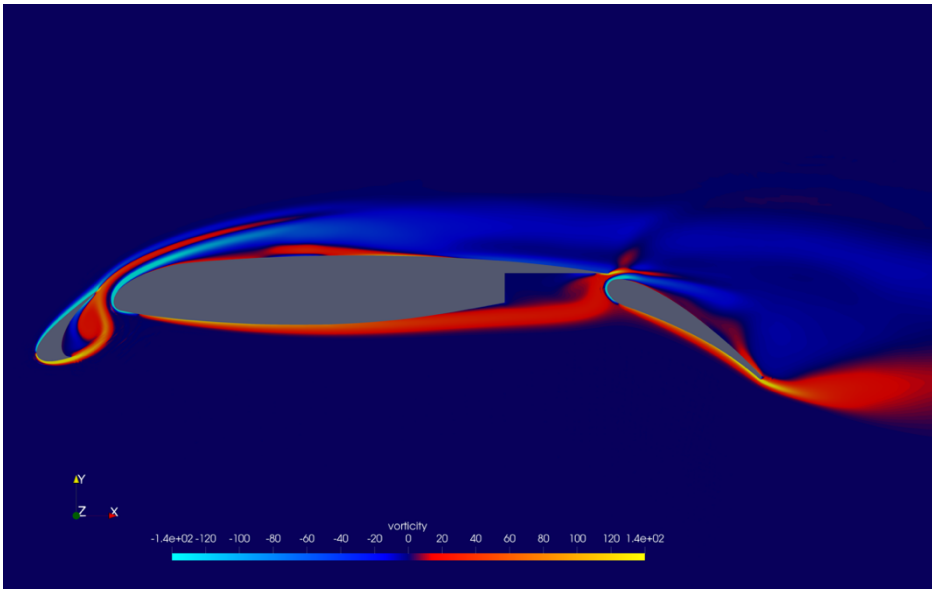

Figure 4:19: Time-Averaged Vorticity Field for Ground Clearance Ratio h/c = 1

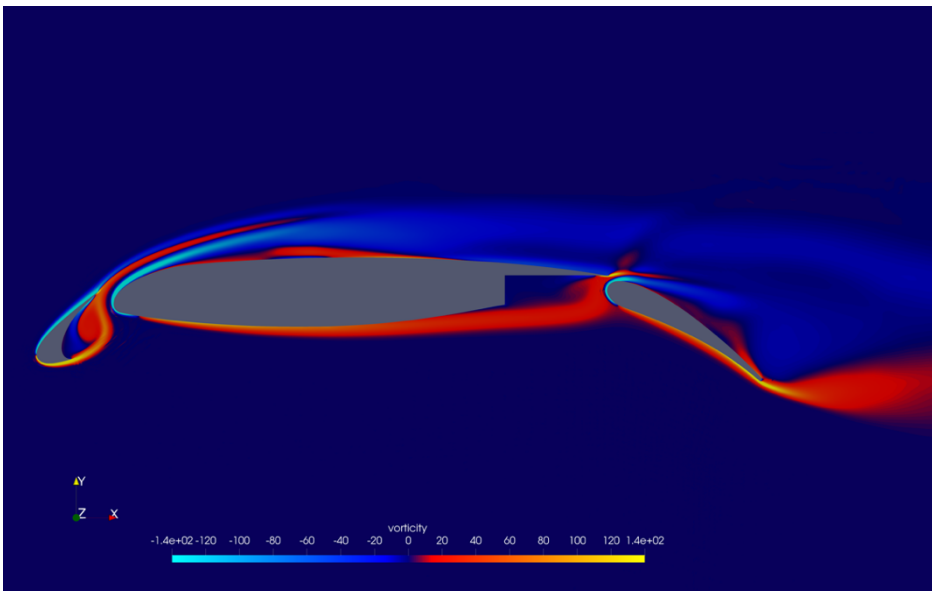

Figure 4:20: Time-Averaged Vorticity Field for Ground Clearance Ratio h/c = 0.8

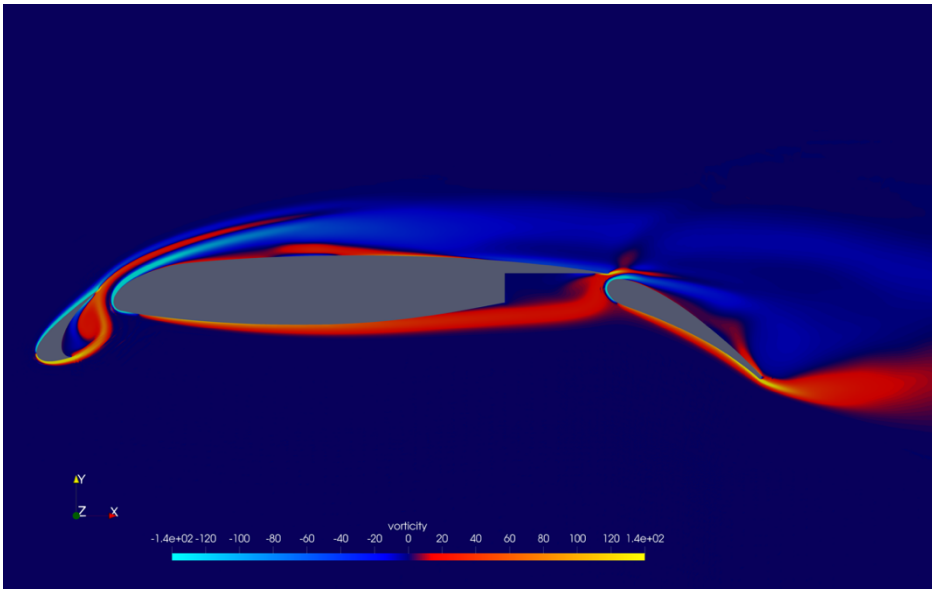

Figure 4:21: Time-Averaged Vorticity Field for Ground Clearance Ratio h/c = 0.6

4.7 Velocity Profiles

The streamwise mean velocity, expressed as u_s / U_e, are presented at seven chordwise locations over the 30P30N airfoil for the three ground clearance ratios, h/c = 1, 0.8 and 0.6. Here, U_e denotes the edge velocity at δ_{99}, and u_s is the local mean streamwise velocity, resolved in the streamwise-normal (s-n) coordinate system. One location, x/c = 0.05 was selected on the slat, four locations, x/c = 0.2, 0.4, 0.6 and 0.8 on the main element, and two locations, x/c = 1.0, 1.1, on the flap. The vertical axis is normalized by the stowed chord length (y_n/c). Figure 4.22 shows the locations of these seven profiles along the airfoil. Figure 4.23 presents the velocity profiles for all three h/c ratios, and these results are further compared against the free-stream reference profiles in Figure 4.24, highlighting both the effect of ground proximity and the relative changes among the three h/c cases.

The velocity profiles for all three h/c cases largely collapse onto each other across most chordwise locations, with noticeable differences observed at x/c = 0.6, 0.8, and 1.1. At x/c = 0.05 on the slat, the mean streamwise velocity, u_s , gradually increases with y/c and reaches the edge velocity U_e at y_n/c ≈ 0.01, corresponding to the 99% boundary layer thickness (δ_{99}). Above this height, u_s decreases slightly. This trend is consistent with the free-stream reference profile.

For x/c = 0.2, a small region of negative velocity is observed near the wall, indicating the presence of reverse flow associated with a recirculation bubble in this region. This suggests that flow separation is more pronounced compared to the free-stream condition (see Figure 4.24 (b)). Further away from the wall, between y/c = 0.02 and 0.035, a flow deviation is observed in the velocity profile is observed, attributed to the presence of shear layers (SL_{S1} and SL_{S2}) separating from the slat trailing edge. This deviation is more prominent than in the free-stream case, reflecting the stronger separated shear layers at this location.

At the chordwise position x/c = 0.4, near-wall measurements reveal a region of positive velocity immediately below a small zone of negative velocity, indicating the presence of the primary LSB and secondary separation bubble (SB_{M1} and SB_{M2}) over the main element. The observed near-wall positive velocity may also result from the SL_{M2} shear layer separating in this region, contributing to the formation of SB_{M2}. At a higher location, $y_n/c \approx 0.05$, a localized deviation in the velocity profile is evident due to the strong shear layers SL_{S1} and SL_{S2} separating from the slat. This confirms that these shear layers are convected further downstream, beyond roughly one-third of the chord, consistent with the trends discussed in the velocity and vorticity sections. In the free-stream case, the absence of these convected shear layers eliminates this local flow deviation, as seen in Figure 4.24 (c).

The velocity profile at x/c = 0.6 reveals a pronounced region of reverse flow near the wall, associated with the secondary separation bubble SB_{M2}. As the ground clearance decreases, the intensity of this reverse flow increases, indicating that the flow re-energization and transition are delayed, which is also evident from the free-stream velocity profile in Figure 4.24 (d). Additionally, the h/c = 1 case reaches U_e at a lower y/c than the h/c = 0.8 and 0.6 cases, suggesting that the thickness of the laminar separation bubble SB_{M1} is comparatively smaller for higher ground clearance and free-stream conditions. Around this chordwise location, the re-energized flow begins to approach reattachment, as the transition process restores sufficient momentum.

Velocity profiles at x/c = 0.8 exhibit no reverse flow, indicating that the boundary layer has fully reattached and is moving downstream. Similar to the behaviour observed at x/c = 0.6, the h/c = 1 case reaches U_e sooner than the lower ground clearance cases, suggesting that the reattached boundary layer becomes thicker as h/c decreases.

For x/c = 1.0, a slight reverse flow persists near the wall due to a separation bubble atop the flap. A localized positive velocity deviation occurs as a result of streaks ejected from the flap–main gap, before the streamwise velocity gradually approaches U_e. This deviation is smaller than in the free-stream condition, indicating that streak intensity plays a larger role in the free-stream case, whereas the slot jet is the dominant averaged phenomenon in the current study.

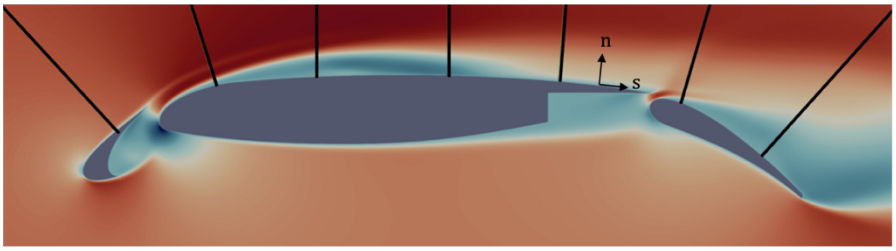

Figure 4:22: Location of Seven Chordwise Locations Over Which the Streamwise Mean Velocity Profile is Plotted

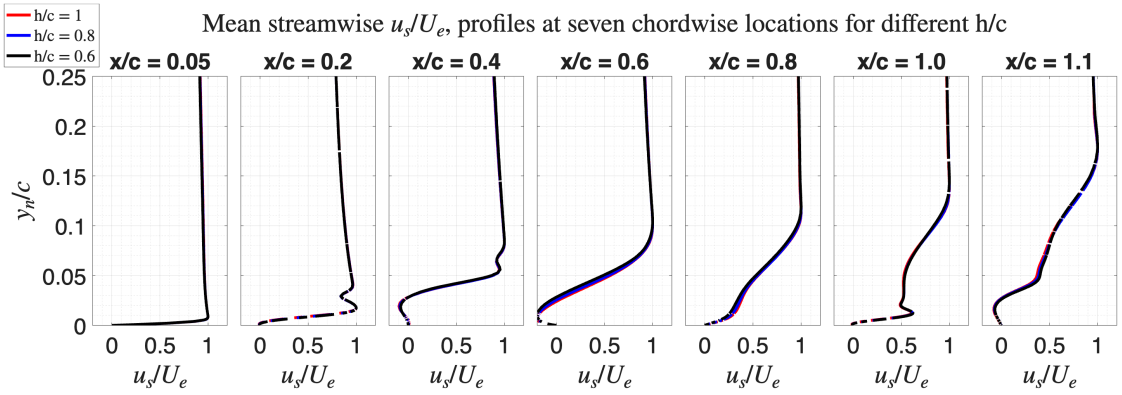

Figure 4:23: Streamwise Mean Velocity Profiles at Seven Chordwise Locations Over the 30P30N Airfoil (as noted in Figure 4.22) for Different Ground Clearance Ratio, h/c = 1, 0.8, and 0.6

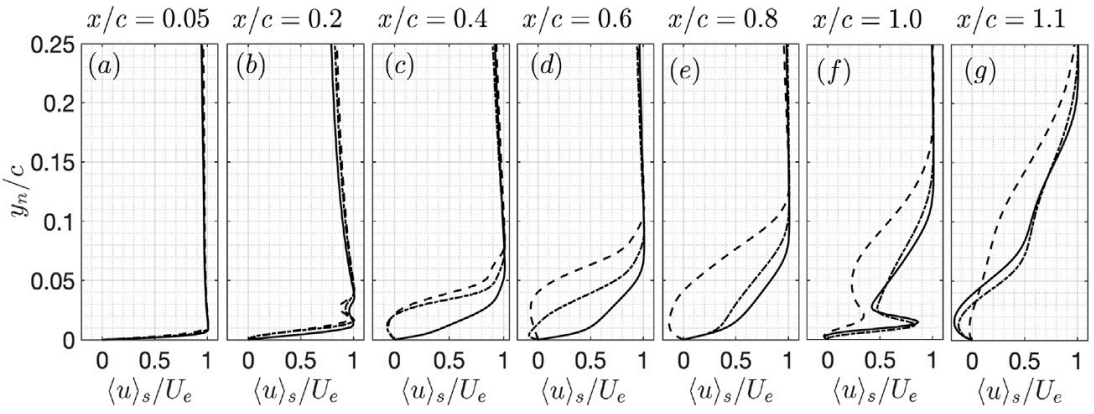

Figure 4:24: Streamwise Mean Velocity Profiles at Seven Chordwise Locations Over the 30P30N Airfoil in Freestream Condition [4]

Near-wall reverse flow is again observed for x/c = 1.1, due to the flap separation bubble. The velocity, however, reaches U_e earlier than in the free-stream case, implying that the flap separation bubble is comparatively narrower in the present configuration. Overall, the profiles demonstrate that reduced ground effect causes earlier flow separation while simultaneously delaying boundary layer transition and reattachment along the airfoil surface.

4.8 Aerodynamics Coefficients

4.8.1 Lift and Drag Coefficients

The lift and drag coefficients for the different ground clearance ratios h/c = 1, 0.8, and 0.6 are analyzed in this section. These results are also compared with free-stream studies [4] conducted for 3D configurations. Although not strictly one-to-one with the present 2D simulation, the comparison provides a useful reference and indicates that the observed trends are consistent with established data, thereby supporting the validity of the current analysis.

The lift, L, and drag, D, forces on the airfoil are calculated directly from the total force results obtained from the Nek5000 simulation. The calculations for their respective coefficients, C_L and C_D, are performed using Equations 4.1 and 4.2 as follows:

$$C_L = \frac{L}{\frac{1}{2}\,\rho\, {U_\infty}^2\, c},$$	(4.1)

$$C_D = \frac{D}{\frac{1}{2}\,\rho\, {U_\infty}^2\, c},$$	(4.2)

where D and L are the total lift and drag forces (sum of forces due to pressure and viscosity), and ρ is the density of the fluid and U_∞ is the freestream velocity, and c is the stowed chord length (c = 1).

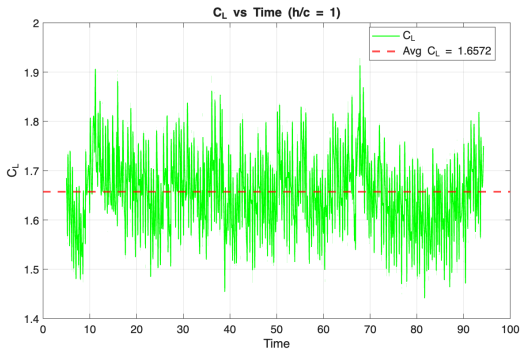

(a) Lift Coefficient

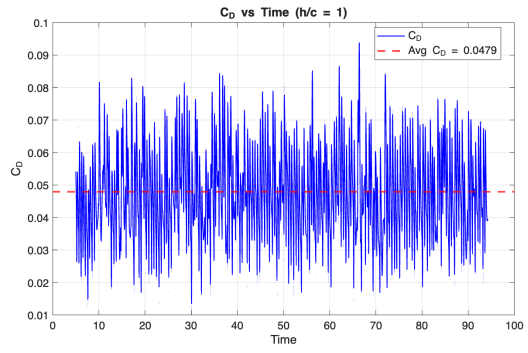

(b) Drag Coefficient

Figure 4:25: Aerodynamic Coefficients for Ground Clearance Ratio h/c = 1

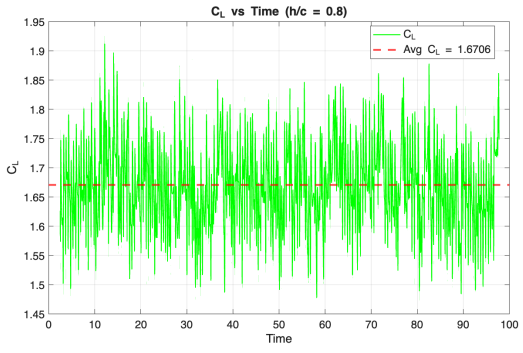

(a) Lift Coefficient

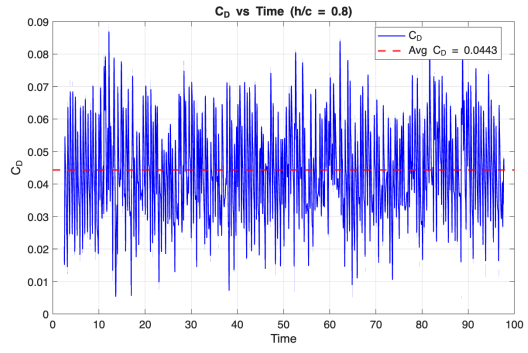

(b) Drag Coefficient

Figure 4:26: Aerodynamic Coefficients for Ground Clearance Ratio h/c = 0.8

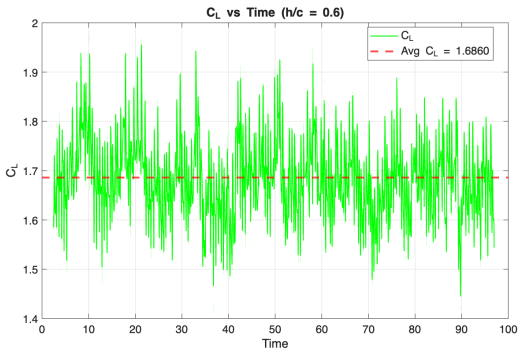

(a) Lift Coefficient

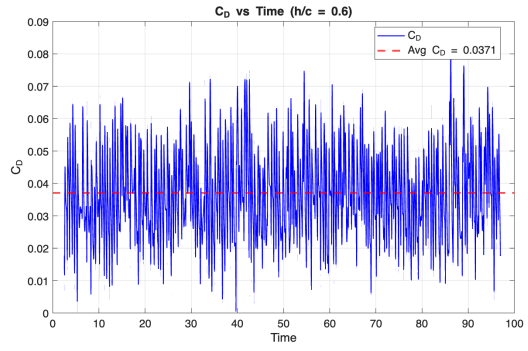

(b) Drag Coefficient

Figure 4:27: Aerodynamic Coefficients for Ground Clearance Ratio h/c = 0.6

Both the lift and drag coefficients are time-averaged over 10.5 flow-throughs for all three h/c ratios. Their temporal variations are presented in Figures 4.25 - 4.27, respectively, along with their corresponding mean values.

The C_L increases as the airfoil approaches the ground, with the h/c ratio decreasing from 1 to 0.6. The variation in C_L across the three h/c cases ranges between 0.8% to 1.74% (see Table 4.2). Meanwhile, the drag decreases by about 7.5% as h/c reduces from 1.0 to 0.8, and by approximately 16% as h/c further decreases from 0.8 to 0.6. This indicates a linear trend, where for every 0.2 reduction in h/c, the drag coefficient deviation percentage drops approximately by a factor of two. Correspondingly, the overall C_L/C_D ratio follows a similar pattern.

Table 4.2: Lift and Drag Coefficient Comparison for the Different Ground Clearance Ratios

h/c	C_L	C_L deviation (%)	C_D	C_D deviation (%)	C_L/C_D	C_L/C_D deviation (%)
1.0	1.6572	-	0.0479	-	**34.60**	**-**
0.8	1.6706	0.81	0.0443	7.52	**37.71**	**9.00**
0.6	1.6860	1.74	0.0371	22.55	**45.44**	**31.35**

The present study shows an increase in C_L of 6.3% – 8% compared to the free-stream condition, as summarized in Table 4.3. This enhancement is attributed to the increased pressure on the lower surface of the airfoil and the corresponding reduction in pressure on the upper surface, as discussed in the C_p section. In contrast, the ground effect leads to a significant reduction in drag, ranging from 17% to 35%. Consequently, the overall C_L/C_D ratio increases by 28% to 68 % relative to the freestream condition, representing more than a 1.7-fold improvement. This demonstrates that the ground effect significantly enhances aerodynamic performance, primarily due to the drag reduction and the cushioning effect of the ground.

Table 4.3: Lift and Drag Coefficient Comparison Between Freestream Condition and Different Ground Clearance Ratios

h/c	C_L	C_L deviation (%)	C_D	C_D deviation (%)	C_L/C_D	C_L/C_D deviation (%)
Freestream	1.559	-	0.0578	-	26.97	**-**
1.0	1.6572	6.30	0.0479	17.13	34.60	**28.27**
0.8	1.6706	7.16	0.0443	23.36	37.71	**39.81**
0.6	1.6860	8.15	0.0371	35.81	45.44	**68.49**

Table 4.4: Pressure Drag Comparison Between Freestream and Different Ground Clearance Ratios

h/c	C_D	C_{D_p} (%)	C_{D_p} deviation (%)	
			from h/c =1	from freestream
Freestream	0.0578	**71.7**	**-**	**-**
1.0	0.0479	**64.09**	**-**	**25.92**
0.8	0.0443	**61.40**	**11.40**	**34.37**
0.6	0.0371	**54.45**	**34.20**	**51.26**

Table 4.4 presents the comparison of pressure drag between the freestream condition and the present study. A reduction in pressure drag is observed as the airfoil moves closer to the ground, primarily due to the narrowing of the wake region. In the free-stream simulations reported by [4] the pressure drag coefficient (C_{D_p}) decreased from 71.7% to 64.9% as the Reynolds number increased from 1.27 x 10^4 to 1.83 x 10^4. In the present study, a comparable C_{D_p} of 64.1% is obtained at h/c = 1, suggesting that the ground effect may act to increase the local Reynolds number near the airfoil. This local Reynolds number enhancement could partially explain both the reduction in drag and the improvement in lift. Although the precise magnitude of this increase cannot be quantified from the current results, the presence of a smaller separation bubble in the slat cove region, as observed in the velocity and vorticity fields, provides further evidence supporting this interpretation.

4.8.2 Pressure Coefficient

This section presents the pressure coefficient distribution over the 30P30N multi-element airfoil for the different ground clearance ratios h/c = 1, 0.8 and 0.6. The variation of C_p along the chord highlights key aerodynamic features such as suction peaks, pressure recovery, and regions of adverse pressure gradient, which are directly associated with boundary-layer development, flow separation, and reattachment behaviour. Figure 4.28 - 4.30 presents the pressure coefficient, C_p, distribution over the 30P30N airfoil. For comparison, the results are evaluated against freestream condition [61] shown in Figure 4.31 to highlight the influence of ground effect.

From the pressure data obtained using Nek5000, the pressure coefficient (C_p) is computed according to Equation 4.3.

$$C_p = -\frac{p - p_\infty}{\frac{1}{2}\rho U_\infty^2},$$	(4.3)

where p is the local pressure, the p_∞ is stream pressure defined such that C_p = -1 at the stagnation point, ρ is the density of the fluid and U_∞ is the freestream velocity.

The overall trend of the pressure coefficient (C_p) profile remains consistent across different h/c ratios, with minor moderations over the main element and the slat. As h/c decreases from 1.0 to 0.6, a 25% reduction in the suction peak is observed on the upper trailing edge of the slat, accompanied by a progressive shift of the suction peak toward the trailing edge. This is shown in Figure 4.29. At the leading edge of the main element, the C_p profiles collapse over each other. The accelerating flow in this region causes a pressure drop, yielding a suction peak in C_p that decreases as the airfoil moves closer to the ground.

Subsequently, as the flow encounters an adverse pressure gradient (APG) around x/c = 0.16, it induces a laminar flow separation. This separation leads to a quasi-plateau region in the C_p profile, characteristic of minimal pressure change [4], and causes the previously collapsed profiles to diverge, showing a noticeable difference among the three different h/c ratios.

The C_p distribution exhibits a characteristic bump over the main element, as seen in Figures 4.28 and 4.29. This feature is attributed to the presence of a secondary separation bubble (SB_{M2}) located beneath the larger LSB, SB_{M1} in this region. The C_p bump initiates at approximately x/c ≈ 0.4, coinciding with the onset of the secondary separation bubble, SB_{M2}, and reaches a maximum peak at x/c ≈ 0.5 where the SB_{M2} terminates. Beyond this point, the flow transitions and gains sufficient momentum to overcome the APG and reattaches downstream. A slight downstream shift in the SB_{M2} is also observed as the ground clearance h/c decreases. On the flap, the C_p plateau extends to the trailing edge due to the absence of reattachment, similar to observations in Figure 4.31 [4].

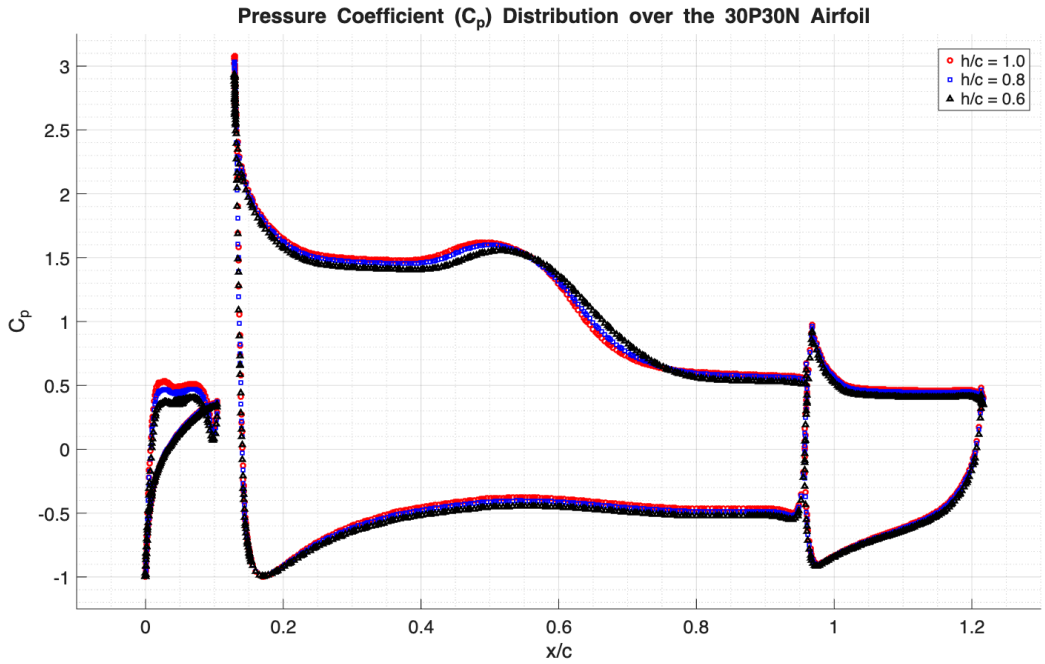

Figure 4:28: Pressure Coefficients, C_p, Distribution Over 30P30N Airfoil for Different Ground Clearance Ratio, h/c = 1, 0.8, and 0.6

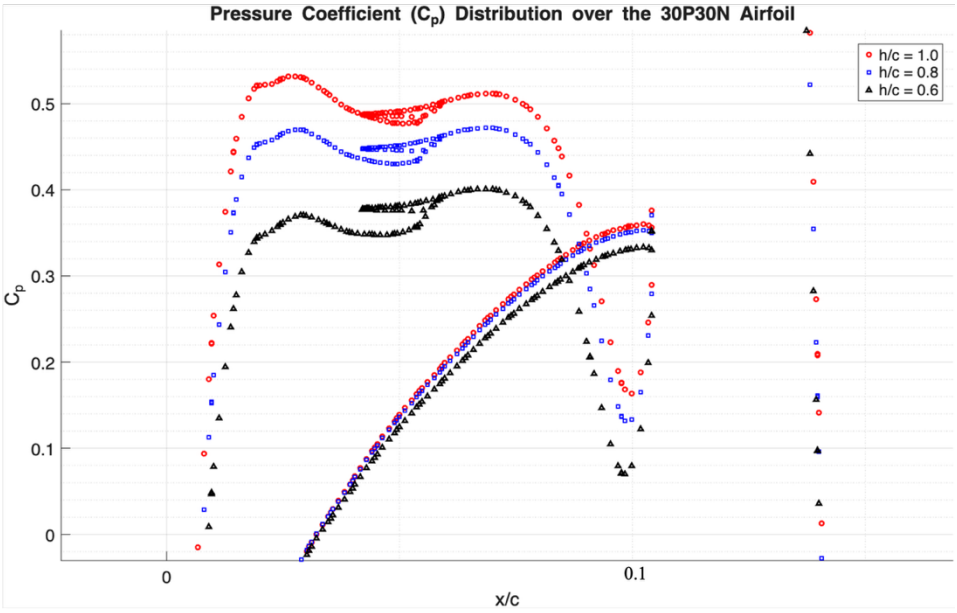

Figure 4:29: Pressure Coefficients Distribution Over the Slat Trailing Edge for Different Ground Clearance Ratio, h/c = 1, 0.8, and 0.6

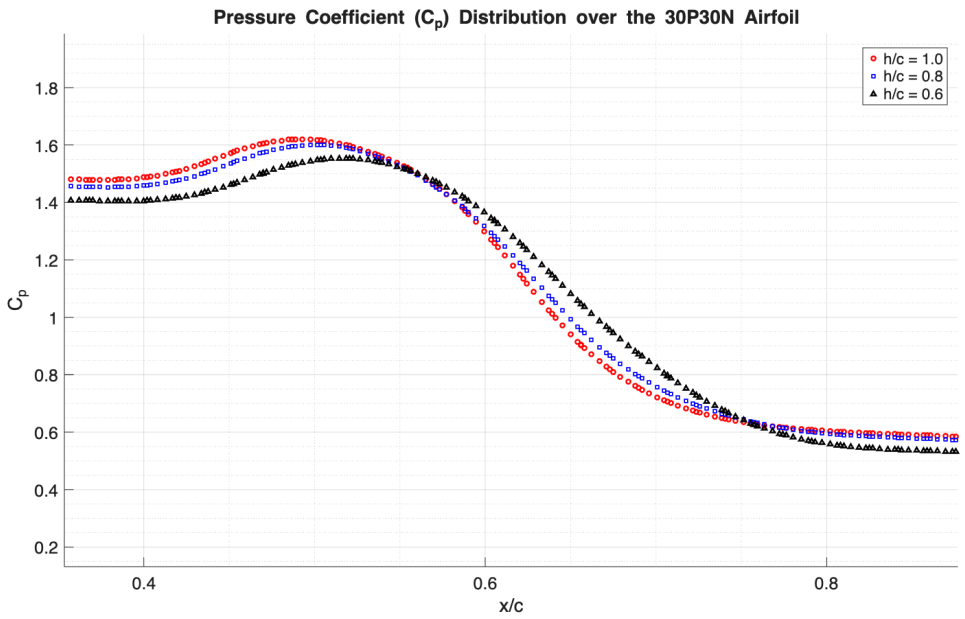

Figure 4:30: Pressure Coefficients Distribution Over the Main Element Showing C_p Bump for Different Ground Clearance Ratio, h/c = 1, 0.8, and 0.6

Although the overall trend in the C_p appears similar for the different h/c ratios, the effect of ground influence has altered the distribution of C_p over the main element and the slat of the airfoil compared to the freestream condition. Over the slat relative to the free-stream condition [4], the pressure on the upper surface of the airfoil increases by approximately 33% at h/c = 1 and by about 50% at h/c = 0.6.

These results indicate that, for the main element, the plateau and bump on the suction side produce a sustained low-pressure region, while the ground effect increases pressure on the pressure side. This combination enhances lift, as reflected in the C_L plots and summarized in Table 4.2.

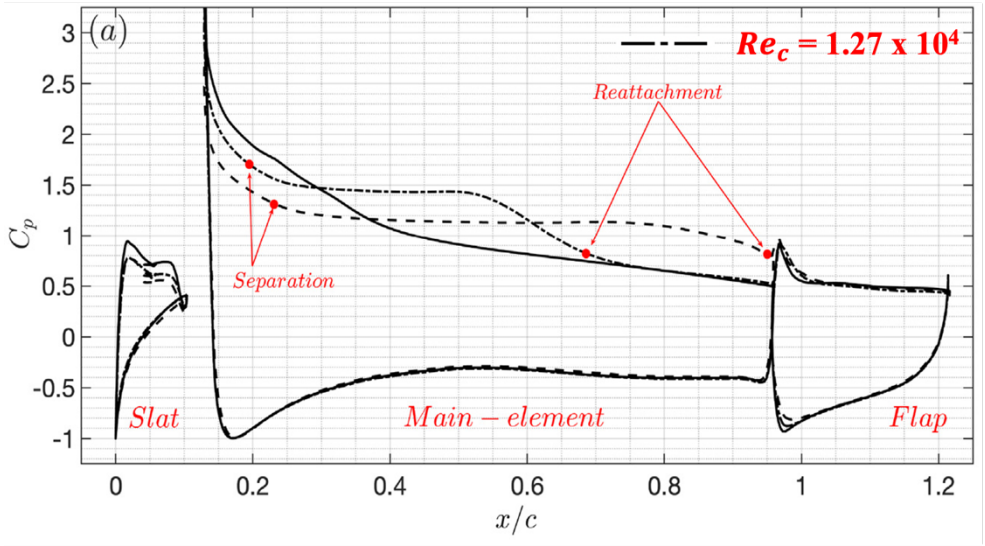

Figure 4:31: Pressure Coefficients Distribution Over 30P30N Airfoil in Freestream Condition [4]

4.8.3 Skin Friction Coefficient

To gain deeper insight into the near-wall flow characteristics, the skin friction coefficient (C_f) distribution is analyzed for different ground clearance ratios h/c = 1, 0.8 and 0.6. The C_f provides valuable information on the boundary layer behaviour, including the locations of flow separation, transition, and reattachment along the airfoil surface. This section examines the distributions to identify key flow features that affect aerodynamic performance, especially under ground proximity.

The skin friction coefficient is computed using Equation 4.4, where the wall shear stress is directly obtained from Nek5000.

$$C_f = \frac{\tau_w}{\frac{1}{2}\rho U_\infty^2},$$	(4.4)

where τ_w is the wall shear stress, ρ is the density of the fluid and U_∞ is the freestream velocity.

The skin friction coefficient distribution over a specific range of x/c on the main element is presented in Figure 4.32. For comparison, the results are evaluated against those of the

freestream condition [4] shown in Figure 4.33 to highlight the influence of ground effect. The corresponding flow separation and reattachment points are also summarized in Tables 4.5 and 4.6 for clarity.

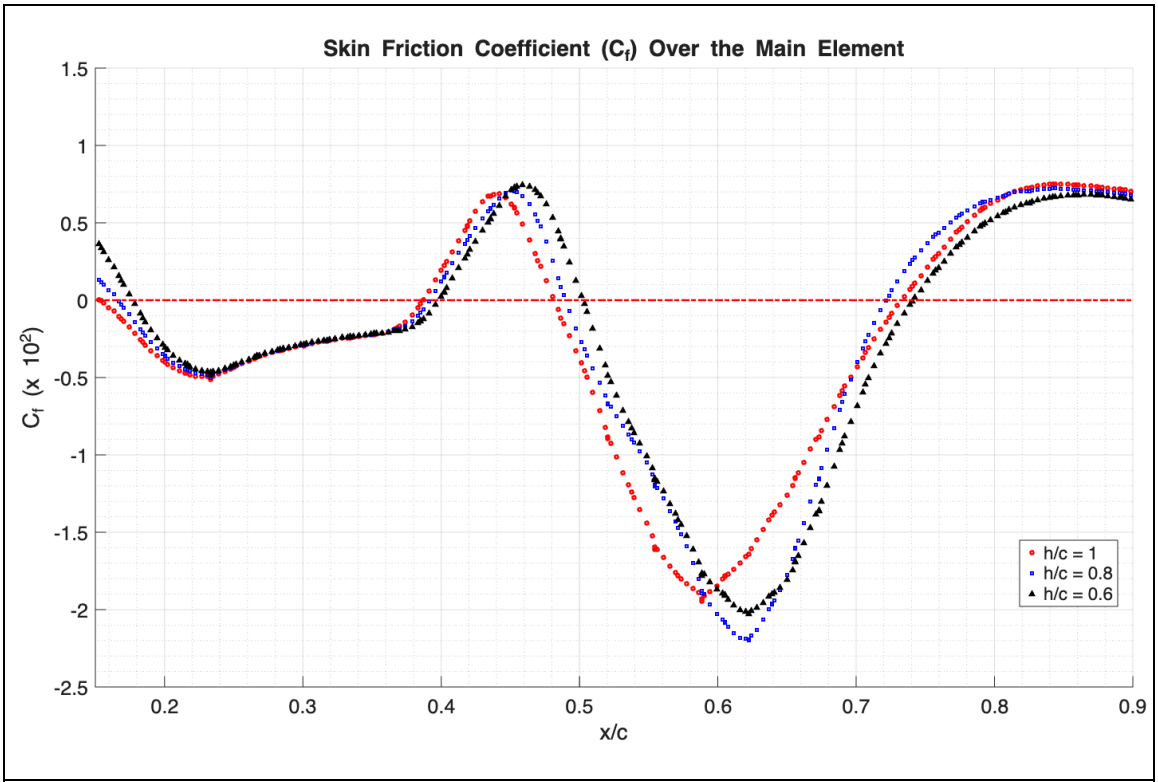

Figure 4:32: Variation of Skin-Friction Coefficient Over the Main Element for Different Ground Clearance Ratios, h/c = 1, 0.8 and 0.6

Typically, a positive skin friction coefficient (C_f) corresponds to attached flow along the airfoil surface, while a negative C_f indicates flow reversal associated with boundary-layer separation. The location where C_f changes from positive to negative, marks the onset of flow separation, whereas the point where it transitions from negative back to positive indicates flow reattachment.

From Figure 4.32 and Table 4.5, it is evident that the main flow separation behaviour varies with different ground clearance ratios. At the start of the graph, the gradual decline of C_f, crossing from positive to negative, indicates flow separation, caused by the boundary layer encountering an adverse pressure gradient that promotes detachment from the airfoil surface. For h/c = 1, separation occurs early at approximately x/c = 0.15; for h/c = 0.8 it is delayed to x/c = 0.17 and for h/c = 0.6, separation occurs around x/c = 0.18. Thus, as the ground clearance decreases, flow separation is progressively delayed. One possible explanation for the delayed separation is that decreasing ground clearance marginally

increases the local Reynolds number in the main flow through the slat-main gap, which energizes the boundary layer and allows it to withstand the adverse pressure gradient for a longer distance.

Comparing these results with the separation location under freestream condition [4] shown in the pressure coefficient distribution section (Figure 4.31), we see that separation in the freestream condition occurs around x/c = 0.2, which is slightly downstream of the ground-effect cases. Overall, in all three cases, the ground proximity tends to slightly promote separation compared to the freestream condition. However, our results show that reducing the ground clearance delays flow separation. The magnitude of this delay is small and can be considered within the typical approximation for flow separation estimation.

Table 4.5: Main Flow Separation and Reattachment Points for the Freestream Condition and Different Ground Clearance Cases

h/c	Main-Flow Separation Point (x/c)	Main-Flow Reattachment Point (x/c)
Freestream	0.2	0.69
1.0	0.152	0.732
0.8	0.167	0.721
0.6	0.177	0.741

For all three ground clearance cases, around x/c = 0.24 a gradual, plateau-like increase in the skin friction coefficient (C_f) is observed. This is followed by a sharp rise in C_f, which crosses the zero line at approximately x/c = 0.39, becoming positive and indicating a local reattachment. After this reattachment, C_f remains temporarily positive before dropping back to negative, reflecting a local separation feature, thereby forming a small positive C_f bump.

It is important to note that this temporary positive C_f bump occurs approximately at the same location on the main element where the secondary separation bubble, SB_{M2} originates and eventually dissipates, as discussed in the previous sections. To reiterate, SB_{M2} was identified by the streamlines analysis in the time-averaged u-velocity field section, and its formation was attributed to roll-ups and wave-like flow features, as highlighted in the instantaneous vorticity and velocity results. Therefore, this brief positive C_f bump can be attributed to a local reattachment followed by subsequent separation within the SB_{M2} recirculation region, reflecting the complex near-wall flow dynamics in this area. This behaviour is not observed in the freestream case (see Figure 4.33) due to the absence of a secondary separation bubble, SB_{M2}. The locations of the local reattachment and separation points are summarized in Table 4.6. It is also noted that the local reattachment and

separation points associated with SB_{M2} shift downstream as h/c decreases, as discussed in the previous sections.

Table 4.6: Local Reattachment and Separation and Points Due to SB_{M2} for Different Ground Clearance Cases

h/c	Local Reattachment Point (x/c) due to SB_{M2}	Local Separation Point (x/c) due to SB_{M2}
1.0	0.387	0.482
0.8	0.391	0.490
0.6	0.397	0.502

Following the temporary C_f bump, the skin friction coefficient drops to a deep negative valley, indicating the separation region, as observed in the freestream condition shown in Figure 4.28. Among the ground clearance cases, h/c = 0.8 exhibits the most negative C_f, indicating the strongest flow reversal. When compared to the freestream case, the present ground effect simulations show a more pronounced negative C_f, demonstrating that ground proximity amplifies the intensity of flow reversal.

Further reattachment of the main flow along the main element observed in Figure 4.32 and summarized in Table 4.5, occurs after x/c = 0.7, for all three ground clearance cases. Around x/c ≈ 0.59, a sudden rise in the skin friction coefficient (C_f) is observed, indicating the onset of laminar-to-turbulent transition which also corresponds closely to the region where the pressure coefficient (C_p) begins to decline, as discussed in the pressure distribution section. This trend is consistent with the transition onset and pressure decline location discussed and reported in the freestream study [4]. As C_f continues to rise and crosses the zero line, the reattachment point of the boundary layer is identified.

For h/c = 1 the reattachment occurs at approximately x/c = 0.73; for h/c = 0.8, it shifts upstream to x/c = 0.72 and for h/c = 0.6 it moves downstream to x/c = 0.74. These results indicate that the main flow reattachment location does not vary monotonically with decreasing ground clearance. The apparent discrepancy for h/c = 0.8, which exhibits the earliest reattachment despite the strongest flow reversal among the ground clearance ratios, requires further analysis. One possible explanation is that this simulation case was run on a different computational cluster compared to the h/c = 1 and 0.6 cases, which may have introduced a small numerical inconsistency.

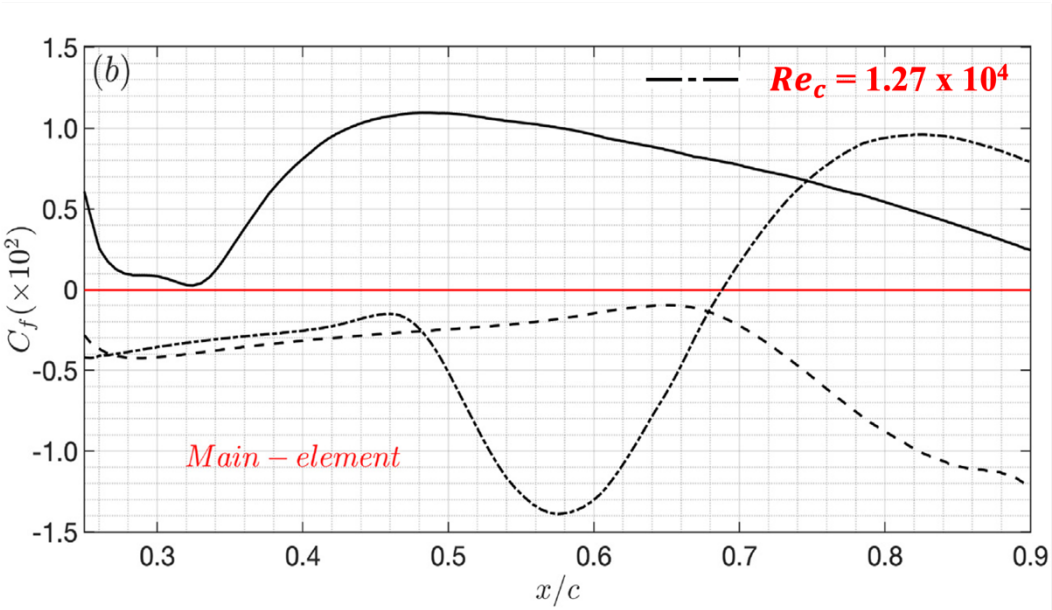

Figure 4:33: Variation of Skin-Friction Coefficient Over the Main Element for Freestream Condition [4]

These results, compared with the reattachment point under freestream conditions [4] shown in Figure 4.33 (and in Figure 4.31), indicate that reattachment in the freestream case occurs around x/c = 0.69, slightly upstream of the ground-effect cases. This confirms that the ground effect delays the reattachment point, as discussed in the previous sections. Shortly after reattachment, C_f rises rapidly and reaches a peak value, indicating the further strengthening of the turbulent flow. The overall trend of transition and peak C_f is similar across all three ground clearance ratios.

Chapter 5

Conclusion

The present study has investigated the intricate flow features around the 30P30N three-element airfoil in ground proximity using the spectral element DNS solver Nek5000. Simulations were performed at a low Reynolds number of $Re_c = 1.27 \times 10^4$ and a fixed angle of attack AoA, $\alpha = 4°$ for three ground clearance ratios h/c = 1, 0.8, and 0.6. The results were systematically compared with freestream cases reported in the literature [2-5], showing good overall agreement and validating the present approach.

For all three ground clearance cases considered in this study, the overall flow features remain broadly similar, with minor variations observed in the slat cove region, over the main element of the airfoil, and within the wake.

As the main flow moves past the 30P30N airfoil, a shear layer separates from the lower surface of the slat, is deflected by the main flow, and meanders in the slat cove region. This shear layer undergoes laminar reattachment near the slat trailing edge, giving rise to two separation bubbles within the slat cove. The primary, larger bubble decreases in size as ground clearance decreases and is also smaller than that observed under freestream conditions [4]. The reduction in bubble size reduces the extent of shear-layer meandering within the slat cove, thereby promoting earlier reattachment. Interestingly, in previous studies [2–8], a comparable decrease in the size of the primary bubble was reported only with increasing Reynolds number, suggesting that the local Reynolds number within the slat cove may have increased under ground-effect conditions.

The reattached shear layer separates again through the slat-main gap, merging with the shear layer originating from the slat's upper surface and subsequently convecting over the main element. As the ground clearance decreases, the shear layer convects farther downstream, indicating an increase in the local flow velocity within the gap.

The main flow over the leading edge of the main element accelerates rapidly before separating under the influence of the adverse pressure gradient (APG). The separated shear layer interacts with the slat shear layer, leading to wave-like roll-ups driven by Kelvin-Helmholtz (KH) instability. As h/c decreases, the onset of these roll-ups shifts downstream, indicating a delayed transition. The roll-ups eventually break down into discrete shedding vortices, which promote reattachment of the flow on the main element and give rise to a large laminar separation bubble. With decreasing ground clearance, the shear layer over

the main element shifts away from the wall, resulting in an increase in both the thickness and length of the separation bubble. This behavior reflects the longer distance required for the flow to recover sufficient momentum to overcome the adverse pressure gradient (APG). Furthermore, a secondary separation bubble develops beneath the primary bubble and shifts slightly downstream as h/c decreases. This secondary bubble is a distinct feature of ground-effect conditions and was not observed in the freestream case [2-9].

The shed vortices create a region of low-velocity flow that is convected downstream across the main-flap gap. As this low-velocity region passes over the gap, a periodic slot jet is generated into the main-flap cavity. This slot jet is attributed to the high-momentum flow from beneath the airfoil being forced into the gap as the low-velocity region moves past. The observed frequency of this jet ranges between 15-19 flow-through times for the different ground clearances considered in this study. Without the low-velocity clouds, the high-momentum flow from beneath the airfoil enters the main-flap gap smoothly, forming a continuous streak instead of a jet. This slot jet and streak of flow influence the flap recirculation bubble, causing its upper boundary to incline downward.

The flow separates over the flap, forming a large recirculation bubble on the flap and a coherent wake downstream. While the overall wake structure remains similar across the different ground clearance ratios, the wake becomes slightly narrower as the ground clearance decreases and is also narrower compared to the free-stream case. This narrowing is associated with the shear layer separating from the lower surface of the flap, which generates periodic upward-swirling vortices. These vortices displace the lower boundary of the flap recirculation bubble upward, further contributing to the observed narrowing of the wake.

These flow features are further validated by plotting the streamwise mean velocity at seven chordwise locations over the airfoil. In addition, aerodynamic metrics such as lift, drag, pressure coefficient, and skin-friction coefficient were analyzed, providing a comprehensive understanding of how these flow structures influence the overall aerodynamic efficiency of the airfoil.

It was observed that as the ground clearance decreased, the lift coefficient increased by approximately 2%, while the drag coefficient decreased significantly by 22.5%, resulting in an increase in the lift-to-drag ratio of about 31%. When compared with the free-stream condition [4], the lift-to-drag ratio was found to be substantially enhanced, showing an increase ranging from 28% to 68%. Furthermore, the narrowing of the wake at lower ground clearances led to a significant reduction in pressure drag, decreasing by 25% to 50% relative to the free-stream case.

The overall trend of the pressure coefficient distribution over the 30P30N airfoil remains consistent across the different ground clearance ratios. However, on the slat's suction surface, the pressure coefficient distribution exhibits a reduction of nearly 25% in the suction peak, accompanied by a shift of the peak towards the upper trailing edge as the ground clearance decreases. Over the main element, a distinct pressure bump appears due to the formation of a secondary separation bubble. This feature slightly increases the pressure coefficient following the quasi-static pressure plateau region. The presence of this bubble contributes to a locally lower pressure on the suction side, while the ground effect simultaneously enhances pressure on the lower surface. Together, these effects lead to an overall increase in lift compared to the free-stream condition.

A similar bump was observed in the skin-friction coefficient, caused by local reattachment followed by subsequent separation within the secondary recirculation bubble. The skin-friction results further indicate that flow separation is progressively delayed as the ground clearance is reduced. Interestingly, the reattachment location of the main flow does not vary monotonically with decreasing ground clearance. In particular, for the intermediate case of ground clearance ratio h/c = 0.8 the earliest reattachment was observed compared to the other ground-clearance ratios. This apparent discrepancy suggests that further analysis is required to better understand the underlying mechanisms.

Chapter 6

Future Work

The present study has provided detailed insights into the major two-dimensional flow features of the 30P30N configuration in ground effect. However, several important aspects remain open for further exploration, and the results obtained here can serve as a foundation for these investigations.

A natural extension of the current work would be the transition from two-dimensional to three-dimensional simulations. Previous studies [2-5] have demonstrated that Görtler-type vortices play a critical role at low Reynolds numbers, driving instability mechanisms and influencing transition. Capturing the origin, growth, and nonlinear evolution of these vortices in a three-dimensional setting would provide a more realistic representation of the flow physics associated with ground effect.

Another avenue for future research involves a detailed characterization of the roll-up structures forming over the main element. The variation in frequency and intensity of these roll-ups is closely linked to shear-layer instabilities that ultimately govern transition. Advanced modal decomposition techniques such as Proper Orthogonal Decomposition (POD), Dynamic Mode Decomposition (DMD), or Spectral POD could be applied to systematically extract the dominant flow modes and their temporal evolution. Such analyses would help establish a more direct connection between coherent structures, instability mechanisms, and unsteady aerodynamic loading.

Additionally, the effect of varying the angle of attack should be systematically examined. Since ground effect aerodynamics are highly relevant for take-off and landing conditions, analyzing how the flow topology, lift enhancement, and unsteady separation evolve with changing incidence would provide valuable insight into the operational performance envelope of the configuration.

References

[1] Fischer, P. F., Lottes, J. W., & Kerkemeier, S. G. (2008). NEK5000 web page. Retrieved from http://nek5000.mcs.anl.gov.

[2] Vadsola, M., Mavriplis, C., Agbaglah, G. G., & University of Ottawa. Department of Mechanical Engineering. (2020). High-Order Spectral Element Method Simulation of Flow Past a 30P30N Three-Element High Lift Wing. Université d'Ottawa / University of Ottawa.

[3] Vadsola, M., Agbaglah, G. G., & Mavriplis, C. (2021). Slat cove dynamics of low Reynolds number flow past a 30P30N high lift configuration. Physics of Fluids, 33(3). https://doi.org/10.1063/5.0036088.

[4] Teng, M. (2025). Transition to turbulence of an incompressible flow past a multi-element airfoil: Mean-flow dynamics. International Journal of Heat and Fluid Flow, 115, 109825. https://doi.org/10.1016/j.ijheatfluidflow.2025.109825.

[5] Wang, J.-S., Feng, L.-H., Wang, J., & Li, T. (2018). Görtler vortices in low-Reynolds-number flow over multi-element airfoil. Journal of Fluid Mechanics, 835, 898–935. https://doi.org/10.1017/jfm.2017.781.

[6] Wang, J., Wang, J., & Kim, K. C. (2018). Wake/shear layer interaction for low-Reynolds-number flow over multi-element airfoil. Experiments in Fluids, 60(1). https://doi.org/10.1007/s00348-018-2662-5.

[7] Wang, J.-S., & Wang, J.-J. (2021). Wake-induced transition in the low-Reynolds-number flow over a multi-element airfoil. Journal of Fluid Mechanics, 915, A28.

[8] Wang, J., & Wang, J. (2021). Vortex dynamics for flow around the slat cove at low Reynolds numbers. Journal of Fluid Mechanics, 919, A8. https://doi.org/10.1017/jfm.2021.385.

[9] Kokash, H., Mavriplis, C., & Agbaglah, G. G. (2024). On the origin of Görtler vortices in flow over a multi-element airfoil. Journal of Experimental and Theoretical Analyses, 2(4), 121–133. https://doi.org/10.3390/jeta2040010.

[10] Klausmeyer, S., & Lin, J. (1994). An experimental investigation of skin friction on a multi-element airfoil. In 14th Applied Aerodynamics Conference. https://doi.org/10.2514/6.1994-1870.

[11] Holloran, M., & O'Meara, S. (1999). Wing-in-ground effect craft review. DSTO Aeronautical and Maritime Research Laboratory. https://apps.dtic.mil/sti/pdfs/ADA361836.pd.

[12] Leishman, J. G. (2022). Ground effect vehicles. In Introduction to Aerospace Flight Vehicles. Embry-Riddle Aeronautical University. https://eaglepubs.erau.edu/introductiontoaerospaceflightvehicles/chapter/hovercraft/.

[13] Pua'at, A., Zhahir, A., Ahmad, M. T., & Hassan, A. (2024). Review on the Development of Wing-In-Ground Crafts. E3S Web of Conferences, 477, 00010. https://doi.org/10.1051/e3sconf/202447700010.

[14] Stack Exchange contributors. (2021). Ground effect and lift coefficient. Aviation Stack Exchange. https://aviation.stackexchange.com/questions/88290/ground-effect-and-lift-coefficient.

[15] Chin, V. D., Peters, D. W., Spaid, F. W., & McGhee, R. J. (1993). Flowfield measurements about a multi-element airfoil at high Reynolds numbers. AIAA Paper 93-3137. AIAA 24th Fluid Dynamics Conference, Orlando, FL.

[16] Bodart, J., Larsson, J., & Moin, P. (2013). Large eddy simulation of high-lift devices. In 21st AIAA Computational Fluid Dynamics Conference. https://doi.org/10.2514/6.2013-2724.

[17] Smith, A. M. O. (1975). High-lift aerodynamics. Journal of Aircraft, 12(6), 501–530. https://doi.org/10.2514/3.59830.

[18] Deck, S., & Laraufie, R. (2013). Numerical investigation of the flow dynamics past a three-element aerofoil. Journal of Fluid Mechanics, 732, 401–444. https://doi.org/10.1017/jfm.2013.363.

[19] Rogers, S., Menter, F., Durbin, P., & Mansour, N. (1994). A comparison of turbulence models in computing multi-element airfoil flows. In 32nd Aerospace Sciences Meeting and Exhibit. https://doi.org/10.2514/6.1994-291.

[20] Lynch, F., Potter, R., & Spaid, F. (1996). Requirements for effective high lift CFD. In 20th ICAS Congress (pp. 1479–1482).

[21] Klausmeyer, S. M., & Lin, J. C. (1997). Comparative results from a CFD challenge over a 2D three-element high-lift airfoil. NASA Technical Memorandum 112858.

[22] Anderson, W. K., Bonhaus, D. L., McGhee, R. J., & Walker, B. S. (1995). Navier-Stokes computations and experimental comparisons for multielement airfoil configurations. Journal of Aircraft, 32(6), 1246–1253. https://doi.org/10.2514/3.4687.

[23] Thomas, J. L., & Salas, M. (1986). Far-field boundary conditions for transonic lifting solutions to the Euler equations. AIAA Journal, 24(7), 1074–1080.

[24] Zhang, Y., Chen, H., Wang, K., & Wang, M. (2017). Aeroacoustic prediction of a multi-element airfoil using wall-modeled large-eddy simulation. AIAA Journal, 55(12), 4219–4233. https://doi.org/10.2514/1.J055853.

[25] Jawahar, H. K., Ali, S. A. S., Azarpeyvand, M., & Da Silva, C. R. I. (2020). Aerodynamic and aeroacoustic performance of high-lift airfoil fitted with slat cove fillers. Journal of Sound and Vibration, 479, 115347. https://doi.org/10.1016/j.jsv.2020.115347.

[26] Aly, H. S., Saqr, K. M., Eldrainy, Y. A., & Jaafar, M. N. (2009). Can large eddy simulation (LES) predict laminar to turbulent flow transition? International Journal of Mechanical and Materials Engineering, 4(1), 42–48. https://www.researchgate.net/publication/252066992_Can_large_eddy_simulation_LES_predict_laminar_to_turbulent_flow_transition.

[27] Kim, M., Lim, J., Kim, S., Jee, S., Park, J., & Park, D. (2018). Turbulent transition prediction using large-eddy simulation with the stability theory. Tech. Rep. ICCFD10-2018-0175. https://www.iccfd.org/iccfd10/papers/ICCFD10-175-Paper.pdf.

[28] Boutilier, M. S. H., & Yarusevych, S. (2012). Separated shear layer transition over an airfoil at a low Reynolds number. Physics of Fluids, 24(8). https://doi.org/10.1063/1.4744989.

[29] Mueller, T. J., & DeLaurier, J. D. (2003). Aerodynamics of small vehicles. Annual Review of Fluid Mechanics, 35(1), 89–111. https://doi.org/10.1146/annurev.fluid.35.101101.161102.

[30] Gaster, M. (1967). The structure and behaviour of laminar separation bubbles. Reports and Memoranda No. 3595, Aeronautical Research Council, London, England.

[31] Marxen, O., & Henningson, D. S. (2011). The effect of small-amplitude convective disturbances on the size and bursting of a laminar separation bubble. Journal of Fluid Mechanics, 671, 1–33. https://doi.org/10.1017/s0022112010004957.

[32] Hain, R., Kähler, C. J., & Radespiel, R. (2009). Dynamics of laminar separation bubbles at low-Reynolds-number aerofoils. Journal of Fluid Mechanics, 630, 129–153. https://doi.org/10.1017/s0022112009006661

[33] Jones, L. E., Sandberg, R. D., & Sandham, N. D. (2008). Direct numerical simulations of forced and unforced separation bubbles on an airfoil at incidence. Journal of Fluid Mechanics, 602, 175–207. https://doi.org/10.1017/s0022112008000864.

[34] Alam, M., & Sandham, N. D. (2000). Direct numerical simulation of 'short' laminar separation bubbles with turbulent reattachment. Journal of Fluid Mechanics, 410, 1–28. https://doi.org/10.1017/s0022112099008976.

[35] Carter, A. W. (1961). Effect of ground proximity on the aerodynamic characteristics of aspect-ratio-1 airfoils with and without end plates. NASA Technical Report L-1693. https://ntrs.nasa.gov/api/citations/19980228064/downloads/19980228064.pdf

[36] Ahmed, M. R., Takasaki, T., & Kohama, Y. (2006). Aerodynamics of a NACA4412 airfoil in ground effect. AIAA Journal, 45(1), 37–47. https://doi.org/10.2514/1.23872.

[37] Jamei, S., Maimun, A., Mansor, S., Azwadi, N., & Priyanto, A. (2012). Numerical investigation on aerodynamic characteristics of a compound wing-in-ground effect. Journal of Aircraft, 49(5), 1297–1305. https://doi.org/10.2514/1.c031627.

[38] Mahon, S., & Zhang, X. (2004). Computational analysis of pressure and wake characteristics of an aerofoil in ground effect. Journal of Fluids Engineering, 127(2), 290–298. https://doi.org/10.1115/1.1891152

[39] Qin, X., Liu, P., & Qu, Q. (2009). Aerodynamics of a multi-element airfoil near ground. Tsinghua Science & Technology, 14(S2), 94–99. https://doi.org/10.1016/s1007-0214(10)70039-0.

[40] Sereez, M., & Zaffar, U. (2021). Dynamic stall on high-lift airfoil 30P30N in ground proximity. Open Journal of Fluid Dynamics, 11(3), 135–152. https://doi.org/10.4236/ojfd.2021.113008.

[41] Sereez, M., Abramov, N., & Goman, M. G. (2018). Impact of ground effect on airplane lateral directional stability during take-off and landing. Open Journal of Fluid Dynamics, 8(1), 1–14. https://doi.org/10.4236/ojfd.2018.81001

[42] Mansi, A., & Aydin, D. (2022). The impact of trailing edge flap on the aerodynamic performance of small-scale horizontal axis wind turbine. Energy Conversion and Management, 256, 115396. https://doi.org/10.1016/j.enconman.2022.115396

[43] Patera, A. T. (1984). A spectral element method for fluid dynamics: Laminar flow in a channel expansion. Journal of Computational Physics, 54(3), 468–488. https://doi.org/10.1016/0021-9991(84)90128-1

[44] Rønquist, E. M. (1988). Optimal spectral element methods for the unsteady three-dimensional incompressible Navier-Stokes equations. PhD thesis, Massachusetts Institute of Technology.

[45] Fischer, P., Obabko, A., Kerkemeier, S., Min, M., Lottes, J., Heisey, K., Aithal, S., & Peet, Y. (2015). NEK5000 User's manual (Tech. Rep., p. 67). Available: https://nek5000.github.io/NekDoc/.

[46] NEK5000 Tutorial. (2010). Available online: https://www.mcs.anl.gov/~fischer/nek5000/fischer_nek5000_dec2010.pdf (accessed March 3, 2021).

[47] Karniadakis, G. E., Israeli, M., & Orszag, S. A. (1991). High-order splitting methods for the incompressible Navier–Stokes equations. Journal of Computational Physics, 97(2), 414–443. https://doi.org/10.1016/0021-9991(91)90007-8

[48] Khorrami, M., Choudhari, M., & Jenkins, L. (2004). Characterization of unsteady flow structures near leading-edge slat: Part 2: 2D computations. In 10th AIAA/CEAS Aeroacoustics Conference. https://doi.org/10.2514/6.2004-2802

[49] Geuzaine, C., & Remacle, J. (2009). Gmsh: A three-dimensional finite element mesh generator with built-in pre- and post-processing facilities. International Journal for Numerical Methods in Engineering, 79(11), 1309–1331. https://doi.org/10.1002/nme.2579.

[50] Chi, X., Zhu, B., Shih, T. I.-P., Slater, J., Addy, H., & Choo, Y. (2003). Computing aerodynamic performance of a 2D iced airfoil: Blocking topology and grid generation (Tech. Rep. 20030007845). NASA. https://ntrs.nasa.gov/search.jsp?R=20030007845

[51] Lepage, F., Mavriplis, C., & University of Ottawa. Department of Mechanical Engineering. (2021). Low-Reynolds number direct numerical analysis of an iced NLF-0414 airfoil [Université d'Ottawa / University of Ottawa]. http://hdl.handle.net/10393/42919

[52] Yuan, Y. H., Gmsh2nek, 2020. [Online]. Available: https://github.com/yhaomin2007/Nek5000/tree/master/tools/gmsh2nek

[53] Mittal, K., & Fischer, P. (2019). Mesh smoothing for the spectral element method. Journal of Scientific Computing, 78(2), 1152–1173. https://doi.org/10.1007/s10915-018-0812-9

[54] Schrader, L. U., Brandt, L., & Henningson, D. S. (2009). Receptivity mechanisms in three-dimensional boundary-layer flows. Journal of Fluid Mechanics, *618*, 209–241. https://doi.org/10.1017/S0022112008004934

[55] Tempelmann, D., Schrader, L. U., Hani, A., Brandt, L., & Henningson, D. (2011). Numerical study of boundary-layer receptivity on a swept wing. In 6th AIAA Theoretical Fluid Mechanics Conference.

[56] Massaro, D., Peplinski, A., Stanly, R., Mirzareza, S., Lupi, V., Mukha, T., & Schlatter, P. (2024). A comprehensive framework to enhance numerical simulations in the spectral-element code Nek5000. Computer Physics Communications, 302, 109249. https://doi.org/10.1016/j.cpc.2024.109249

[57] Digital Research Alliance of Canada, "Digital Research Alliance of Canada." [Online]. Available: https://www.alliancecan.ca/en

[58] Offermans, N., Marin, O., Schanen, M., Gong, J., Fischer, P., Schlatter, P., Obabko, A., Peplinski, A., Hutchinson, M., & Merzari, E. (2016). On the strong scaling of the spectral element solver Nek5000 on petascale systems. In Proceedings of the Exascale Applications and Software Conference (pp. 1–10).

[59] Ahrens, J., Geveci, B., & Law, C. (2005). ParaView: An end-user tool for large data visualization. In C. D. Hansen & C. R. Johnson (Eds.), Visualization handbook (pp. 717–731). Elsevier. ISBN 978-0123875822.

[60] Ayachit, U. (2015). The ParaView guide: A parallel visualization application. Kitware. ISBN 9781930934306

[61] The MathWorks Inc. MATLAB version: 9.13.0 (R2022b). Natick, Massachusetts: The MathWorks Inc., 2022. Available: https://www.mathworks.com

[62] Carmichael, B. H. (1981). Low Reynolds number airfoil survey (NASA-CR-165803-VOL-1). NASA Langley Research Center.

Appendices

Appendix A: Sponge Layer

Figures A.1 to A.4 show four successive snapshots of the velocity magnitude field comparing simulation results with and without the sponge layer, illustrating how downstream-shed vortical structures exit the computational domain, and how the sponge layer attenuates flow disturbances. Figures A.1 - A.4 (a) correspond to h/c = 0.8 case with the sponge layer, while Figures A.1- A.4 (b) show the h/c = 1 case without it.

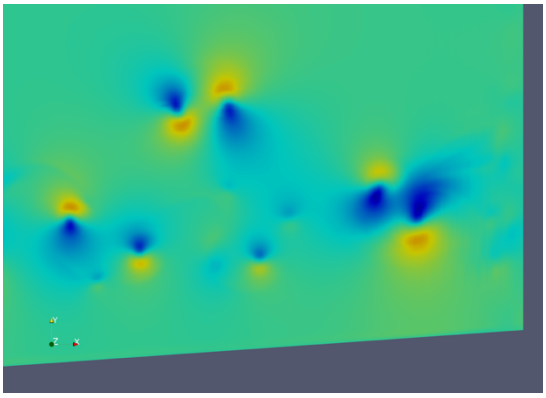

Figure A.1 (a): With Sponge Layer

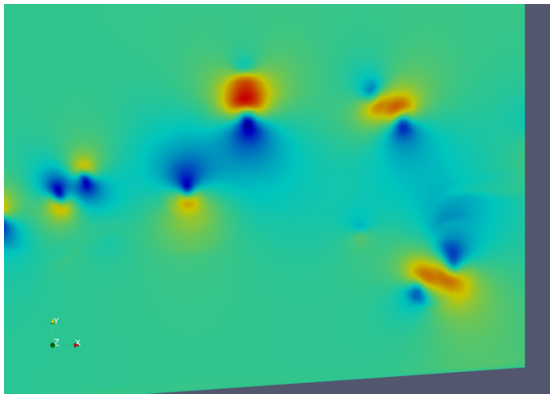

Figure A.1 (b): Without Sponge Layer

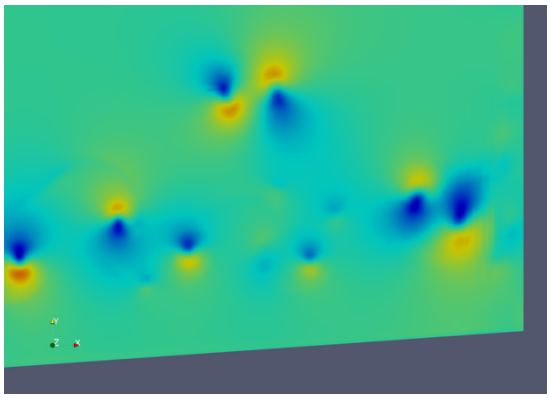

Figure A.2 (a): With Sponge Layer

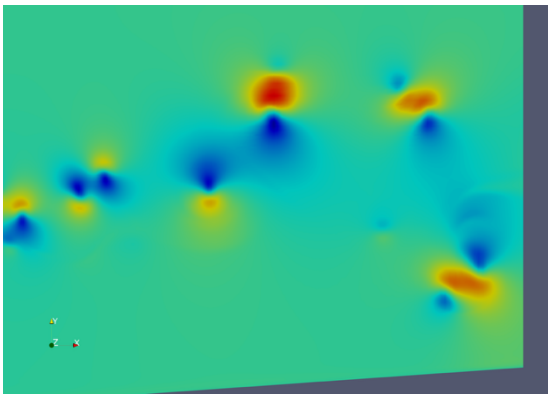

Figure A.2 (b): Without Sponge Layer

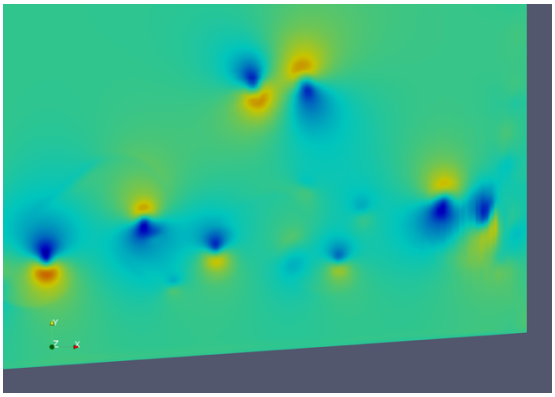

Figure A.3 (a): With Sponge Layer

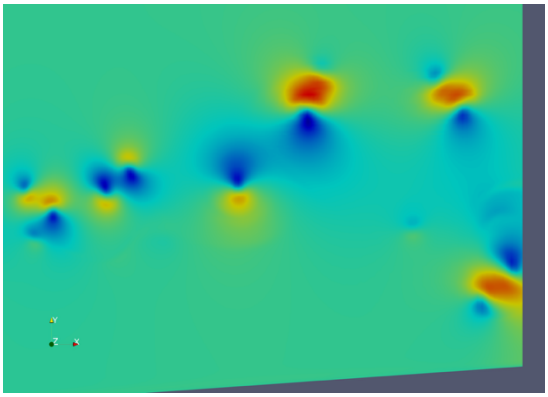

Figure A.3 (b): Without Sponge Layer

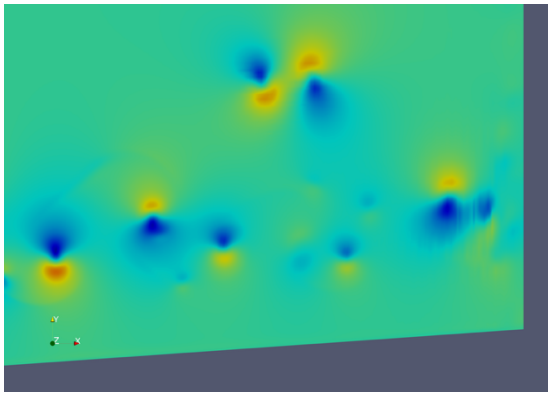

Figure A.4 (a): With Sponge Layer

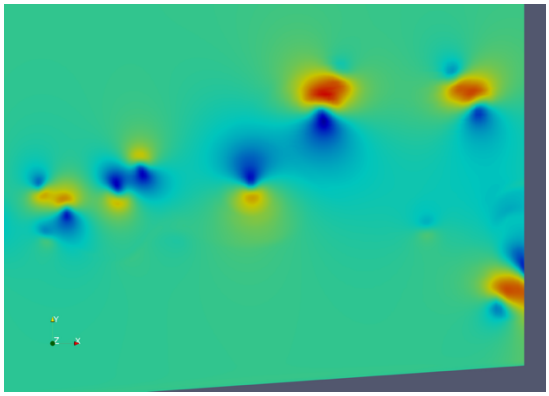

Figure A.4 (b): Without Sponge Layer

It is observed that, without the sponge layer, vortical structures persist up to the outlet boundary, whereas with the sponge layer, velocity fluctuations decay smoothly, minimizing artificial reflections. For these illustrated cases, the vortices are small enough to exit the domain properly without numerical blowup, even without a sponge layer. However, as vortices become larger, this is no longer the case, as illustrated below, and a sponge layer is needed.

A.1 Numerical Blow-Up at the Right Outlet Boundary

In the absence of the sponge layer, the large shed vortices exiting the domain at the right outlet boundary induce a local reverse flow, which disrupts the solution and leads to numerical blow-up of the simulation. This occurs because the unattenuated vortical structures reflect off the boundary, causing unphysical backflow and instability in the numerical solution. The effect is clearly illustrated in Figures A.5-A.9, which show the velocity magnitude fields near the outlet for cases without the sponge layer.

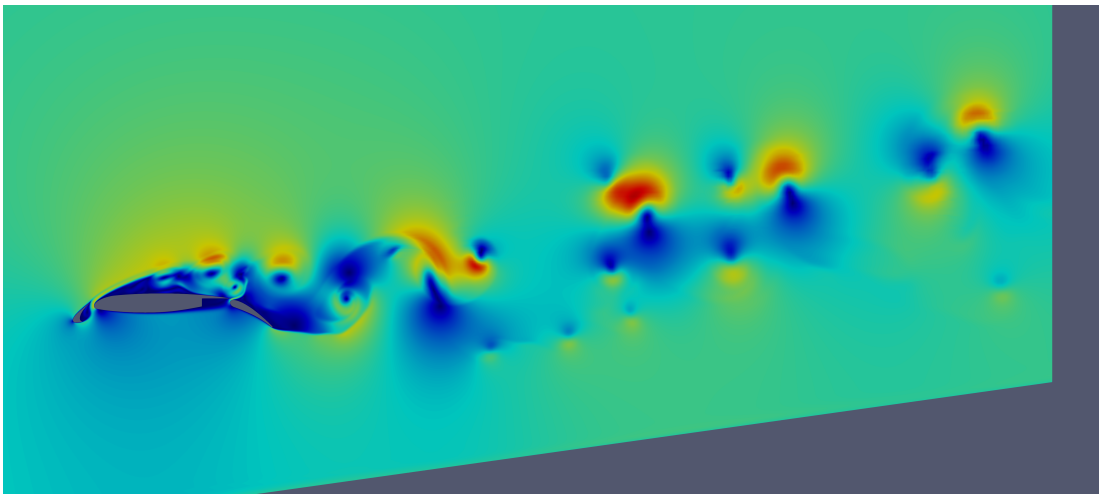

Figure A.5: Instantaneous Velocity Magnitude Field for Ground Clearance Ratio h/c = 1 at Re_c = 1.27 x 10^4, AoA = 8°

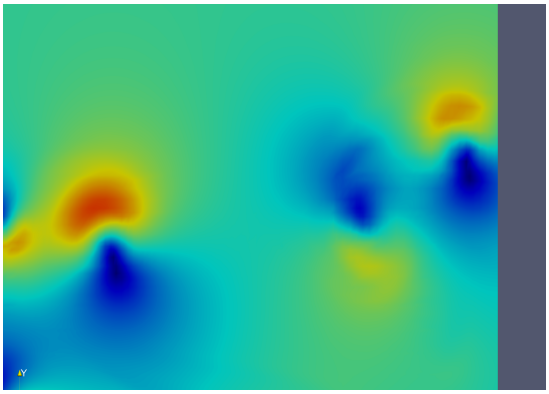

Figure A.6: Large Vortex Exiting

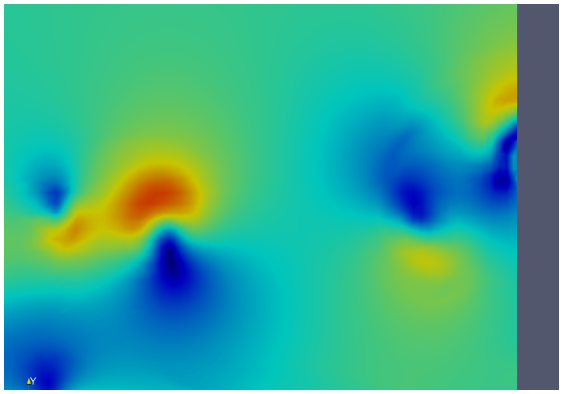

Figure A.7: Onset of Reverse Flow at Exit

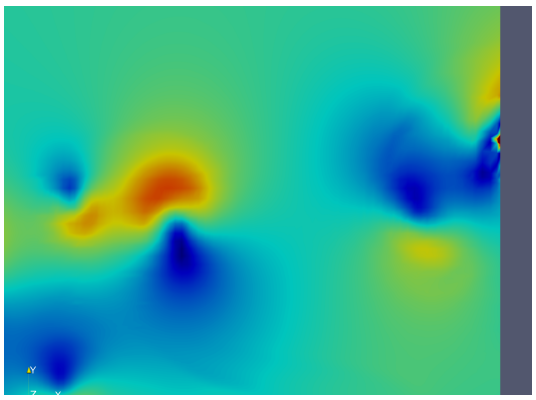

Figure A.8: Reverse Flow Inducing Simulation Blow-Up

Figure A.9: Numerical Blow-Up

Appendix B: Local Reynolds Number (Re_{Lo})

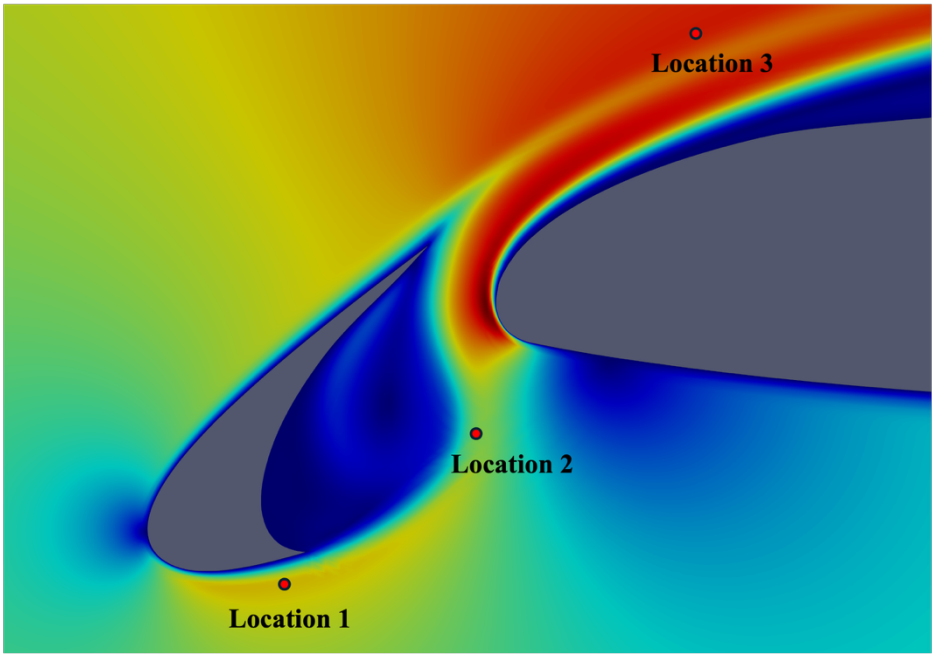

Figure B.1: Marked Locations in the Flow Near the Slat and Main Element Used for Evaluating Local Reynolds Number (Re_{Lo}).

Table B.1: Local Velocity and Reynolds Number Value at Location 1, Flow Below the Slat, for Different Ground Clearance Ratios

h/c	Local Velocity (u_{Lo})	Local Reynolds Number (Re_{Lo})
1	1.166	14808
0.8	1.147	14567
0.6	1.112	14122

Table B.2: Local Velocity and Reynolds Number Value at Location 2, Meandering Flow Between the Slat-Main Gap, for Different Ground Clearance Ratios

h/c	Local Velocity (u_{Lo})	Local Reynolds Number (Re_{Lo})
1	0.738	9372
0.8	0.792	10058
0.6	0.844	10718

Table B.3: Local Velocity and Reynolds Number Value at Location 3, Flow Above the Main Element, for Different Ground Clearance Ratios

h/c	Local Velocity (u_{Lo})	Local Reynolds Number (Re_{Lo})
1	1.515	19240
0.8	1.508	19515
0.6	1.492	18948

From Table B.3, which summarizes the local Reynolds number at Location 2 within the meandering flow region, it is observed that the local velocity increases with decreasing ground clearance ratio due to ground effect. Consequently, the local Reynolds number increases, indicating higher kinetic energy in the flow at this location. This increase in local flow energy enhances the ability of the boundary layer to overcome the adverse pressure gradient (APG) at the leading edge of the main element, thereby delaying flow separation as the ground clearance ratio h/c decreases in the present study. This behaviour is consistent with and provides additional support for the trends discussed in the skin-friction coefficient analysis in the main text.

In addition, the ground effect is expected to alter the local flow direction, introducing an upward flow angle toward the leading edge of the main element. This change in flow angle can promote localized separation near the leading edge and may explain the earlier onset of separation observed in the present ground-effect study compared to the free-stream results reported in [4]. This modified flow behaviour may also contribute to the delayed downstream flow reattachment observed as the ground clearance ratio decreases.

Appendix C: Different Reynolds Numbers

In addition to the primary chordwise Reynolds number of 1.27 x 10^4 at an Angle of Attack (AoA) of 4°, discussed in the main text, additional simulations were carried out at a chordwise Reynolds number (Re_c) of 8.32 x 10^3 and 1.83 x 10^4.

C.1 Instantaneous Velocity Magnitude Field

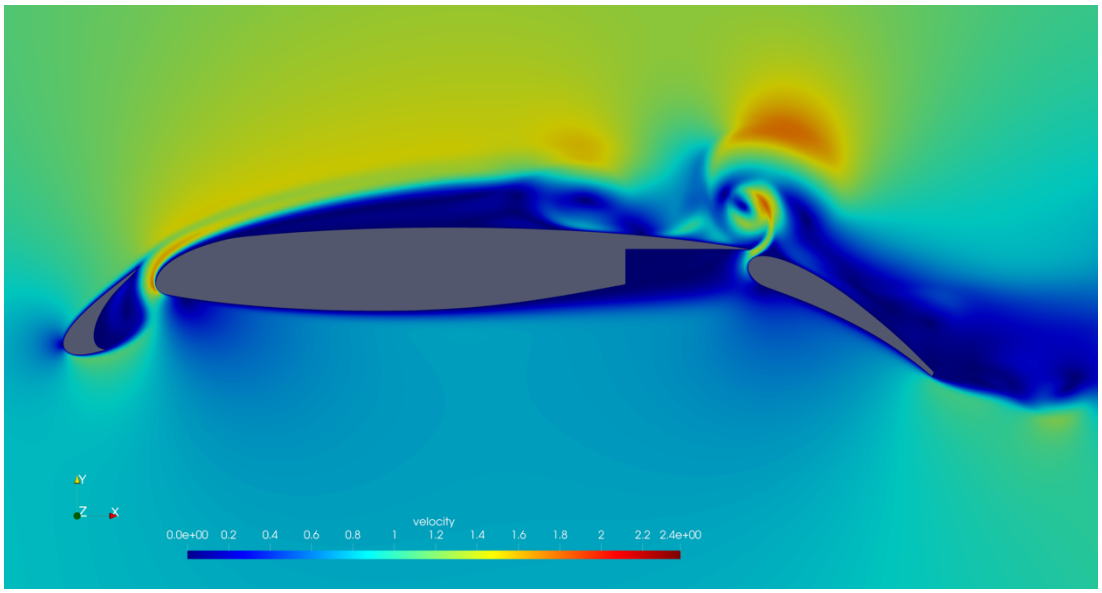

Figure C.1: Instantaneous Velocity Magnitude Field for Ground Clearance Ratio h/c = 0.8 at Re_c = 8.32 x 10^3

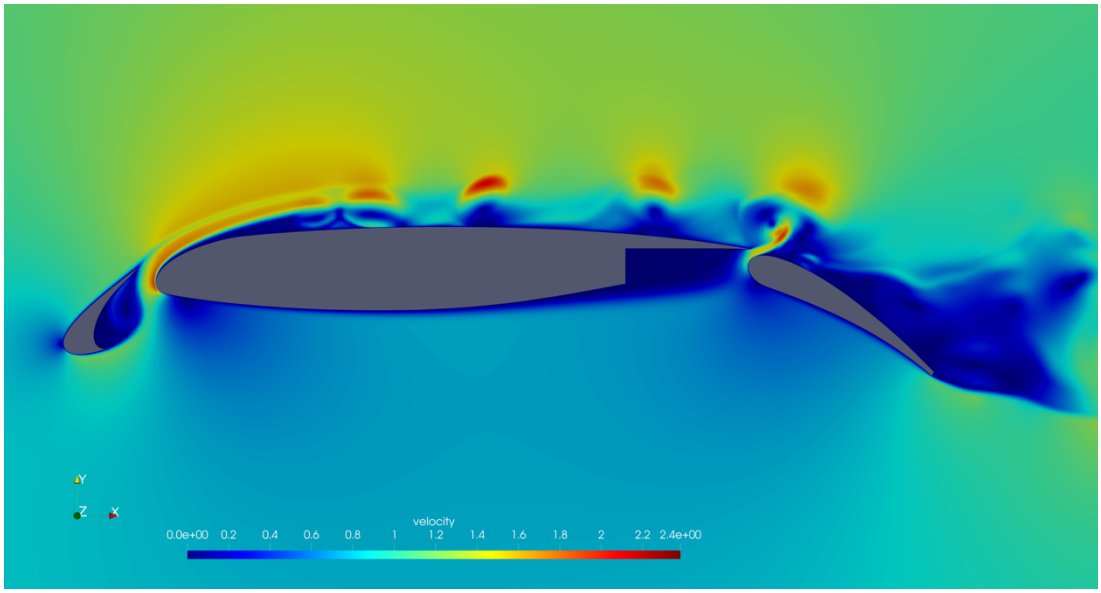

Figure C.2: Instantaneous Velocity Magnitude Field for Ground Clearance Ratio h/c = 0.8 at Re_c = 1.83 x 10^4

C.2 Time-Averaged Velocity Magnitude Field

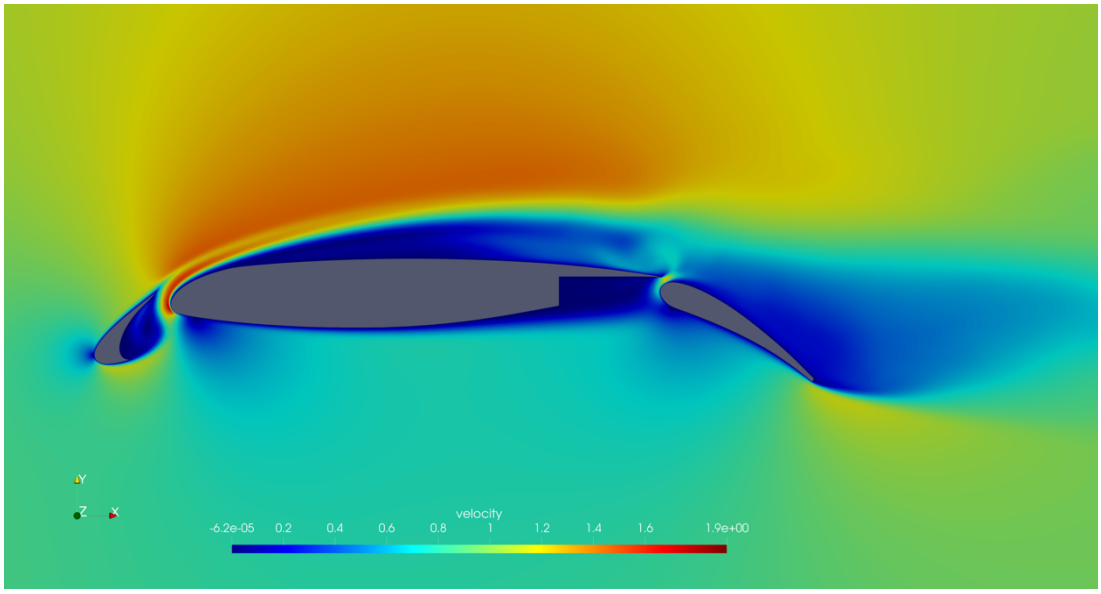

Figure C.3: Time-Averaged Velocity Magnitude Field for Ground Clearance Ratio h/c = 0.8 at Re_c = 8.32 x 10^3

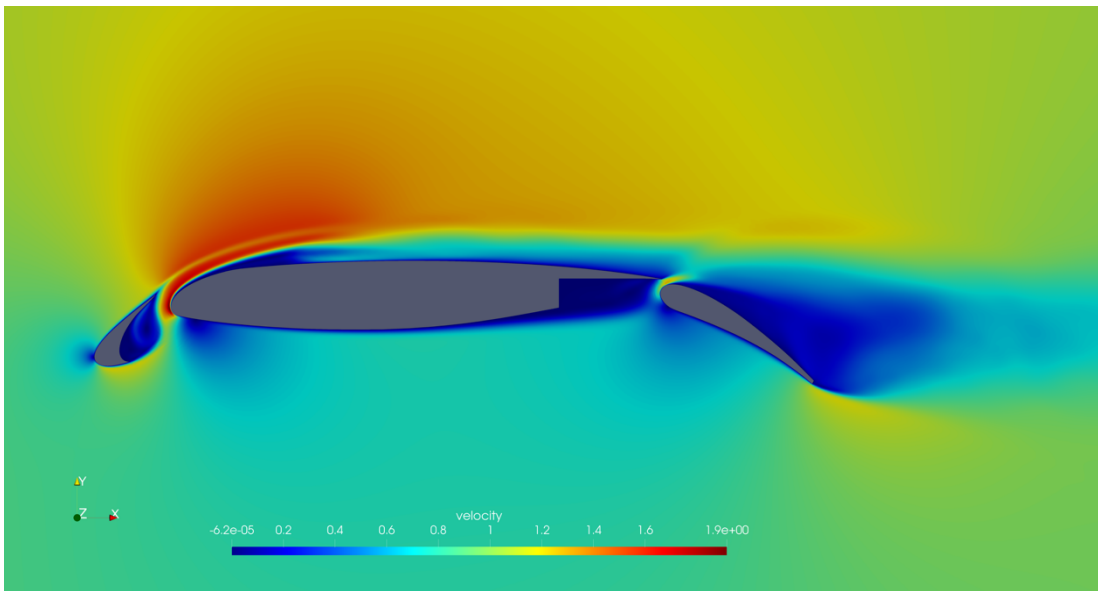

Figure C.4: Time-Averaged Velocity Magnitude Field for Ground Clearance Ratio h/c = 0.8 at Re_c = 1.83 x 10^4

C.3 Time-Averaged u-Velocity Field

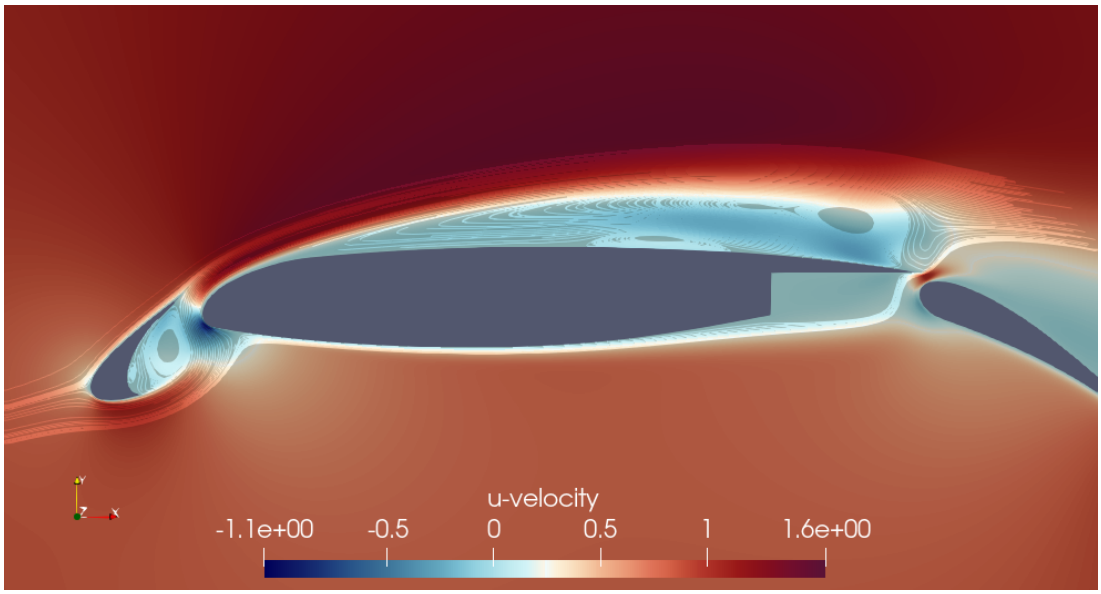

Figure C.5: Time-Averaged u-Velocity Field for Ground Clearance Ratio h/c = 0.8 at Re_c = 8.32 x 10^3

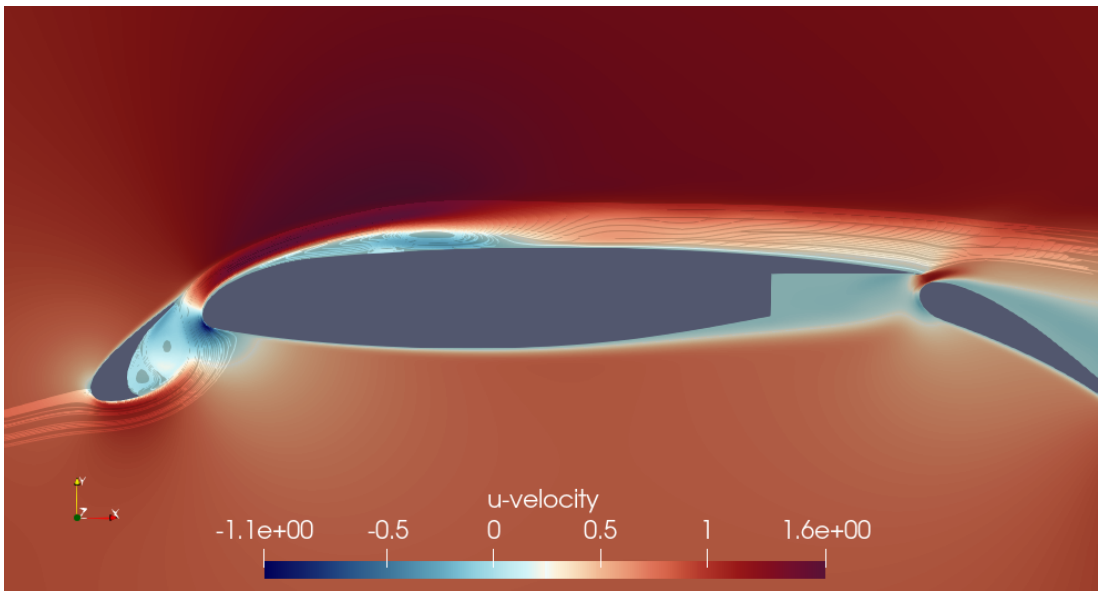

Figure C.6: Time-Averaged u-Velocity Field for Ground Clearance Ratio h/c = 0.8 at Re_c = 1.83 x 10^4

C.4 Lift and Drag Coefficients

The corresponding lift and drag coefficients for a ground clearance ratio of h/c = 0.8 at these Reynolds numbers are summarized in Table C.1.

Table C.1: Lift and Drag Coefficient Comparison for the Different Chordwise Reynolds Numbers (Re_c) at Ground Clearance Ratio h/c = 0.8

Reynolds Number for h/c = 0.8 case	C_L	C_D
8.32 x 10^3	1.7413	0.8630
1.27 x 10^4	1.6706	0.0443
1.83 x 10^4	1.6251	0.0441

It was observed that simulations at higher Reynolds numbers (1.83 x 10^4) sometimes yielded negative drag coefficients (C_D), which is suspected to be due to the limited domain size and requires further investigation.

Consequently, for consistency and reliability, the present analysis and all reported results for different h/c cases were based solely on the Reynolds number of 1.27×10^4 in the main text.

Appendix D: Higher Angles of Attack

In the present study, the main results correspond to an Angle of Attack (AoA) of 4° as discussed in the main text. Additional simulations were performed at higher angles of attack, 6° and 8°, to examine the influence of angle of attack on the flow characteristics and aerodynamic performance. The following sections present the instantaneous velocity magnitude and time-averaged velocity magnitude fields (time-averaged over 1 flow-through, they also looked similar after 3 flow-throughs) for these cases at a ground clearance ratio of h/c = 1, where the AoA = 6° simulation corresponds to a chordwise Reynolds number (Re_c) of 8.32 x 10^3, and the AoA = 8° simulation corresponds to a Re_c of 1.27 x 10^4.

D.1 Angle of Attack (AoA) = 6°

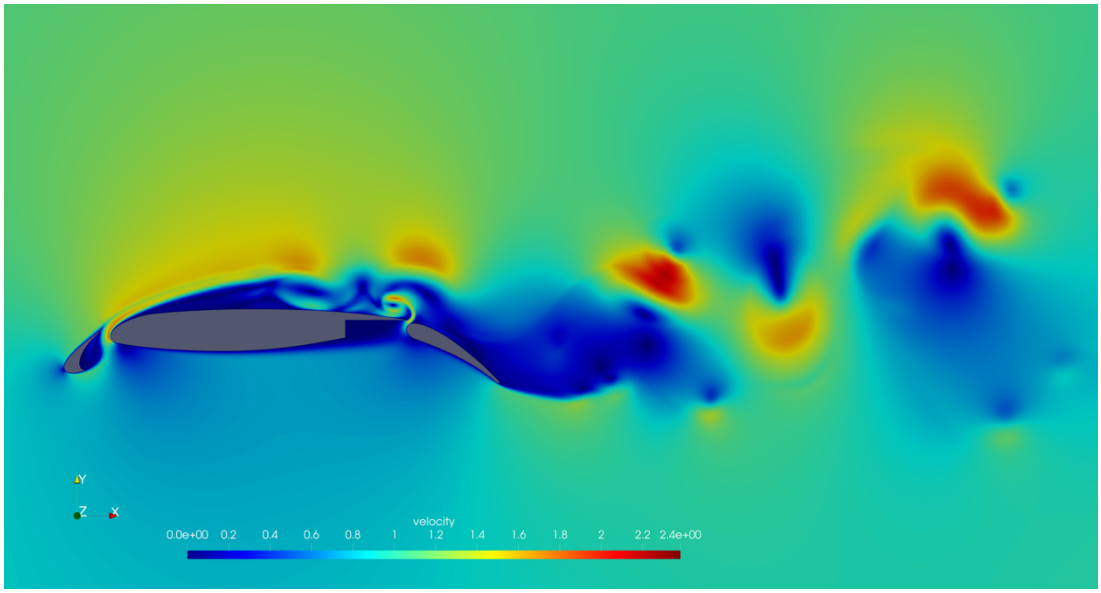

Figure D.1: Instantaneous Velocity Magnitude Field for Ground Clearance Ratio h/c = 1 at Re_c = 8.32 x 10^3, AoA = 6°

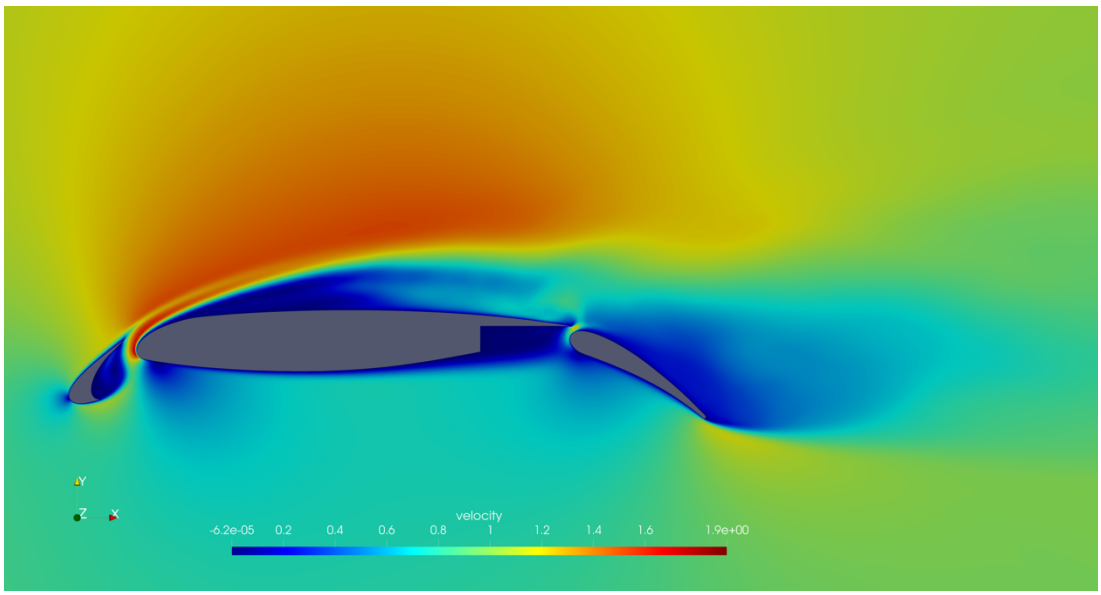

Figure D.2: Time-Averaged Velocity Magnitude Field for Ground Clearance Ratio h/c = 1 at Re_c = 8.32 x 10^3, AoA = 6°

D.2 Angle of Attack (AoA) = 8°

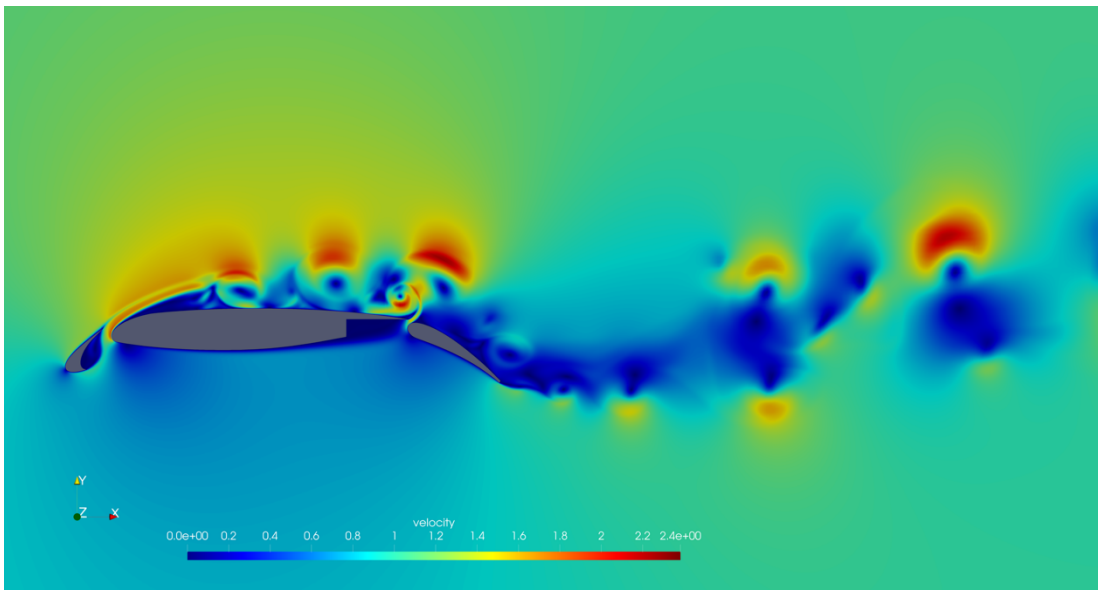

Figure D.3: Instantaneous Velocity Magnitude Field for Ground Clearance Ratio h/c = 1 at Re_c = 1.27 x 10^4, AoA = 8°

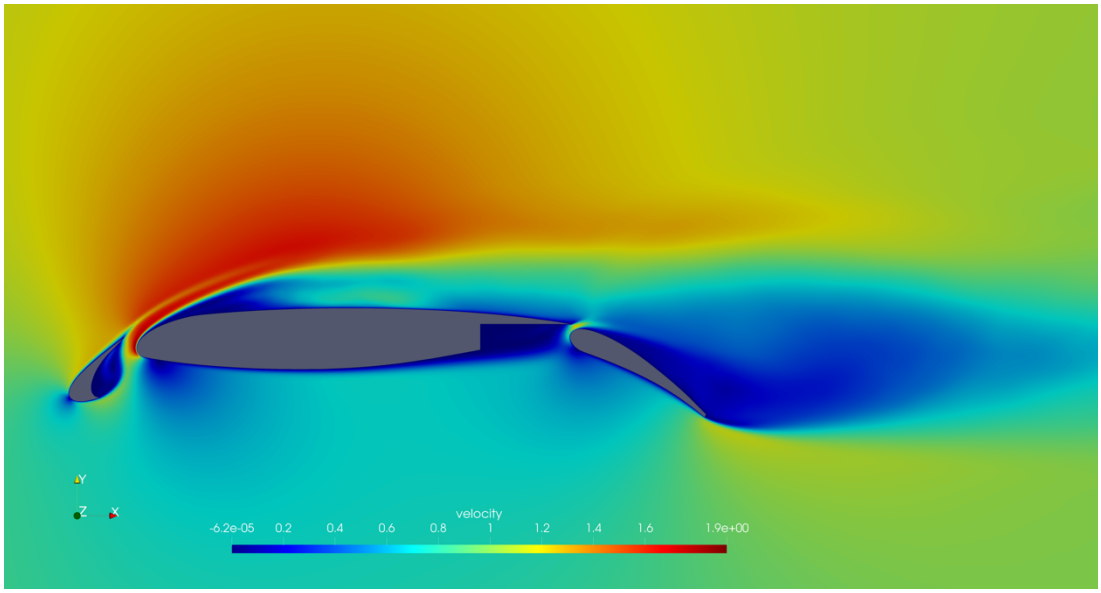

Figure D.4: Time-Averaged Velocity Magnitude Field for Ground Clearance Ratio h/c = 1 at Re_c = 1.27 x 10^4, AoA = 8°

It is observed that for the higher angles of attack (6° and 8°), the vortices shed in the downstream wake are significantly larger compared to the AoA = 4° presented in the main text, as evident from the velocity magnitude fields shown in Sections D.1 and D.2. The increased size and complexity of these wake vortices led to numerical instabilities (leading to blow-up) at the right outlet boundary when using the standard sponge layer parameters that were effective for the 4° simulation. As a result, negative drag coefficient (C_D) values were observed in the simulation output, indicating that the results for these higher angles of attack were not physically reliable. This highlights that higher angles of attack amplify wake unsteadiness and require careful adjustment of numerical damping strategies to maintain stable and accurate simulations.

D.3 Sponge Layer Performance at High AoA

The sponge layer width was insufficient to damp the large vortices generated at high angles of attack, which caused flow reflection back into the domain and led to negative drag coefficient (C_D) values. Figures D.5 - D.7 illustrate the ineffectiveness of the sponge layer in the high-AoA simulation.

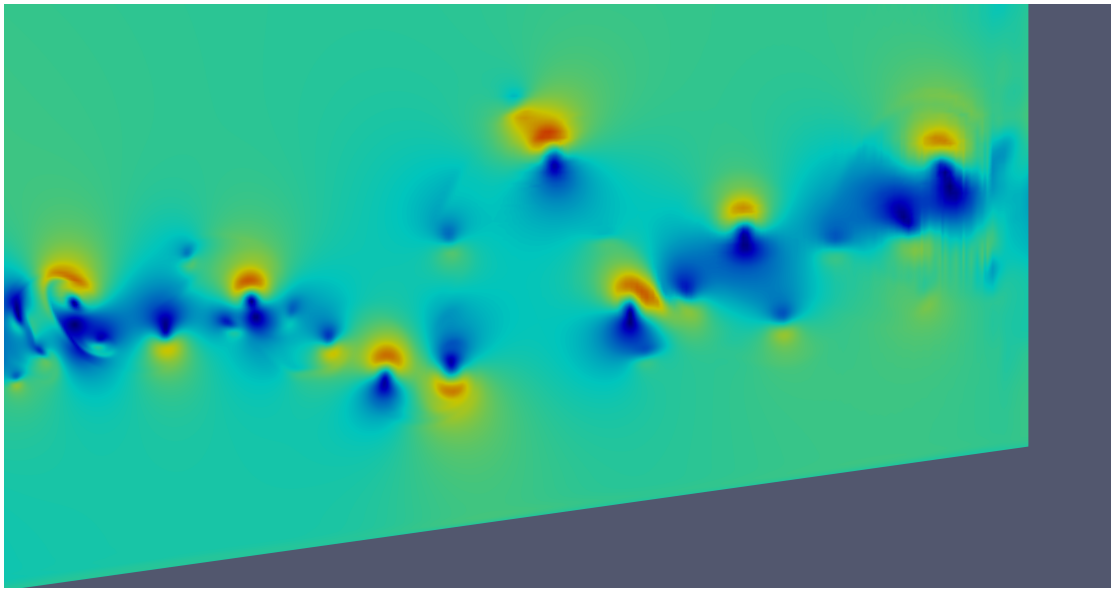

Figure D.5: Ineffective Sponge Layer in Damping Large Exit Vortices for Ground Clearance Ratio h/c = 1 at Re_c = 1.27 x 10^4, AoA = 8°

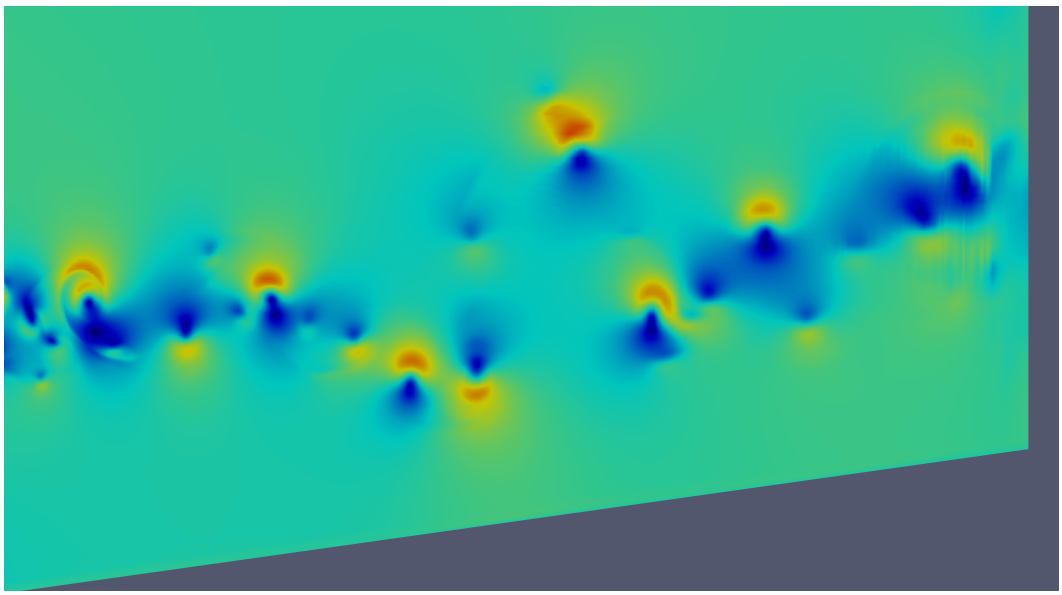

Figure D.6: Skewed Wake Vortices Due to Insufficient Sponge Layer Width for Ground Clearance Ratio h/c = 1 at Re_c = 1.27 x 10^4, AoA = 8°

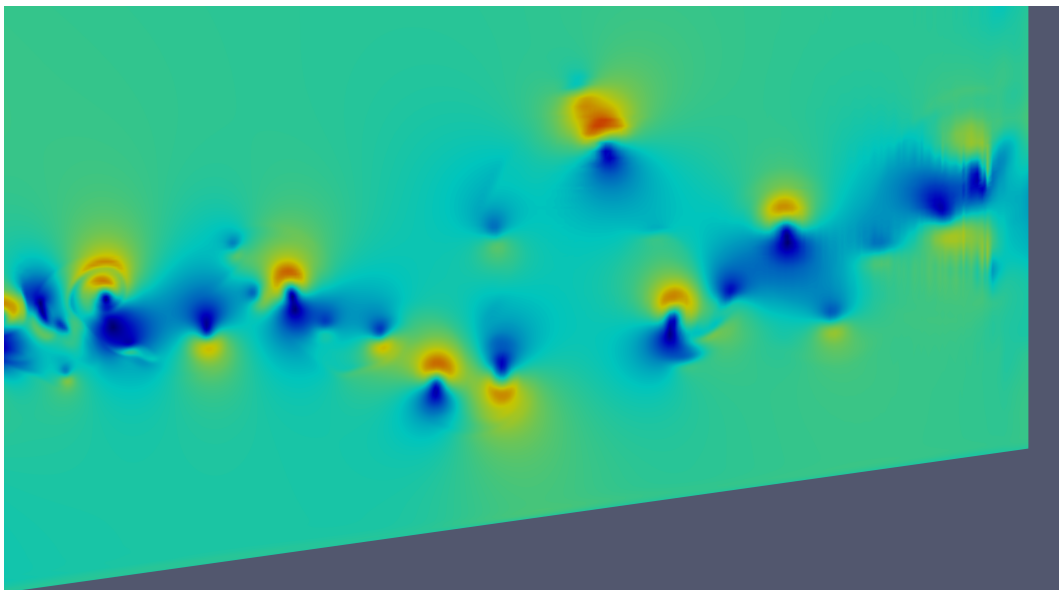

Figure D.7: Insufficient Sponge Layer Width Causing Flow Reflection into the Domain for Ground Clearance Ratio h/c = 1 at Re_c = 1.27 x 10^4, AoA = 8°

To successfully run simulations at higher angles of attack, it is necessary to adjust the width of the sponge layer, which in turn requires increasing the computational domain size.

Attempts were made to expand the domain by an additional 1c downstream and 0.5c above the airfoil, and the sponge layer width was increased by 1% compared to the original setup. However, these modifications still resulted in negative C_D values. Further expansion of the domain in both the downstream and vertical directions was limited by the angled lower boundary and the constraints of the multi-block grid approach used for the mesh. These results indicate that successfully simulating higher angles of attack would require the development of a new domain configuration and mesh generation strategy to accommodate the larger wake structures and ensure stable numerical solutions.